Fundamental Understanding on the Inception of Hydrodynamic Cavitation and its Generated Microbubbles in Fine Particle Flotation

by

Mingda Li

A thesis submitted in partial fulfillment of the requirements for the degree of

Doctor of Philosophy

in

Chemical Engineering

Department of Chemical and Materials Engineering

University of Alberta

Abstract

Hydrodynamic cavitation is a frequently occurring phenomenon with positive and negative implications. Research has been mostly conducted to avoid cavitation in the last century because it is the major cause of corrosion in the marine industry. With the progress of science and technology, hydrodynamic cavitation is now used as an innovative process for enhancing chemical reactions and water disinfection. Most importantly, it has shown great potential in improving the flotation recovery of fine mineral particles. With the pros and cons, understanding the promotion and prevention mechanisms and controlling the inception of hydrodynamic cavitation become essential for industrial applications.

In this thesis, Venturi tubes were used as the hydrodynamic cavitation devices by inducing low static pressure in the throat region. In contrast to the visualization techniques used in the previous research, the cavitation inceptions were measured by detecting the high magnitude energy at the instant of bubble burst. The addition of NaCl was shown to promoted cavitation inceptions. And the results were explained by the increase in air saturation level with lowered water solubility. Based on this idea, an innovative control method of cavitation inception was proposed by modifying the CO_2 solubility by changing the pH of carbonated water. The reversibility of the process was also demonstrated.

In mineral flotation, the hydrodynamic cavitation-generated microbubbles act as an efficient aid for improving fine particle recovery. The process involving particles and tube walls is considered three-phase hydrodynamic cavitation. Experimental studies were performed to better understand the cavitation behavior in the presence of solids with different surface hydrophobicity and surface structure. Results demonstrated that

hydrodynamic cavitation was promoted by particles with low wettabilities but was barely affected by the particle size and roughness. Tests performed using Venturi tubes of different materials demonstrated the similar effect of the wall as particles. Hydrodynamic cavitation was promoted by a more hydrophobic Venturi tube which screened the effect of particle surface properties.

The different behaviors of hydrodynamic cavitation with particles of various wettabilities suggested its potential to achieve not only high recovery but also high grade in particle flotation. This effect of hydrodynamic cavitation on the selective flotation of fine particles was further investigated from a detailed mechanism. The single-bubble flotation experiment indicated that the bubble-particle collection efficiencies of hydrophobic fine silica particles were improved significantly after hydrodynamic cavitation compared to the hydrophilic ones. The results were explained from three perspectives: (1) The strong attachment between microbubble and hydrophobic particles after hydrodynamic cavitation was demonstrated using zeta potential measurements; (2) The formation of large aggregates of hydrophobic fine particles after cavitation was revealed by slurry turbidity and particle size measurements; (3) The attachment efficiency between solid and flotation bubbles was enhanced with cavitation-generated microbubbles on solid surfaces. In the end, the beneficial effect of hydrodynamic cavitation in fine particle flotation was demonstrated in bench-scale flotation tests.

Preface

This thesis contains published and accepted papers, and an article in preparation. The following is the statement of contributions to these co-authored papers presented in this thesis.

1. Chapter 1 and Chapter 2 are original works from Mingda.

2. Chapter 3 presents a published work: Mingda Li, Rogerio Manica, Bailin Xiang, Qingxia Liu. "Effect of NaCl and CO2 on the Inception Control of Hydrodynamic Cavitation by Gas Solubility Change". *Chemical Engineering Science*. Mingda Li performed all the experiments, the data analysis and preprepared the editing manuscript. Rogerio Manica and Bailin Xiang reviewed and edited the manuscript. Qingxia Liu supervised this project and helped with editing.

3. Chapter 4 presents a published work: Mingda Li, Adrien Bussonnière, Bailin Xiang, Rogerio Manica, Qingxia Liu. "Effect of Solid Wettability on Three-Phase Hydrodynamic Cavitation". *Minerals Engineering.* Mingda Li was responsible for the experimental word, the data analysis and manuscript preparation. Adrien Bussonnière provided guidance to the work and helped establish the experimental setup. Rogerio Manica and Bailin Xiang proofread and edited the manuscript. Qingxia Liu supervised this project and helped with editing.

4. Chapter 5 presents an accepted work: Mingda Li, Jing Liu, Jingqiao Li, Bailin Xiang, Rogerio Manica, Qingxia Liu. "Enhancement of Selective Fine Particle Flotation by Microbubbles Generated through Hydrodynamic Cavitation". *Powder Technology*. Mingda Li performed all the experiments, the data analysis and prepared the manuscript.

Jing Liu and Jingqiao Li helped with experimental work. Rogerio Manica and Bailin Xiang reviewed and edited the manuscript. Qingxia Liu supervised this project and helped with editing.

5. Chapter 6 presents a paper in preparation for publication: Mingda Li, Vu Truong, Hao Huang, Qingxia Liu. "Improvement of the Fine Particle Flotation by Optimized Parameters of Dual Bubble Generator". Mingda Li was responsible for experimental work, data analysis, and manuscript preparation. Vu Truong and Hao Huang helped with experimental work. Qingxia Liu supervised this project and helped with editing.

6.   Chapter 7 is an original work from Mingda Li.

Acknowledgements

I would like to express my sincere gratitude to my supervisor, Prof. Qingxia (Chad) Liu for his support and enthusiastic encouragement during my Ph.D. studies. The knowledge and skills I have gained over this time will undoubtedly serve me well as I move forward to the next stage of my life.

I would like to express great appreciation to Dr. Bailin Xiang, Dr. Rogerio Manica, Dr. Adrien Bussonnière and Dr. Jing Liu for their valuable comments and advice that allowed me to look at things from a different perspective. Their support has been invaluable.

I would like to express my thanks to Ms. Laurie Kachmaryk and Mr. James Skwarok for their technical assistance.

The valuable suggestions and comments from Professor John Ralston are much appreciated.

I would like to thank Prof. Hongbo Zeng for allowing me to borrow and use different lab equipment. Without his generous contribution, I would not have been able to finish this thesis.

I would like to express my appreciation to all the colleagues from the research group for all their support and assistance.

Finally, my deepest gratitude goes to my family, father, and mother, who tried their best to support me in my life and encourage me in my research.

Contents

Chapter 5 Enhancement of Selective Fine Particle Flotation by Microbubbles Generated through Hydrodynamic Cavitation 83

List of Figures

List of Tables

Chapter 1 Introduction

1.1.　Background and motivations

Hydrodynamic cavitation is a process of bubble nucleation, growth and collapse that occurs in a flowing liquid. The liquid flow experiences a decrease in pressure due to the hydrodynamic motion of the liquid. The local pressure lower than the saturated vapor pressure leads to the inception of hydrodynamic cavitation, where vaporization occurs around voids and bubbles are formed [1]–[3]. Following the bubble generation, the subsequent recovery of local pressure causes the rapid dissolution of the gaseous phase and inward/outward oscillation of the liquid phase in the local area, which generates a high magnitude of energy.

Hydrodynamic cavitation is now widely used in many industrial applications, utilizing its efficiency and simplicity in bubble generation and energy release. For example, microbubbles generated through hydrodynamic cavitation can effectively improve the fine particle recovery rates [4]–[6]. The bubbles release high magnitude energy at the instant of burst, making them efficient in water disinfection treatment and enhancing oxidation reactions [7]–[11]. However, uncontrolled cavitation is regarded as the cause of disaster in some other applications. In the marine industry, hydrodynamic cavitation induced by the high rotating speed of the impeller and turbine blade is the major cause of physical erosion to hydraulic equipment [12]–[14]. Furthermore, the level of cavitation noise is an order of magnitude higher than the noise of a non-cavitating flow, which increases the risk of detection of navy ships by torpedoes [15]. Therefore, understanding the mechanisms of

prevention and promotion of hydrodynamic cavitation is critical for improving industrial applications according to their different needs.

Among all the applications, hydrodynamic cavitation has emerged as a promising method for improving the performance of froth flotation for fine and ultrafine particles [3], [16]. Froth flotation is a technology discovered in the nineteenth century that utilizes rising bubbles to selectively separate hydrophobic materials from hydrophilic ones in a water vessel. It is now widely used in many industrial applications, including oil sands processing [17]–[20], paper recycling, and wastewater treatment [21], [22]. Most importantly, froth flotation has been heavily utilized in mineral processing for its high efficiency in mineral recovery and separation from gangue [23]–[25].

With the depletion of high-grade and easy to process ore, miners are now facing low-grade and complex ore bodies. In this case, fine grinding circuits must be applied to liberate valuable minerals. The grinding processes usually result in a substantial number of fine particles. However, it has been reported that the small size of mineral particles is unfavorable for the bubble-particle interaction during flotation, which can be explained from the three sub-processes in mineral flotation: collision, attachment, and detachment [26], [27]. The detachment is negligibly small for fine particles because of the low inertia [28], [29]. Their small sizes are mainly attributed to the low collision efficiency and conventional flotation bubbles. Furthermore, the low inertia of fine particles makes it difficult to penetrate the water film around column bubbles, resulting in a lower attachment probability [30]–[35].

Two major approaches have been investigated to improve fine particle flotation, including decreasing the bubble size and increasing apparent particle sizes [36]. In

particular, the methods of enhancing particle sizes by forming flocs or aggregates are of great interest. Typically, a long-chain polymer or coagulant is added to promote the aggregation of fine particles [37], [38]. However, this method had difficulties in the industry due to the lack of selectivity of the reagents used, resulting in the entrapment of gangue minerals [39], [40]. Thus, the demand for an efficient method to selectively improve the collision and attachment of conventional flotation bubbles and fine particles is still substantial.

Studies in the past decade have reported that micro/nanobubbles can effectively improve the flotation recovery and flotation rate of fine particles [6], [16], [41]–[44]. The use of microbubbles can promote particle collection efficiency for two main reasons. First, the generation of microbubbles on the particle surfaces acts as bridges that can significantly enhance the attachment probability between particles and flotation-sized bubbles [45]–[47]. Second, the microbubbles benefit the flotation process by promoting the aggregation of fine particles and increasing the bubble-particle collision probability [4], [48], [49]. Besides that, the advantages of micro/nanobubbles can extend to lower consumption of collector and frother [43], [44]. To sum up, the overall flotation recovery can be effectively improved with massive microbubbles. Hydrodynamic cavitation, as a simple and energy-efficient technology for microbubble generation [8], [50]–[52], shows great potential in the flotation process. To improve the performance of hydrodynamic cavitation in the mineral flotation process, fundamental studies on the particle-involved three-phase cavitation are required. Furthermore, the behavior of hydrodynamic cavitation-generated microbubbles in improving the selectivity and recovery of fine particles requires further study on the perspective of bubble-particle interactions in flotation sub-processes.

1.2. Research objectives

This study aims to investigate the mechanism of hydrodynamic cavitation, develop methods to control the occurrence of both two-phase and three-phase cavitation, and fundamentally understand the roles of generated microbubbles as an aid in fine particle flotation. The main objectives are listed below:

1. To investigate the effect of salt on the inception of hydrodynamic cavitation in an air-water two-phase system and develop a new method for controlling the occurrence of cavitation for different application use.

2. To study the behavior of hydrodynamic cavitation in a solid-air-water three-phase system and the change of cavitation inception with the effects of solid properties, including wettability of tube wall and particles, particle size and surface roughness.

3. To reveal the mechanism of how cavitation-generated microbubbles benefit the fine particle flotation through studying the selective behaviors of microbubbles with hydrophobic and hydrophilic fine particles in flotation sub-processes.

4. To demonstrate the effect of hydrodynamic cavitation in lab-scale column flotation and investigate the relative position of conventional bubble injection to optimize the dual bubble flotation.

In the first part of this thesis (Chapter 3), the effect of salt in promoting cavitation inception is demonstrated using NaCl solutions of different concentrations to induce hydrodynamic cavitation in a Venturi tube. The inceptions are measured using the acoustic detection method. The results are correlated with the dissolved oxygen level of saline water to reveal the effect of gas saturation level change on cavitation inception. Based on this

mechanism, an innovative method of cavitation control is developed by altering the CO2 solubility in carbonated water via pH change, and the reversibility is also tested.

The second part of this thesis (Chapter 4) investigates the inceptions of three-phase hydrodynamic cavitation with the presence of solid particles and tube walls of different surface properties. By using a glass-made Venturi tube with high wettability, the cavitation inceptions with particles of different wettabilities, sizes and surface roughness are investigated and compared. The effect of surface gas pockets is demonstrated by comparing inceptions before and after gas pocket elimination treatment. At last, the influence of tube wettability on three-phase hydrodynamic cavitation is investigated and the screen effect of the tube wall on particle wettability effect is analyzed.

The third part of this thesis (Chapter 5) focuses on the beneficial effect of hydrodynamic cavitation in fine particle flotation. As the collection efficiency with hydrophobic particles after hydrodynamic cavitation treatment has an obvious increase compared to hydrophilic particles, the mechanism of cavitation microbubbles-assisted fine particle flotation is investigated from the perspectives of flotation sub-processes. First, the condition of microbubble frosting on particles is demonstrated using zeta potential distribution observation. Second, the level of particle aggregation with microbubbles is obtained through turbidity and size measurements. Last, the effect of surface microbubbles on the induction time of bubble-solid surface attachment is investigated.

The last particle of this thesis (Chapter 6) further demonstrates the beneficial effect of hydrodynamic cavitation in the recovery and selectivity of fine particle flotation, through tests performed using a lab-scale flotation column. The synergy of cavitation bubbles and conventional bubbles named dual bubble flotation is first optimized by measuring the

bubble sizes and gas holdups with different gas injection locations. Flotation tests with a mixture of fine molybdenite and silica particles are carried out to verify the optimized dual-bubble flotation. The change in the recovery and grade of molybdenite particles is obtained by changing the flow rate and relative position of conventional bubble injection to the cavitation sparger.

1.3. Thesis outline

This thesis consists of seven chapters. Chapters 3 and 4 are published research papers, and Chapter 5 is an accepted paper. Chapter 6 contains a paper in preparation. The content of each chapter is summarized below:

Chapter 1 introduces the background and motivations of the research objectives and the structure of this thesis.

Chapter 2 provides a review of the fundamentals and applications of hydrodynamic cavitation. The potential use of hydrodynamic cavitation in the flotation process is also reviewed.

Chapter 3 discusses the effect of salt on the inception of hydrodynamic cavitation, which can be used to promote or prevent cavitation for different applications. The mechanism of cavitation inception by altering gas saturation level is explained, and an efficient method of cavitation control by modifying the pH of carbonated water is proposed. This chapter has been published:

Mingda Li, Rogerio Manica, Bailin Xiang, and Qingxia Liu. "Effect of NaCl and CO_2 on the Inception Control of Hydrodynamic Cavitation by Gas Solubility Change" *Chemical Engineering Science*. vol. 246, p. 116997, 2021.

Chapter 4 introduces the effect of solid surface properties on the inception of three-phase hydrodynamic cavitation. The mechanism of hydrodynamic cavitation initiated by gas pockets on hydrophobic solid surfaces is explained. The wettability effect of the Venturi tube wall that screens the effect of particle wettability is discussed. This chapter has been published:

Mingda Li, Adrien Bussonnière, Bailin Xiang, Rogerio Manica and Qingxia Liu. "Effect of Solid Wettability on Three-Phase Hydrodynamic Cavitation" *Minerals Engineering*. Vol. 180, p. 107455, 2022.

Chapter 5 illustrates the influence of hydrodynamic cavitation-generated microbubbles on the overall performance and sub-steps of particle flotation, including bubble frosting, particle aggregation and flotation-size bubble attachment. The beneficial effects of microbubbles on all the processes are compared between hydrophobic and hydrophilic silica particles. A mechanism is summarized to explain the overall enhanced flotation recovery and selectivity with cavitation bubbles. A version of this chapter has been accepted:

Mingda Li, Jing Liu, Jingqiao Li, Bailin Xiang, Rogerio Manica, Qingxia Liu. "Enhancement of Selective Fine Particle Flotation by Microbubbles Generated through Hydrodynamic Cavitation". *Powder Technology*.

Chapter 6 presents the experimental demonstration of hydrodynamic cavitation in improving the recovery and grade of fine particle flotation, using a lab-scale flotation column with a mixture of naturally hydrophobic molybdenite and hydrophilic silica particles. The flotation results were correlated with bubble size and gas holdup analysis to

examine the location effect of conventional bubble injection with respect to cavitation microbubble sparger. The dual bubble flotation is optimized.

Mingda Li, Vu Truong, Hao Huang, Rogerio Manica, Qingxia Liu. "Improvement of the Fine Particle Flotation by Optimized Parameters of Dual Bubble Generator".

Chapter 7 summarizes the conclusions from this research and presents future research plans.

Chapter 2 Literature Review

2.1. Hydrodynamic cavitation principles

As briefly introduced, hydrodynamic cavitation is a process of bubble nucleation, growth and collapse. The generation of hydrodynamic cavitation can be achieved by the passage of liquid through a constriction such as throttling valve, orifice plate and Venturi tube. The local liquid pressure experiences reduction due to the hydrodynamic motion of the liquid, which is affected by the geometrical layout of the flow passage. If the pressure reaches a critical low point, nucleation of bubbles happens, and cavitation is incepted. The required critical low pressure for cavitation inception is usually below the saturated vapor pressure, so tensile stress is generated on the water body to rupture the liquid phase. The pressure difference between vapor pressure and cavitation inception pressure is called the tensile strength of the liquid [53], [54]. The tensile strength value represents the level of difficulty for cavitation inception and depends on the purity and surface tension of the liquid. In an ultra-pure mono-phase water system, an extremely low inception pressure has been reported at around -240 MPa due to the high surface tension of water [51]. In reality, the tensile strengths of water are often far lower, with critical inception pressures slightly below the saturated vapor pressure. This phenomenon has been explained by the presence of pre-existing gas nuclei, which create the "weak points" for the liquid to rupture [51], [55]–[60].

2.1.1. The presence of gas nuclei

However, doubts about the presence of gas nuclei have been raised due to the discrepancy between theoretical low lifetime, according to the Laplace pressure equation for a spherical bubble: $\Delta P = \frac{2\sigma}{R}$, where ΔP is the difference between pressures inside and outside of a bubble in water, σ is the air-water surface tension, and R is the bubble radius. Based on the theory, bubbles of sub-micro sizes have incredibly high inner pressure, which would result in bubble dissolution under milli-seconds. In contrast, the discovered nanobubbles in many works published in the literature are reported to have a lifetime of weeks or even months [61]–[63]. A number of theories have been proposed to explain the long lifetime of the gas nuclei. For instance, gas supersaturation around tiny bubbles causes equilibrium of gas exchanges to offset the Laplace pressure, or the negatively charged ions at the air-water interface lower the surface tension, but both with their flaws [64]–[66]. A model of contamination coating was proposed in which bubbles can be initially partially covered with organic contaminants or surfactants [67], [68]. The bubbles shrink until their surfaces are fully covered with the contaminants, which prevent the gas from further diffusing. Similar to the contamination coverage mechanism, the dynamic equilibrium model was developed. In this case, the bubbles are stabilized by partial attachment to a hydrophobic material [64], [69]. The hydrophobic material immersed in water forms a surface depletion layer enriched with dissolved gas. A bubble attaching to the hydrophobic material would experience both gas influx from the depletion layer and gas outflux from the uncovered part; thus, equilibrium can be reached. Therefore, the presence of hydrophobic solid contaminants theoretically enhances the inception of hydrodynamic cavitation by providing gas pockets for bubble nucleation.

2.1.2. Gas nuclei in solid crevices

It is reported that solid enhanced heterogeneous nucleation of bubbles is more energy-efficient compared to homogeneous nucleation. However, the bubble nucleation performed with smooth surfaces still shows a more difficult occurrence than the observation in practical operations [53][70]. The results provided a promising theory that the pre-existing gas cavities in surface crevices promote the formation of bubbles [71]. For a solid surface with an advancing contact angle θ_a and a conical crevice with half angle α, water can easily enter the crevice and fill it completely if $\theta_a < \alpha$ as illustrated in **Fig 2.1a**. On the contrary, water cannot fully wet the crevice if $\theta_a > \alpha$ as shown in **Fig. 2.1b**, resulting in an entrapped air pocket in the crevice bottom. For a static contact angle $\theta > 90^o + \alpha$, the gas cavity concaves into the crevice and the nuclei are stabilized as shown in **Fig. 2.1c**. In fact, the nuclei can be naturally formed according to Kelvin's equation for a sphere-like volume [72]:

$$R_g T \ln \left(\frac{P_k}{P_o} \right) = \frac{2\sigma V_m}{R} \tag{2.1}$$

where P_k and P_o are the vapor pressure of curved and flat surfaces, V_m is the molar volume of the liquid, and R is the radius of the sphere-like volume. The Kelvin equation relates the vapor pressure with the curvature of the liquid. For such a concave shape of gas pocket in a crevice as shown in **Fig. 2.1c**, R is positive and $P_k > P_o$. The water molecules at the air-water interface would undergo evaporation until R increases to a critical value and equilibrium is reached, thereby stabilizing the gas pocket. If θ is lower than $90^o + \alpha$, the cavity exhibits a convex shape as shown in **Fig. 2.1d**. In this case, the gas pocket can only be stabilized or even enlarged if the pressure inside the nuclei (vapor pressure and

undissolved gas partial pressure) is equal or higher than the liquid pressure to balance the Laplace pressure imposed by the curvature. The details of bubble nucleation under cavitation from such small cavities will be explained next.
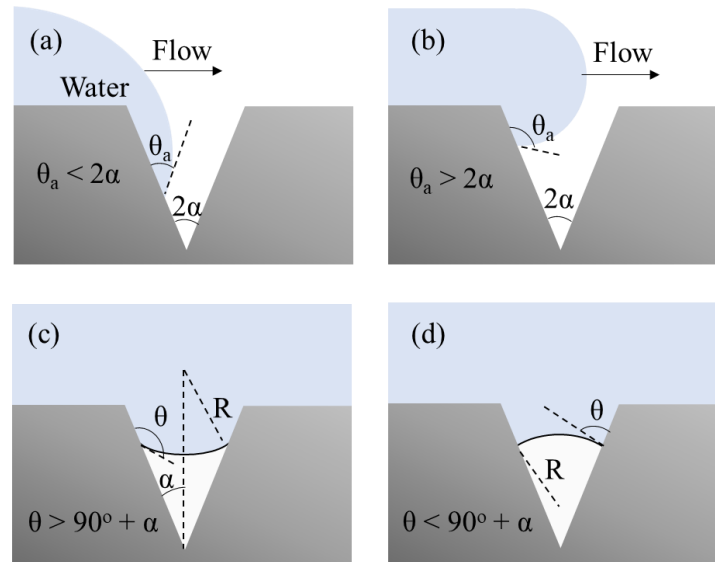
Figure 2.1. Schematic illustration of a liquid wetting with a conical crevice on (a) hydrophilic surface and (b) hydrophobic surface, and entrapped gas cavities with (c) concave shape and (d) convex shape.

2.1.3. Bubble nucleation from gas cavities

The presence of gas nuclei in water provides sites for the vaporization of surrounding water molecules. However, due to the large Laplace pressure of tiny bubbles $\Delta P = \frac{2\sigma}{R}$, the pressure inside bubbles is much higher than the liquid pressure. Therefore, a local pressure lower than the saturated vaporization pressure is required to initiate vaporization, and the tensile strength of water is negatively correlated with the size of pre-existing bubbles. For acoustic cavitation or hydrodynamic cavitation induced using devices with short convergent and constriction regions such as orifice plates, the gas diffusion from the

surrounding water body to the nuclei during the pressure drop is neglected. In this case, the relation between the critical low pressure for bubble nucleation and bubble radius can be approximated using Blake's radius obtained from the Laplace equation in quasi-static equilibrium condition [73]:

$$P_{bo} = P_v + P_{go} = P_{lo} + \frac{2\sigma}{R_o} \tag{2.2}$$

where P_{bo} is the initial pressure inside a spherical bubble of radius R_o, P_v and P_{go} are the vapor pressure and initial partial pressure of undissolved gas within the bubble. Assuming an isothermal flow, as the static pressure is lowered, P_v remains unchanged, and the new gas pressure P_g can be obtained from the ideal gas law:

$$P_g = P_{go} \frac{R_o^3}{R^3} \tag{2.3}$$

and the new pressure balance at equilibrium condition:

$$P_v + P_g = P_l + \frac{2\sigma}{R} \tag{2.4}$$

By combining the three equations 2.2-2.4, we can get the relationship between liquid pressure at the bubble surface and bubble radius:

$$P_l = P_v - \frac{2\sigma}{R} + \frac{A}{R^3} \tag{2.5}$$

where the constant term $A = \left(P_{lo} - P_v + \frac{2\sigma}{R_o}\right) R_o^3$. Based on this equation, P_l is plotted against R in **Fig. 2.2**, where the minimum critical pressure $P_{l,cr}$ is shown at the critical radius R_{cr}, referred to as the Blake radius. By differentiating Eq. 2.4, Blake's radius can be obtained as:

$$R_{cr} = \frac{4\sigma}{3(P_v - P_{l,cr})} \tag{2.6}$$

As **Fig. 2.2** shows, nuclei with a radius smaller than the Blake radius are stable, as the size has little change when the liquid pressure recovers. On the other hand, nuclei with sizes larger than the Blake radius can grow explosively as the pressure increases and cavitation is incepted. Three curves with different R_o are plotted in the figure. The bubble with a larger initial radius R_o leads to a higher $P_{l,cr}$, and a lower tensile strength of the liquid. Therefore, cavitation can be promoted with the presence of large nuclei. Through calculation, a bubble in tens of micrometers has $P_{l,cr}$ slightly lower than the saturated vapor pressure. The result explains the phenomenon that cavitation usually happens when pressure is lowered to the saturated vapor pressure, as the presence of microbubbles is quite common.
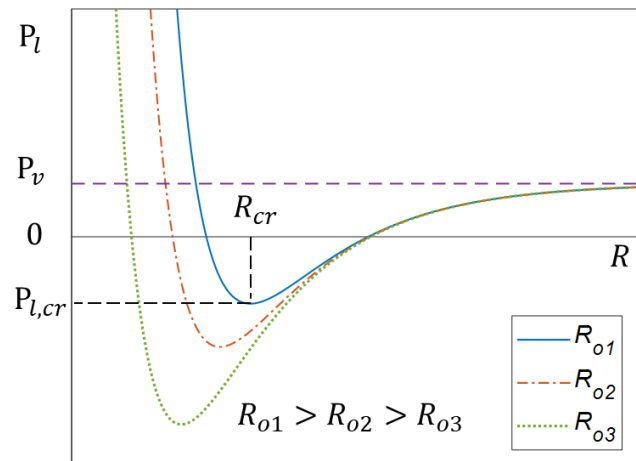
Figure 2.2. Blakes's radius and critical liquid pressure. Three curves were plotted with different initial bubble radiuses.

Compared to acoustic cavitation or orifice induced hydrodynamic cavitation, where the pressure reductions can happen in microseconds, a longer period of pressure drop is also

commonly seen, e.g., hydrodynamic cavitation induced by a Venturi tube with a long convergent or constricted section. In this case, the diffusion of uncondensable gas plays a significant role in cavitation inception. According to Henry's law, the gas solubility in water decreases with liquid pressure [74]. The supersaturated dissolved gases possessing sufficient time to diffuse will enter the existing gas nuclei and enlarge their sizes. As a result, the inception of cavitation becomes much easier. Furthermore, the diffusion of gases could induce cavitation at a pressure higher than the vapor pressure, named gaseous cavitation [75], [76].

Following the nucleation and growth during cavitation, bubbles experience the stage of collapse/implosion when the liquid pressure recovers. This is particularly significant for vaporous cavitation, as the vapor bubbles almost immediately condense when the local pressure increases above the saturated vapor pressure. The collapse of bubbles consequently induces the motion of surrounding water, producing powerful microjets and shock waves that can potentially generate high pressure at tens of megapascals inside the bubble and high temperature at thousands of Kelvin at the bubble surface [77], [78]. Such shockwaves and microjets can erode the surface and cause mechanical wear. At the same time, cavitation's high efficiency has been utilized in energy release in various applications, which will be elaborated in the next section.

2.2. Disadvantages of hydrodynamic cavitation

As introduced previously, the collapse/implosion of cavitation bubbles are accompanied by intense pressure waves, vigorous shearing forces and localized heating that is particularly destructive to local material. As illustrated in **Fig 2.3**, the collapse of vapor bubbles experiences asymmetrical inward motion of liquid due to the presence of a

solid surface on the opposite side. This results in the formation of a micro-jet, which penetrates through the bubble and potentially hits the surface [79]–[81]. Without the proper control of the location and intensity, cavitation was regarded as an unfavored process in the early years of study, especially in the marine industry [13], [82]–[84]. From the investigation of the eroded equipment, the pump, compressor, and turbine that operate underwater are found to induce uncontrollable cavitation, which causes a reduction of thrust and damage to components such as the impeller and turbine. The generation of hydrodynamic cavitation in these cases is due to the high rotating speed of the impeller, causing a rapid decrease in the local pressure according to Bernoulli's principle. Associated with the micro-jets or shockwaves, the generated cavities eventually lead to the removal of material elements from the surface. In the operating conditions of the hydraulic machinery, cavities are repetitively formed, and the collapse of cavities generates shock waves that are subject the material fatigue stresses [83]. Furthermore, the level of cavitation noise is an order of magnitude higher than the noise of a non-cavitating flow, which increases the risk of detecting navy ships by torpedoes [15]. Such undesired behaviors of hydrodynamic cavitation have caused immeasurable loss to the industries and driven scientists to deeply investigate the mechanism behind this phenomenon to better control its occurrence.
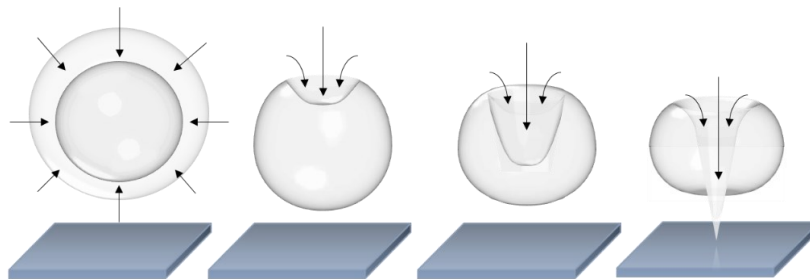
Figure 2.3. Schematic illustration of a cavitation bubble collapsing close to a solid surface in water.

2.3. Hydrodynamic cavitation in industrial applications

With further investigations on its behavior, hydrodynamic cavitation due to its energy efficiency and simplicity has gradually twisted its reputation as a beneficial process [85]. For example, cavitation has been intentionally generated for testing the intensity of erosion on various materials [82], [84]. Hydrodynamic cavitation is now being utilized in various industry-scale applications as an efficient bubble generation and violent energy release process. By understanding the use of cavitation in those areas, hydrodynamic cavitation can be adjusted accordingly to optimize the benefit for each process.

2.3.1. Water treatment

Hydrodynamic cavitation has been utilized in the water treatment industry. At the instant of burst, the cavitation bubbles release high magnitude energy, physically and chemically destroying microorganisms and disinfecting wastewater [9]–[11]. Compared to the traditional water disinfection with chemical additives, cavitation does not result in the formation of any toxic byproducts. It is also economical and efficient for a large-scale water treatment scheme. To have hydrodynamic cavitation as the pretreatment, the consumption of chemical additives for killing microbes can be substantially lowered.

Like acoustic cavitation triggered by the oscillating ultrasonic field, hydrodynamic cavitation is driven by the sudden drop and recovery in pressure due to the change in flow velocity. The rapid change in the surrounding environment results in the generation of oscillating bubbles. By adjusting the ultrasonic field or pressure recovering time (different frequencies), cavitation can manifest in different properties and mechanisms for implementing it into different scenarios. High frequencies generate a higher number of

collapses and promote the diffusion of OH$^-$ radicals, which can be used as a biocide in water treatment, but the generated bubbles are less energetic. On the other hand, low frequencies tend to generate more violent collapse and strong shock waves, but at the expense of less collapse per unit time and less diffusion of OH$^-$ radicals.

Compared to acoustic cavitation, which disinfects water mostly by chemical processes with the generation of OH$^-$ radicals, mechanical disruption of bacteria plays a major role in hydrodynamic cavitation. The bacteria tend to form clusters, and the external microorganisms can act as protection against biocides. The shear force produced by cavitation can break the agglomerates and isolate the individual bacteria, increasing biocides' efficiency [86]. Therefore, the disinfection rates are maximized by configurations that promote large bubbles and higher cavitation activity.

The efficiency of using orifice plates in rhodamine B degradation is also compared with the results of using acoustic cavitation. The hydrodynamic cavitation using orifice plates was proved to produce a higher disinfection rate, with higher energy efficiency than acoustic cavitation. Moreover, the scale-up of the hydrodynamic cavitation reactors is easier as having a constriction in the flow system is readily available [87], [88]. Overall, hydrodynamic cavitation is a relatively simple and energy-efficient technology that is promising to implement on an industrial water treatment scale.

2.3.2. Chemical reaction enhancing

In conventional chemical processes such as chemical synthesis with oxidation reaction, the utilization of acoustic cavitation has been extensively studied [8], [89]. However, due to poor transmission of acoustic energy in the large volume of water and low energy

efficiency, the implementation of acoustic cavitation in industrial-scale processes has been challenging [52]. Researchers recently highlighted the use of hydrodynamic cavitation in chemical processes. Despite the disadvantages of less intense collapse compared to acoustic cavitation, hydrodynamic cavitation has the advantages of easy scaling up and high energy efficiency.

For a better description of cavitation's effect in chemical processes, the collapse of cavities can be classified into two types: symmetric and asymmetric [90]. The symmetric collapse happens when the cavity remains spherical until burst, forming reactive free radicals favoring thermal pyrolysis of organic molecules. For asymmetric collapse, the collapsing cavity is not spherical because of the presence of a wall or particle at the point of collapse. It produces high-velocity liquid jets and intense local turbulence, which is favorable for physical transmission. In the symmetrical collapse condition, when the water is under cavitating conditions, the highly reactive hydroxyl radicals (OH^-) are formed from the dissociation of water molecules. The symmetrical collapse is beneficial, especially for the oxidation reactions that are primarily induced by the formation of reactive free radicals. The oxidation processes caused by cavitation happen in two ways: First, the molecules trapped inside the cavity undergo thermal decomposition during the collapse. Second, the formed radicals attach the targeted molecules at the cavity liquid interface and in the bulk liquid, thereby oxidizing the molecules [8], [91]. Each cavity behaves as a micro-reactor during cavitation, which releases a large amount of energy and creates a local condition of high pressure and temperature [7].

Pandit and Joshi first tested the use of hydrodynamic cavitation in the hydrolysis of oils in 1993. The experiment showed an improved hydrolysis yield with the use of HC. The

traditional hydrolysis methods require high temperature and pressure, as well as a high interfacial area between the catalyst and the oil. With hydrodynamic cavitation, spots with adequate temperature and pressure can be created at many locations inside the reactor. Also, the size of the catalyst emulsion is mechanically reduced, which facilitates the interaction between the oil and catalyst [8]. Similarly, hydrodynamic cavitation was shown to be helpful in crude oil upgrades for its ability to produce high temperature, pressure, and catalyst-reagent contact area to break large molecular petroleum fractions into smaller ones [8], [92].

2.3.3. Food processing

The traditional heat-treat process for food sterilization involves several problems, including low efficiency at killing heat-resistant microorganisms, high energy consumption and risks of destroying heat-labile nutrients and flavor components. Inspired by the contribution to the water treatment industry, cavitation is regarded as an alternative method for commercial sterilization of food by processors [87], [93], [94]. Using hydrodynamic cavitation without any further processes, the induced destructive forces can effectively inactive bacteria, yeast, and heat-resistant bacterial spores. The microbial lethality induced by hydrodynamic cavitation is reported to be greater than that accounted by thermal effects. To combine hydrodynamic cavitation with the traditional heat treatment process, the lethality of common spoilage microorganisms can be achieved at reduced temperature due to the synergistic effect of cavitation and temperature. This way, the heat-labile components can be retained, and foods such as fruit juice, salad dressing, and milk can be safely processed.

Besides food sterilization, cavitation can be beneficial for many other applications in the food processing industry. The ultrasonic induced acoustic cavitation has been developed to accelerate processes such as freezing, thawing, and crystallization of lactose and improve processes such as cutting, extraction, emulsification, and ageing of wines [94], [95]. Considering the energy efficiency in food processing, which involves large volumes, hydrodynamic cavitation is suggested to be the alternative to acoustic cavitation. It has shown promising potential at solving many problems faced by the food industry, such as the replenishment of moist lost during storage and primary processing [96]. In the hydration process, hydrodynamic cavitation can assist chemically pure protein in binding theoretically up to 40% water by weight. The formed hydration shells of protein increase their affinity for water during precipitation. In addition, the formation of dense and strong hydration shells raises the thermal resistance of the dissolved valuable nutrients and vitamins, preventing them from thermal denaturation at the subsequent heat treatment.

2.4. Froth flotation for mineral processing

The froth flotation process was invented in the early 20th century and has been widely used in many applications for material separation, such as wastewater treatment and paper recycling [97]. It utilizes bubbles to selectively adhere to the surface of objects in water based on the affinity for water (hydrophilic or hydrophobic) so that the target material in the form of bubble aggregate has a reduced density and is carried to the water top driven by buoyancy force. Different from the definitions in some works of literature, that flotation is a process that separates material solely based on density, in this thesis, the word "flotation" is the shortened form of "froth flotation", which involves the interactions with bubbles and is also dependent on the wettability of the material [98].

In the mining industry, the freshly mined mineral ores contain different types of valuable materials and unwanted gangue minerals that require separation for further processing. The froth flotation process has been used as an efficient and versatile technique to collect target minerals based on their distinct affinity to air bubbles. As shown in **Fig. 2.4**, air bubbles are injected and dispersed from a rotating agitator at the tank bottom in a typical mineral flotation process. The bubbles interact with hydrophobic particles at the flotation pulp to form mineral-bubble aggregates and rise to the top froth layer for collection. On the other hand, the hydrophilic particles that fail to attach to bubbles settle to the tank bottom and are discharged out of the pulp.
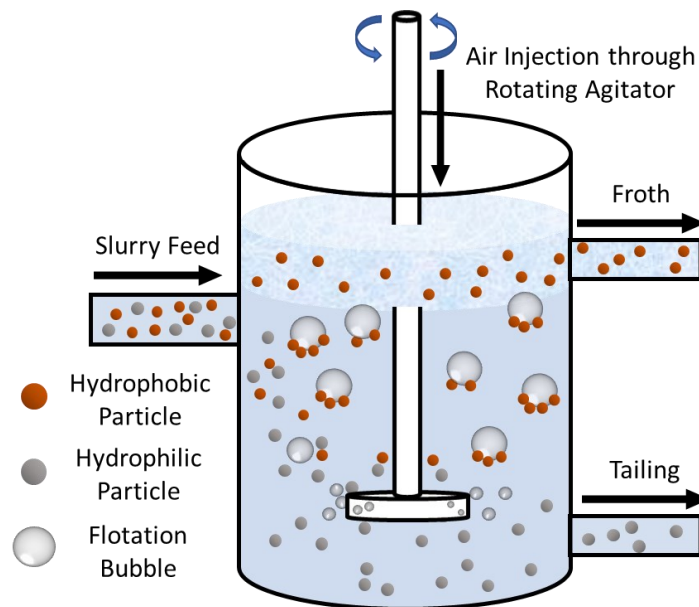
Figure 2.4. Schematic process of mineral flotation.

However, in many flotation processes, the target minerals are not naturally hydrophobic, or the surface hydrophobicity of target minerals is not high enough to achieve selective attachment to air bubbles. In such scenarios, collectors are required to render the mineral surface hydrophobic. Collectors are surface-active surfactants that consist of a hydrophobic

head that interacts with solid surfaces by a specific mechanism, leaving the long hydrocarbon chain oriented toward air bubbles, thus creating a hydrophobic film on the particle surface. For example, xanthates and hydroxamates can chemically bind the specific metal sites (e.g., Pb, Cu) of sulphide or non-sulphide minerals, leaving the hydrocarbon tails to enhance the hydrophobicity of mineral surfaces. Sodium oleate is used for iron oxide, where the oleate group makes contact with air bubbles and the carboxyl group of the oleate interacts with silica surfaces. In contrast, the depressants, usually as high molecular weight polymers, can adsorb on the undesired minerals to render them hydrophilic [97], [99], [100]. Together with pH regulators, the chemical reagents tune the solid surface characteristics in aqueous media, which ultimately dictate the value recovery and selectivity of froth flotation separation.

2.5.   Three sub-processes in mineral flotation

The mechanism of bubble-particle interaction in mineral flotation has been discussed overwhelmingly in the past decades. It is generally accepted that three sub-processes: collision, attachment, and detachment, as shown in **Fig. 2.5**, compose the particle collection process [31], [101], [102]. The probability of a particle being collected by an air bubble, P_{col} can be defined as:

$$P_{col} = P_c P_a (1 - P_d) \qquad (2.7)$$

where P_c, P_a, and P_d are the probabilities of bubble-particle collision, attachment, and detachment, respectively.
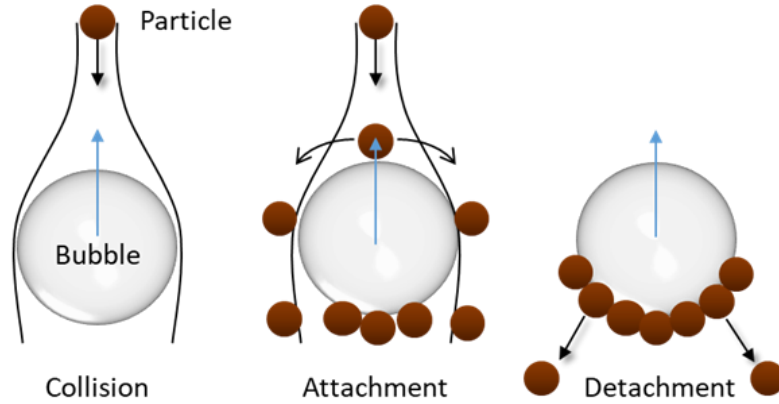
Figure 2.5. Diagram of three sub-processes in mineral flotation.

2.5.1. Bubble-particle collision

The bubble-particle collision probability, P_c can be defined in the generalized form [102], [103]:

$$P_c = A \left(\frac{d_p}{d_b}\right)^n \tag{2.8}$$

Table 2.1. A and n for different flow conditions in the collision probability calculation

Flow Conditions	A	n
Stokes flow	3/2	2
Intermediate 1	$\frac{3}{2}\left[1 + \dfrac{(3/16)Re}{1 + 0.249Re^{0.56}}\right]$	2
Intermediate 2	$\left[\dfrac{3}{2} + \dfrac{4Re^{0.72}}{15}\right]$	2
Potential flow	3	1

The equation for the Stokes flow condition is derived using the stream function by Gaudin (1957), and is only applicable for bubbles smaller than approximately 100 μm. In contrast, the equation for potential flow derived by Sutherland (1949) is only valid for much larger bubbles than the bubbles in flotation practices. Recognizing the limits of equations for Stokes and potential flow, Weber and Paddock (1983) solved the Navier-Stokes equations using a curve fitting technique to derive the first P_c equations for intermediate flow, which is in the more applicable range of bubble and particles sizes. Yoon and Luttrell (1989) derived the second expression for P_c based on the stream function for the intermediate Reynolds number range. As the equations suggest, a higher Reynolds number of bubbles, Re would result in higher collision probability, which is in line with the intuition that objects are more likely to collide with each other in a turbulent flow. Besides hydrodynamic parameters, bubbles and particles' size also plays an important role in determining the collision probability in the flotation process. This is particularly significant for fine particles flotation, as the collision probability proportional to the square power of small particles sizes is generally low.

2.5.2. Bubble-particle attachment

The bubble-particle attachment probability, P_a is determined by comparing the sliding time of a particle on a bubble surface with the period required for particle-bubble attachment, termed induction time. If the sliding time is longer than the induction time, the particle has enough time to thin and rupture the liquid film between the surfaces for successful attachment. For flow with an intermediate Reynolds number, Yoon and Luttrell

(1989) used the stream function to calculate the sliding times of particles on bubble surfaces. Based on the above information, P_a is derived as [102]:

$$P_a = \sin^2\left[2\tan^{-1}\exp\left(\frac{-(45 + 8Re^{0.72}u_b t_i)}{15d_b(d_b/d_p + 1)}\right)\right] \qquad (2.9)$$

where u_b is the bubble rising velocity and t_i is the induction time. Dobby and Finch in 1987 and 1990 developed another theory to describe the relationship between P_a and t_i. The generalized form under Stokes flow or potential flow can be expressed as [104]:

$$P_a = \text{sech}^2\left(\frac{2u_p B t_i}{d_p + d_b}\right) \qquad (2.10)$$

Table 2.2. B for different flow conditions in the attachment probability calculation

Flow Conditions	B
Stokes flow	$\dfrac{u_b}{u_p} + 1 - \dfrac{3}{4}\left(1 + \dfrac{d_p}{d_b}\right)^{-1} - \dfrac{1}{4}\left(1 + \dfrac{d_p}{d_b}\right)^{-3}$
Potential flow	$\dfrac{u_b}{u_p} + 1 + \dfrac{1}{2}\left(1 + \dfrac{d_p}{d_b}\right)^{-3}$

where u_p is the particle settling velocity, and B is a dimensionless parameter under Stokes flow or potential flow according to equations listed in **Table 2.2**. The induction time is strongly a function of surface forces such as the Van der Waals, electrostatic and hydrophobic forces. It can be experimentally determined using devices such as atomic force microscopy (AFM) and induction timer [105]. Knowing the value of t_i, the attachment probability can be estimated under different flow conditions.

2.5.3. Bubble-particle detachment

Particles that collide and attach onto bubbles do not necessarily guarantee a successful flotation, as they might undergo the last sub-process, detachment. The probability of a particle detaching from a bubble depends on the combined effect of detachment and attachment forces. The forces are usually classified into four categories: (1) the capillary force which is the major attachment force; (2) the excess force, which is usually considered an attachment force in practical flotation, where the bubble diameter is less than 5.5 mm and the excess pressure in the bubble is larger than the hydrostatic force; (3) the weight of particle and (4) the hydrodynamic drag force are always considered as detachment forces. The relationship between the probability of detachment, P_d, the total detachment force, F_d and the total attachment forces, F_a can be generalized as [106]:

$$P_d = \frac{1}{1 + F_a/F_d} \tag{2.11}$$

and F_a/F_d after neglecting the drag force can be estimated as:

$$\frac{F_a}{F_d} \approx \frac{3(1 - \cos\theta_d)\sigma}{g\left(\rho_p - \rho_w\left(\frac{1}{2} + \frac{3}{4}\cos\left(\frac{\theta_d}{2}\right)\right)\right)} \frac{1 + \frac{d_p}{d_b}}{d_p^2} \tag{2.12}$$

where θ_d is the critical contact angle right before detachment, σ is the liquid surface tension, ρ_p and ρ_w are the densities of particles and water, respectively. For particles with large diameters, $F_a/F_d < 0$, and the detachment is more likely to happen. On the other hand, the detachment in fine particle flotation is often neglected.

2.6. Fine Particle Flotation

As discussed previously, the probability of a particle to be collected by a bubble is positively correlated with the probabilities of collision and attachment but negatively affected by detachment. For fine particles, the detachment is negligibly small. In fact, the low recovery is believed to be mainly attributed to the low efficiency of collision and attachment probability between conventional flotation bubbles and fine particles [29], [31], [101], [107], [108]. The model of bubble-particle collision probability suggests that under the same hydrodynamic condition, the collision probability is proportional to the square of the ratio of particle size to bubble size. This analysis explains the low collision probability of fine particles and provides a solution that increasing the particle size or reducing the bubble size would result in a better chance of collision.

Researchers have conducted experiments to increase the bubble/particle collision probability in fine particle flotation. In particular, the methods of increasing the effective particle sizes by forming flocs or aggregates are of great interest. It was reported that techniques such as oil-assisted flotation, carrier flotation, shear flocculation and selective polymer flocculation could effectively promote the aggregation of fine particles (Forbes, 2011; Warren, 1975; Trahar and Warren, 1976; Subrahmanyam and Frossberg, 1990; Gregory and Barany, 2011; Forbes et al., 2011) [37], [38]. The oil and carrier flotation method are used to aggregate fine particles with larger ones such as oil droplets or other hydrophobic materials. To overcome the repulsive energy barrier for particle/oil or particle/carrier attachment, strict physical and chemical conditions must be met, including high shear forces and proper pH range. Also, separating oil from particle aggregates and water in the post-treatment is challenging, especially when oil emulsions are formed. The

shear flocculation technique helps to achieve aggregation by applying a shear field with the aid of a collector. Still, it has the problem of high-energy consumption to produce adequate hydrodynamic conditions. The technique of polymer flocculation is an efficient method to form aggregates by attaching particles onto the long chains, but the easy entrainment of gangue materials causes low selectivity. Considering the disadvantages of the above techniques, the demand for an efficient method to selectively improve the collision and attachment of conventional flotation bubbles and fine particles is still substantial.

2.6.1. Particle-particle interaction laden surface small bubbles

In recent years, the use of micro/nanobubbles, as a relatively green and energy-efficient technology, has been found to improve both the recovery and selectivity of fine particles [30], [45], [46], [109]. The research on the impact of small bubbles on fine particle flotation has suggested that the microbubbles can act as bridges that enhance particle-particle interaction to form aggregates. As the size of a bubble is reduced, the bubble rising velocity decreases, which results in a longer sliding time that enhances bubble-particle attachment [110]. Furthermore, the induction time of a small bubble to attach to a surface is much quicker due to the considerable Laplace pressure [111]. With the small bubbles attached to the surface, the approach of two particles causes the bubbles to coalesce and generate an attractive capillary force, as shown in **Fig. 2.6** [45], [112], [113].
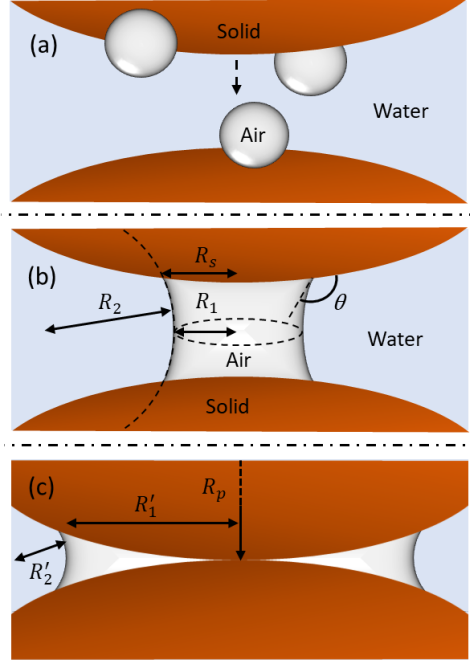
Figure 2.6. Schematic illustration of the approach of two spherical particles with surface small bubbles.

The calculation of capillary force, F_{Cap} can be illustrated in **Fig. 2.6b**, where it consists of the Laplace pressure force, F_P and the surface tension force, F_{ST}, with F_P defined as:

$$F_P \approx \pi R_s^2 * 2\sigma \left(\frac{1}{R_1} + \frac{1}{R_2} \right)$$

(2.13)

where R_s is the radius of the air-solid contact area assuming a flat surface, and $\left(\frac{1}{R_1} + \frac{1}{R_2} \right)$ is the curvature of the air-water interface. In the case illustrated in **Fig. 2.6b**, the contact angle θ is high enough to generate a curvature concave into the capillary, R_2 is negative, and the curvature is positive, thus generating an attractive Laplace pressure force. On the other hand, F_{ST} is always attractive defined as:

$$F_{ST} \approx 2\pi R_s * \sigma \sin(\pi - \theta)$$

(2.14)

For a given volume of capillary, as the two particles approach closer, R_s increases. As a result, the overall capillary force increases. When the two particles are in contact as shown in **Fig. 2.6c**, the capillary force reaches the maximum. Assuming $R_1' \gg R_2'$, the capillary force can be estimated as [114]:

$$F_{Cap} \approx 2\pi\sigma R_p \tag{2.15}$$

where the force only depends on the radius of the particles, R_p. Such a capillary force is strong enough to hold two spherical silica particles of about 2 mm against the gravitational force. In reality, the capillary force is often much smaller due to the lower air-solid contact area from surface roughness. Despite that, the surface small bubbles can hydrodynamically enhance and stabilize the accumulation of particles, forming bubble-particle aggregates. Experimental investigations into the small-bubble-assisted agglomeration phenomenon were confirmed using image analysis [6], [46], [49]. However, further demonstration of the effect of small bubbles to selectively aggregate particles of different properties is still required.

2.6.2. Particle-flotation bubble interaction laden surface small bubbles

Although small bubbles can easily collide and attach onto mineral particles, their low volume cannot provide sufficient buoyancy force to life the aggregates up. At this point, the large flotation bubbles of millimeter sizes come into play to complete the flotation process. The role of small bubbles in the attachment process between particles and large flotation bubbles is explained by small bubbles helping the fine particles adhere to large flotation bubbles by reducing the induction time, thereby enhancing attachment probability [45]–[47].

The induction time is determined by the thinning of the thin liquid film trapped between the particle and the air bubble [29], [115], [116]. For a millimeter size bubble colliding with a flat particle surface (i.e., the bubble is much smaller than the particle), typically, it takes a few seconds [117],[118] for the thin liquid film to reach its critical rupture thickness. The time is reported to be slightly shorter (hundreds of milliseconds) if the particle is spherical [119]. When a surface microbubble (~10 μm) much larger than the typical film thickness (~1 μm) is present on the particle surface, the situation switches from large bubble-particle attachment to large bubble-surface microbubble coalescence. If the coalescence time is significantly shorter than the reported bubble-particle attachment time (a few seconds), mineral flotation can be enhanced.

There has been extensive research done on bubble coalescence. For instance, the dynamic evolution of the thin liquid film trapped between two millimeter-size bubbles was directly observed by the Scheludko cell [120], while the interaction force between micrometer-size bubbles was measured by atomic force microscopy [121]. These works revealed the complex effect of hydrodynamics, surface deformation, and surface forces on the deformation of bubbles, which entraps the liquid to form a stable film and results in a relatively long induction time, as shown in **Fig. 2.7** [122]. However, the experimental collision speeds were limited below 0.1 mm/s, whereas the industrial bubble collision speeds are much faster (mm/s or even cm/s) [123]. A new experimental method called Dynamic Force Apparatus (DFA), which allowed higher collision speed to mimic industrial operation conditions, was applied to achieve the simultaneous measurements of the interference fringe and interaction force at bubble speeds on the order of 1 mm/s. At higher speeds, the coalescence time between a micrometer bubble and a large bubble was shown

to be size-dependent [124]. The experimental results were compared with the prediction of the Stokes-Reynolds-Young-Laplace (SRYL) model [122], [125], showing agreement that the coalescence time increases with surface microbubble size.
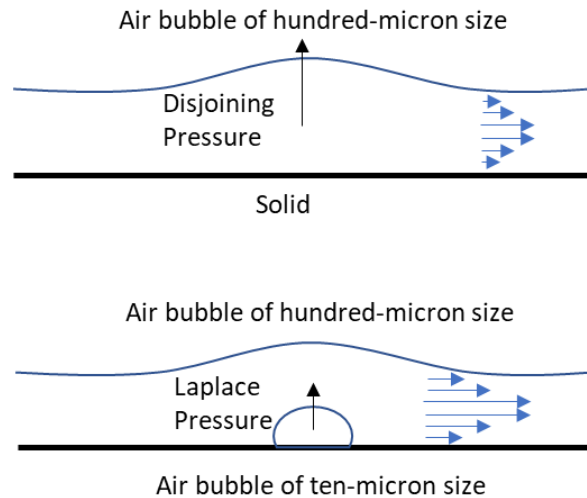
Figure 2.7. Schematic process of liquid drainage when an air bubble of hundreds of micron size approaches a solid surface without (top) and with (bottom) a surface micron bubble.

The increased Laplace pressure of $2\sigma/R$ can explain the fast film drainage with smaller bubbles. The increase of the Laplace pressure increases the excess pressure inside the liquid film. According to the Reynolds lubrication theory, the increase of excess pressure would accelerate the film drainage, causing the induction time to be much shorter than the reported bubble-particle attachment time. Therefore, the flotation recovery can be improved with the presence of surface microbubbles.

Chapter 3 Effect of NaCl and CO₂ on the Inception Control of Hydrodynamic Cavitation by Gas Solubility Change

Abstract

Hydrodynamic cavitation is a common natural phenomenon that has positive and negative implications in several fields. On one hand, it is a major cause of corrosion and noise radiation in the marine industry. On the other hand, it is used as an innovative process for enhancing mineral flotation and water disinfection. Therefore, understanding the promotion and prevention mechanisms of hydrodynamic cavitation inception is essential for industrial applications. In this study, a Venturi tube was used as the hydrodynamic cavitation device, and the cavitation inceptions were measured using the sound-detection method. NaCl was shown to promote cavitation inception of water. However, no obvious change was observed for air-saturated NaCl solutions. These results are explained by the increase in air saturation level when salt is added into water. Based on this idea, the cavitation inception can be controlled by modifying the CO_2 solubility through changing the pH of carbonated water, a process that was shown to be reversible. These findings are applicable to industrial operations that try to avoid cavitation or those where the generation of bubbles is required.

3.1. Introduction

Hydrodynamic cavitation is a process of bubble nucleation, growth and collapse that frequently occurs in many industrial applications. In the marine industry, uncontrolled cavitation induced by the high rotating speed of the impeller and turbine blade is the major cause of physical erosion to hydraulic equipment [12]–[14]. Furthermore, the level of cavitation noise is an order of magnitude higher than the noise of a non-cavitating flow, which increases the risk of detection of navy ships by torpedoes [15]. On the other hand,

hydrodynamic cavitation has been recently recognized as an energy-efficient process for bubble generation and local energy release. As an example, microbubbles generated through hydrodynamic cavitation can effectively improve the fine particle recovery rates [4]–[6]. The bubbles release high magnitude energy at the instant of burst, making them efficient in water disinfection treatment and enhancing oxidation reactions [7]–[11]. The studies investigating the use of hydrodynamic cavitation in micro-scale have also demonstrated the considerable amount of energy transfer during the vaporization and bubble collapse of cavitating flow, thus unveiled the potential of cavitation in enhancing heat transfer and energy harvesting [126]–[130]. For improving industrial applications due to their different needs, understanding the mechanisms of prevention and promotion of hydrodynamic cavitation is critical.

Controlling the cavitation occurrence requires an understanding of the mechanism of hydrodynamic cavitation. According to Bernoulli's principle, when fluid flows at high speed, the static pressure is lowered. Hydrodynamic cavitation is initiated at a critical flow velocity where liquid ruptures due to the low static pressure. The inception of hydrodynamic cavitation starts from the nucleation and growth of pre-existing nuclei. At a static pressure higher than the saturated vapor pressure, gaseous cavitation could occur due to the diffusion of dissolved gases into nuclei [75], [76]. However, if the size of the low pressure region is limited and nuclei do not possess sufficient time to grow, the static pressure must be further lowered till water surrounding nuclei starts to vaporize for the vaporous cavitation to happen. Due to the liquid surface tension, the critical static pressure must be lower than the saturated vapor pressure to create enough tensile stress for the liquid to rupture. The tensile stress at this point is called the tensile strength of the fluid and is

determined by the sizes of its nuclei content, or "weak points" in the liquid system [51], [55]–[60]. The nuclei as tiny gas pockets are naturally unstable in bulk water due to the Laplace pressure and buoyancy force. However, they have been found to be stabilized on the surface of solid impurities or the walls of containers [131]–[133]. The presence of these pre-existing nuclei provides the opportunity to manipulate cavitation inception by changing their sizes. Liquid free of nuclei can withstand high tensile stresses and resist rupture, making cavitation difficult to happen. On the other hand, in a water body enriched with large nuclei of tens of microns or larger, no measurable tensile strength can be observed, and bubble expansion due to local vaporization occurs almost instantly when the liquid static pressure is lowered to the saturated vapor pressure [134]–[136].

The sizes of gas nuclei could be greatly affected by the concentration of dissolved gases through diffusion. Numerous studies have demonstrated that the increased amount of gas content would promote cavitation and vice versa [76], [137], [138]. Among the different methods to alter the gas content, chemicals could be added into the solution to alter the solubility of dissolved gases. By changing the solubility of a gas-saturated solution, the dissolved gases become supersaturated or undersaturated and tend to enter or leave the undissolved gas clusters (nuclei); thus, nuclei size is altered, and control of the cavitation inception can be achieved. The presence of electrolytes, which are closely related to many applications, especially in the marine industry, can effectively lower the solubility of gases and theoretically affect cavitation inception [139]. Although cavitation studies using saline water have been performed to examine the properties of cavitating bubbles [140], [141], the change in inception was not systematically discussed, and a clear mechanism is still lacking.

In this study, a Venturi tube with an inlet/outlet diameter of 10 mm was used to trigger hydrodynamic cavitation. Considering the complexity and difficulty of visual observation on the cavitation condition in such a small tube, the inceptions were measured using the acoustic detection method, which was sensitive to cavitation on a small scale and wildly practiced in the recent cavitation studies [142]–[146]. NaCl solutions of different concentrations were tested to reveal the ability of salt in promoting cavitation inception. The correlation between dissolved oxygen level and cavitation inceptions of saline water was compared with results using DI water so that the effect of salt-induced gas saturation change on inception was demonstrated. We proposed a mechanism for the cavitation inception change based on the decreased gas solubility. Based on this mechanism, we presented an innovative method of cavitation control by altering the CO_2 solubility in carbonated water via pH change, and the reversibility was tested.

3.2. Material and Methods

3.2.1. Experimental Setup

The schematic of the experimental setup for cavitation inception measurement and the associated testing equipment is shown in **Figure 3.1**. The hydrodynamic cavitation device used in this study is a Venturi tube fabricated using the Formlabs Form2 3D printer equipped with Stereolithography (SLA) technology. The geometry of the Venturi tube was designed with a larger convergent angle (28º) and a lower divergent angle (9º) so that hydrodynamic cavitation could be promoted based on our previous research [50], [147]. The inlet and outlet diameters of the Venturi tube are 10 mm, and the throat diameter is 2.25 mm, with a diameter ratio of 4.44.
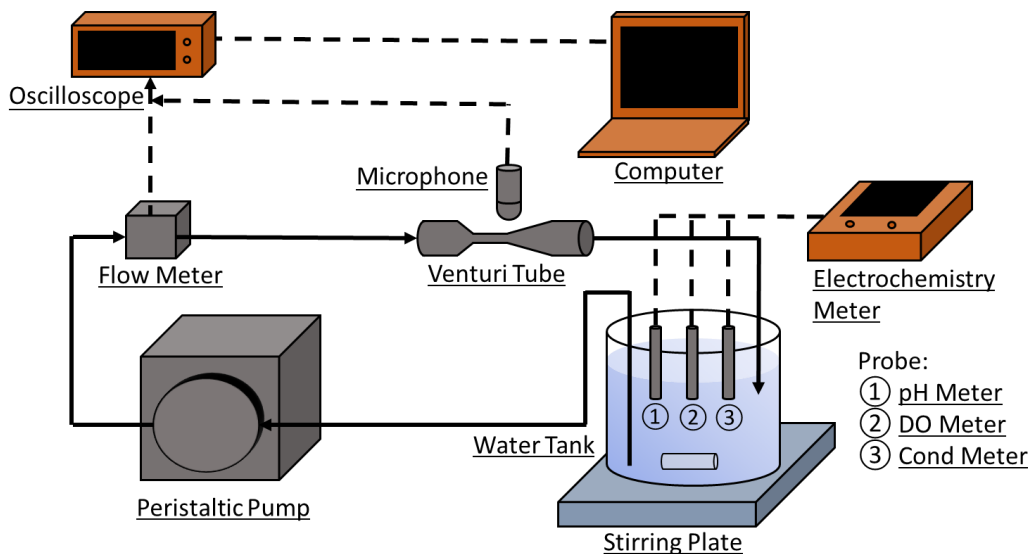
Figure 3.1. Schematic diagram of the experimental setup. Hydrodynamic cavitation was induced by a Venturi tube, and a microphone was placed above to detect cavitation inception. The real-time flow rate was monitored by a flow meter. The properties of the solution in each test were measured using a pH probe, a dissolved O_2 probe, and a conductivity probe placed in the water tank.

For each experiment, one litre of the aqueous electrolyte solution was stored in an open water tank with a diameter of 6 cm and a height of 15 cm. The stirring plate underneath the tank drives a magnetic bar at 200 rpm to homogenize the solution without inducing too much turbulence. Inside the solution, three probes were placed for real-time measurements of water pH, electrical resistance, and dissolved O_2 content. The probes were wired connected to an electrochemistry meter (Orion Versa Star Pro), where the measured parameters can be monitored and recorded at the beginning of each test. Each run of inception test took less than three minutes, and the gas dissolution in such a short period was neglected. A peristaltic pump with adjustable power was used to provide the operating recirculation flow from 0 to 7 L/min, and the real-time flow rate was measured using a

flow meter (Omega type FLR1001) placed downstream of the pump. It delivered signals in the form of voltages, which were monitored by an oscilloscope (Rigol DS1054Z) and converted to flow rate using a lab computer.

3.2.2. Solution preparation

In this study, de-ionized (DI) water was used to prepare the solutions for inception tests. The measured electrical resistance of DI water was in the order of Mega Ohm, which was considered electrolyte-free. To clarify the relationship between gas saturation level and hydrodynamic cavitation inception, air-undersaturated, saturated, and supersaturated DI water was prepared. By maintaining at 60°C while applying vacuum at 0.1 atm for different periods, the air-undersaturated DI water of different gas content was produced. To prevent the temperature effect on gas solubility, the degassed DI water was transferred to a sealed container and stood overnight to recover the operating temperature at 20°C before use. The air-saturated DI water was produced by purging air into the fresh DI water overnight. For the air-supersaturated water, excessive air was compressed into DI water at 1.5 bar in a sealed container. As the air-supersaturated water was discharged from the pressurized container, excess air was released from the liquid in the form of bubbles. The air saturation level of solutions after different treatments was calculated from the ratio of measured O_2 content over the solubility of O_2 following the O_2 solubility equation [148]:

$$O = 1.429 \exp \left[-173.429 + 249.645 \frac{100}{T} + 143.348 \log \left(\frac{T}{100} \right) - 21.849 \frac{T}{100} \right.$$
$$\left. + S \left(-0.0331 + 0.0142 \frac{T}{100} - 0.0017 \left(\frac{T}{100} \right)^2 \right) \right] \frac{P_O}{P_{OA}}$$

(3.1)

where O is the dissolved O_2 concentration at saturation [mg/L], S is salinity [‰], and T is temperature [K]. Although bubble burst releases high-magnitude energy in the local area, it has a negligible effect on the temperature of the entire water system and is generally regarded as an isothermal process [114], [149]. Thus, the experiments were performed in the constant lab temperature controlled at 20°C. P_O is the ambient pressure in the water tank and is also regarded as the pressure of the Venturi outlet. Using the DO meter probe associated with the electrochemistry meter, P_O was measured to be 705 mmHg in Edmonton, AB, where experiments were conducted. P_{OA} is the atmospheric pressure at sea level. From Eq. 3.1, the O_2 solubility in DI water in the operating condition (20 °C, 705 mmHg and 0 salinity) is 8.42 mg/L.

In the study of salt effect in cavitation inception, NaCl was added into the DI water to produce 0-1000 mM NaCl solution. When electrolytes are introduced into water, the dissolved salt ions attract water molecules, leaving fewer hydrogen and oxygen ions to dissociate gas molecules. As a result, the ability of water to dissolve gases decreases, and the gas-saturation level increases [150]. This theory could also be reflected from Eq. 3.1 that, as the water salinity increases, the solubility of oxygen decreases. As a result, the air-saturated DI water after NaCl addition became air-supersaturated. To eliminate the effect of gas saturation level on inception, air-saturated salt solutions were prepared by purging air into the degassed salt solutions overnight.

Table 3.1. Properties of NaCl solution samples.

Batch Number	Sample ID	NaCl Conc (mM)	O_2 Solubility (mg/L)	Dissolved O_2 Content (mg/L)	O_2 Saturation Level
1	1	1	8.42	4.47	0.53
	2	10	8.39	4.65	0.55
	3	20	8.37	4.83	0.58
	4	50	8.29	5.1	0.62
	5	100	8.16	5.34	0.65
	6	200	7.91	5.78	0.73
	7	500	7.20	6.12	0.85
	8	800	6.56	6.73	1.03
2	1	100	8.24	4.42	0.55
	2	200	7.99	4.71	0.60
	3	400	7.51	5.18	0.70
	4	600	7.05	6.12	0.89
	5	1000	6.22	6.41	1.01

To obtain the relationship between cavitation inception and air-saturation level after salt addition, NaCl was gradually added to degassed DI water, and inception tests were performed at each concentration. Two batches of degassed DI water of the same treatment were prepared for the purpose of reproducibility. **Table 3.1** summarizes the gas content of NaCl solutions after each step of salt addition. The saturation level shown in **Table 3.1** was calculated from the ratio of measured O_2 content to the O_2 solubility using Eq. 3.1 with the

consideration of salinity, where salinity was obtained from the measured solution electrical resistance [151]. Throughout the experiments on both batches of solutions, the dissolved O_2 contents had obvious increases, which was due to the inevitable diffusion of air carried by the NaCl particles, as well as air diffusion at the water-air interface during flow circulation and agitation.

CO_2, with the solubility almost 36 times higher than that of O_2 in water [152], and high dissolution sensitivity to pH change, makes it a great candidate for cavitation controlling. In the last section, inception tests were performed on carbonated water, which was prepared by injecting compressed CO_2 into DI water. The freshly made carbonated water was CO_2 supersaturated, where bubbles kept forming at the wall of the containers. The equilibrium reactions associated with CO_2 dissolving into DI water are shown in Eq. 3.2 and 3.3. When CO_2 was injected into water, aqueous CO_2 and H_2CO_3 were formed. The pH of freshly made carbonated water was 4.1. In DI water at such pH, over 99% of CO_2 in water existed in the form of $CO_{2(aq)}$ [153], which was unstable and could be easily transformed into CO_2 gas. The amount of CO_2 existing in one litre of this solution was equivalent to 6.54×10^{14} microbubbles with a diameter of 50 μm or one large bubble of 5.5 cm in diameter, sufficient for promoting cavitation. As the water pH increased, the dissolved CO_2 in the form of H_2CO_3 further underwent several equilibrium reactions, where deprotonation occurred to form bicarbonate and carbonate.

$$CO_{2(aq)} + H_2CO_3 \overset{K_1}{\leftrightarrow} H^+ + HCO_3^- \tag{3.2}$$

$$H^+ + HCO_3^- \overset{K_2}{\leftrightarrow} H^+ + CO_3^{2-} \tag{3.3}$$
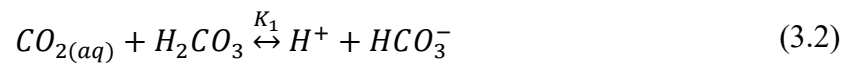
K_1 and K_2 are the equilibrium constant, respectively, and their values as a function of temperature and water salinity are given by [152]

$$pK_1 = 3670.7\frac{1}{T} - 62.008 + 9.7944\ln(T) - 0.0118S + 0.000116S^2 \qquad (3.4)$$

$$pK_2 = 1394.7\frac{1}{T} + 4.777 - 0.0184S + 0.000118S^2 \qquad (3.5)$$

Aqueous $CO_{2(aq)}$ and H_2CO_3 are volatile forms of CO_2 in water and can be easily gasified during the cavitation process. Having the pH and K_1, K_2 known, the fraction of aqueous $CO_{2(aq)}$ and H_2CO_3 over the total dissolved CO_2 content, f_a can be calculated based on

$$f_a = \frac{[H^+]^2}{[H^+]^2 + [H^+]K_1 + K_1K_2} \qquad (3.6)$$

3.2.3. Acoustic Inception Measurement

In this study, the hydrodynamic cavitation inceptions were detected using an acoustic sound-recording approach. During each experimental run, the water flow was gradually increased from the non-cavitating condition to the critical inception value. At this point, water molecules surrounding the nuclei were experiencing a critical low static pressure inside the Venturi throat and evaporated. The nuclei expanded in a short period, followed by a rapid collapse when the pressure recovered at the throat end, as vapor inside the bubble condensed. Such inward motion and subsequent momentum of the surrounding water drove the bubbles to oscillate drastically and radiated sound waves at an order of magnitude higher than the level of non-cavitating flow [154]. This phenomenon has been utilized as a promising method for the inception measurement [51], [142]–[144].

As shown in **Figure 3.1**, a high-performance microphone (Florida Research Instrument 100-1) was placed right above the throat of the Venturi tube to record the sound signals at 50k samples/s. The real-time sound signals were measured for half a second at the rate of one time per three seconds during cavitation tests, and each measurement was recorded in the form of the power spectrum against frequency using MATLAB. The ambient noise, e.g. the noise from the peristaltic pump, could potentially disturb the acoustic power spectrum, especially at high flow rates. To eliminate the interference, the pump was first operated without the connection of the Venturi tube, and the frequency range of the pump noise spectrum was obtained. By applying a frequency filter targeting the ambient noise, the acoustic power spectrum solely affected by cavitation was generated. To differentiate the cavitating and non-cavitating flow, sound signals before and after cavitation were recorded and compared. An obvious jump over 4 mW in signal amplitude was observed as the flow reached the cavitating state. Therefore, sound signals that had amplitude over 4 mW were regarded as cavitating signals, and their fraction among the 25k sound signals recorded at each measurement was calculated as the level of cavitation, termed cavitation probability [145].

Three sample inception experiments were performed using tap water, air-saturated DI water, and degassed DI water to demonstrate the feasibility of the sound detection method. The tap water was under pressure during pipe transportation, thus was enriched with air based on Henry's law and was expected to be air-supersaturated in the atmosphere [74]. In each experiment, the water flow rate was first kept low at a non-cavitating condition. As the flow rate increased to a critical value, cavitating sound signals started to emerge. The cavitation probability was gradually increased from zero to one with the increasing flow

rate. To quantify and compare the cavitating conditions, the level of fluid velocity was represented by the dimensionless number termed cavitation number σ defined in the equation below:

$$\sigma = \frac{P_o - P_v}{\frac{1}{2}\rho V^2} \tag{3.6}$$

where P_v is the saturated vapor pressure at 20 °C operating temperature, ρ is the liquid density with consideration of water salinity, and V is the characteristic throat velocity calculated by dividing the flow rate by the Venturi throat area. As shown in **Figure 3.2,** the cavitation probability and its relationship with cavitation number display a cumulative normal distribution defined as:

$$f = \frac{1}{2}\left\{1 + \mathrm{erf}\left[\frac{(\mu - x)}{s\sqrt{2}}\right]\right\} \tag{3.7}$$

where erf is the error function. By fitting the cavitation probability and the associated cavitation number into f and x, the mean (μ) and variance (s) of the distribution can be obtained. In **Figure 3.2**, cavitation probabilities of three types of water were plotted against cavitation number. Each group consisted of three experimental runs to generate a more representative result. From the definition that inception is determined by the largest nuclei in the fluid [154], the cavitation number when cavitation initiated is a good estimate of inception. As shown in the figure, μ, which marks 50% of qualified samples, was not an accurate representation of the inception, especially for water with a high inception number and low s. However, μ could be used as an anchor point to plot a straight fit line, and the inception was obtained as its interception with the x-axis. As the marks indicated in the

46

figure, the cavitation number at inception was presented in terms of cavitation inception number, where a higher number represents an easier or promoted hydrodynamic cavitation.
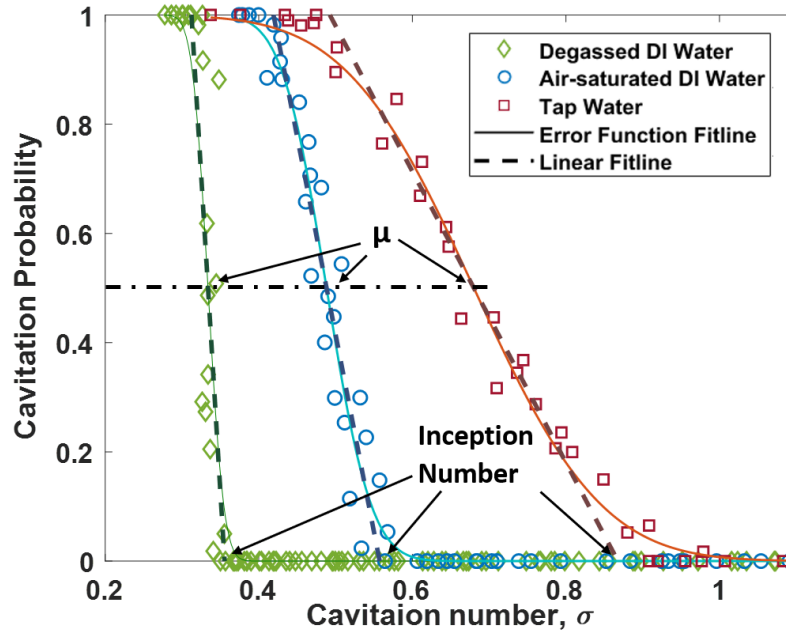
Figure 3.2. Cavitation probability measurement with air-undersaturated/degassed DI water, air-saturated DI water and air-supersaturated tap water. Experimental data were measured using a microphone and fitted using error functions to obtain the anchor points μ. The cavitation inception numbers were regarded as the interceptions between the x-axis and the straight fitting lines that passed through μ.

It is known that the tensile strength of a liquid is inversely proportional to the size of the nuclei present in the system according to the bubble nucleation theory. In other words, the inception of cavitation is highly sensitive to the size and population of pre-existing nuclei. Hydrodynamic cavitation, as a technique widely used for bubble generation, may generate nuclei that potentially survive from the flow circulation during experiments and interfere with the following inception tests. To avoid this issue, three methods were used

to prevent the recirculation of cavitation bubbles: (1) The suction tube was placed at the bottom of the water tank, whereas the discharge tube was placed near the surface so that the bubbles generated during the cavitation process left the system without interfering with the cavitation measurement. (2) Hydrodynamic cavitation was turned off quickly once the inception was reached so that only a small number of cavitation bubbles were generated in each trail. (3) Since a bubble with a size of 50 μm would take about 2 min to exit a 0.1 m height water body from the tank bottom [155], the system was allowed to rest for at least 2 min between each experimental run so that microbubbles had enough time to exit the water system.

3.3.   Results and Discussion

3.3.1. NaCl effect on hydrodynamic cavitation inception

As discussed in Section 2.2, NaCl addition to air-saturated DI water would make it supersaturated. In this section, hydrodynamic cavitation inception tests were performed on the air-supersaturated solutions of different NaCl concentrations to demonstrate the effect of salt addition on promoting cavitation. As the reference, NaCl solutions of controlled air-saturation levels were also tested to investigate the effect of salt property without the influence of the gas saturation level.

The comparison of the cavitation inception number between air-supersaturated water and air-saturated water was plotted in **Figure 3.3**. By adding NaCl to air-saturated DI water, the air-solubility was reduced while the dissolved air content remained the same; as a result, the solution became air-supersaturated. The excess air diffused into local nuclei to form small bubbles, which reduced the tensile strength of the liquid and promoted cavitation. As

to prevent the recirculation of cavitation bubbles: (1) The suction tube was placed at the bottom of the water tank, whereas the discharge tube was placed near the surface so that the bubbles generated during the cavitation process left the system without interfering with the cavitation measurement. (2) Hydrodynamic cavitation was turned off quickly once the inception was reached so that only a small number of cavitation bubbles were generated in each trail. (3) Since a bubble with a size of 50 μm would take about 2 min to exit a 0.1 m height water body from the tank bottom [155], the system was allowed to rest for at least 2 min between each experimental run so that microbubbles had enough time to exit the water system.

3.3.   Results and Discussion

3.3.1. NaCl effect on hydrodynamic cavitation inception

As discussed in Section 2.2, NaCl addition to air-saturated DI water would make it supersaturated. In this section, hydrodynamic cavitation inception tests were performed on the air-supersaturated solutions of different NaCl concentrations to demonstrate the effect of salt addition on promoting cavitation. As the reference, NaCl solutions of controlled air-saturation levels were also tested to investigate the effect of salt property without the influence of the gas saturation level.

The comparison of the cavitation inception number between air-supersaturated water and air-saturated water was plotted in **Figure 3.3**. By adding NaCl to air-saturated DI water, the air-solubility was reduced while the dissolved air content remained the same; as a result, the solution became air-supersaturated. The excess air diffused into local nuclei to form small bubbles, which reduced the tensile strength of the liquid and promoted cavitation. As

shown in **Figure 3.3**, freshly-made air-saturated DI water had a cavitation inception number of 0.53. When NaCl was added to reach the concentration of 50 mM, the inception number was significantly increased to 0.78. The cavitation inception number reached almost 1 at 200 mM NaCl, which indicates the presence of large micro-bubbles, and cavitation happens almost instantly when the threshold pressure drops to the saturated vapor pressure. These results demonstrated that the addition of NaCl into air-saturated DI water could effectively promote the inception of hydrodynamic cavitation.
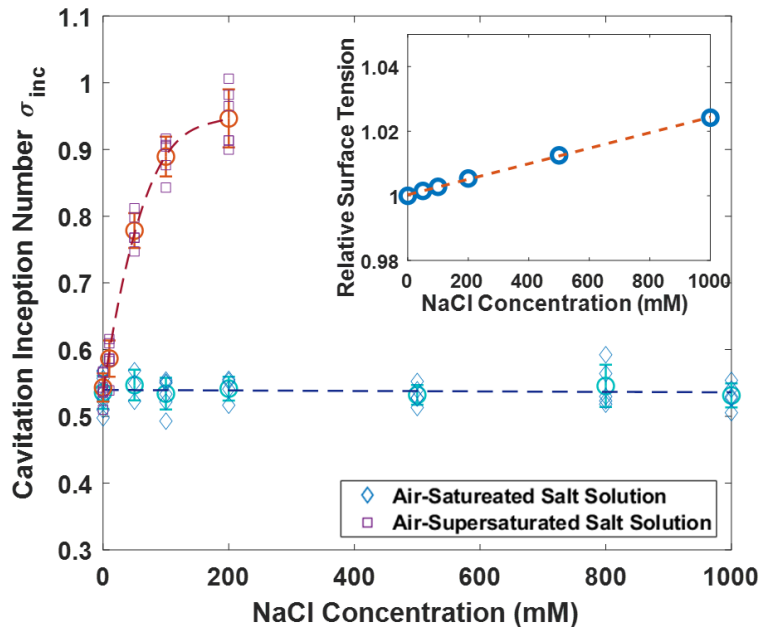
Figure 3.3. The effect of NaCl on hydrodynamic cavitation inception in air-supersaturated solution and air-saturated solution. The circle and error bar were plotted to represent the average and standard deviation of inceptions. Inset shows the NaCl effect on solution surface tension with data obtained from Jones and Ray (1941) [156].

Different from the promoted cavitation with air-supersaturated salt solution, the inception number remained almost constant at 0.53 using the air-saturated salt solutions

from 0 to 1000 mM, indicating a minimal effect of salt on cavitation inception without air-supersaturation. Based on Blake's theory, the tensile strength of fluid is mainly related to the air-water surface tension and the nuclei size [134]. In **Figure 3.3 inset**, the salt concentration effect on surface tension was plotted [156]. As the NaCl concentration was increased from 0 to 1000 mM, there was about 2.5% increase in relative surface tension, which was negligible for inception change. From the perspective of nuclei size, the increase in salinity helped stabilize bubbles from coalescence; thus is expected to have little effect on the sizes of already stabilized microbubbles in this study [157]. As both the water surface tension and pre-existing bubbles size do not change significantly with salinity, NaCl was demonstrated to have little effect on promoting cavitation if the effect air-saturation level was not considered.

3.3.2. Effect of air saturation level on hydrodynamic cavitation inception in DI water and NaCl solution

From the previous discussion, the effect of salt addition on promoting the inception of hydrodynamic cavitation is expected to be due to the supersaturation of dissolved gases in water. By obtaining the correlation of air saturation level with the cavitation inception number and compare the results using DI water and salt solution, the mechanism of salt in promoting cavitation could be further elaborated. Cavitation inception tests were performed using the prepared air-supersaturation, saturation and undersaturation DI water samples with different saturation levels. In **Figure 3.4**, the relationship of inception *vs* water saturation level is plotted. The fitting line in the air-undersaturated region is the linear fitting of the average inceptions. For the air-supersaturated solutions, excess air did not

contribute to a higher air saturation level. Instead, the gases diffused into local nuclei to generate bubbles. As a result, the final air saturation levels were confined at around 1, with a rich number of micro-bubbles present in the solution. The inset of **Figure 3.4** shows the size distribution of bubbles in one of the air supersaturation water samples measured using Malvern Mastersizer 3000. With the mean bubble diameter of 50 µm, the tensile strength of such liquid is about 2 kPa based on Blake's equation, which is quite low considering the tensile strength of many water samples in the order of mega-Pascal [73], [135], [138], [158]. The generated micro-bubbles greatly promoted cavitation inception, as shown in the increase of inception number. For air-undersaturated DI water, the inception number increased in a linear manner with saturation level in the tested range, which was expected to be caused by the increase in nuclei size [153], [159].
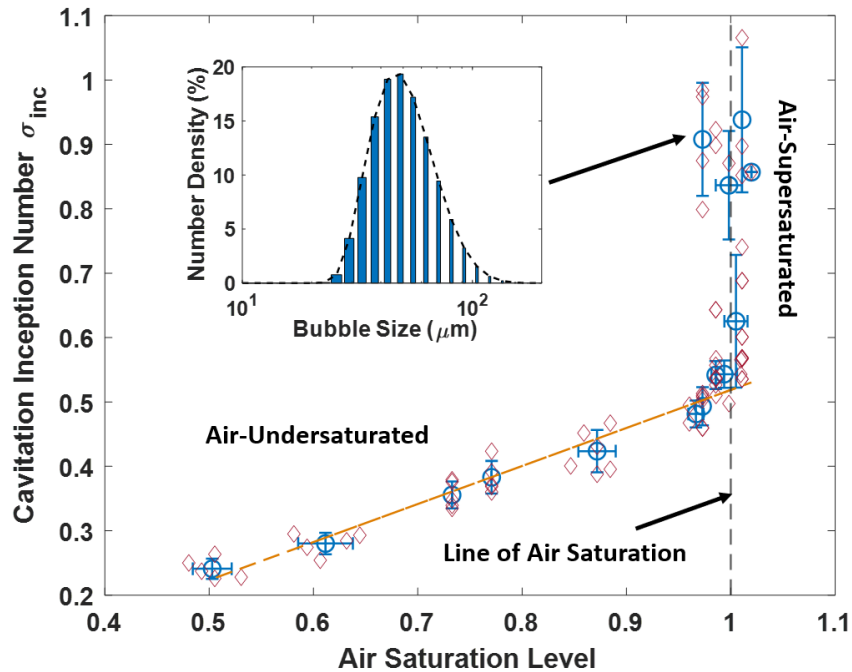
Figure 3.4. Hydrodynamic cavitation inception number *vs* air saturation level in DI water. Inset shows the size distribution of bubbles in one of the air-supersaturated solutions.

Figure 3.5 shows the inception cavitation number as a function of air saturation level, using NaCl solutions prepared in **Table 3.1**. Each data point includes five test runs with the correspondent NaCl concentrations labelled aside. The linear fitting line obtained from the air-undersaturated region in **Figure 3.4** was plotted as the reference line in **Figure 3.5**. From the figure, not only the results of the two batches of samples showed good reproducibility, the inceptions of degassed water after salt addition also showed good agreement with the fitting line from **Figure 3.4**. As salt was gradually added to the solution, the solution air-saturation level increased. The cavitation inception number increased following a similar trend obtained from the DI water tests. As the NaCl concentrations of two batch samples were increased to 800 and 1000 mM, the measured oxygen contents were 6.6 and 6.2 mg/L, which were much less than the oxygen saturation level in DI water at 8.4 mg/L. Despite that, the cavitation inception number showed an obvious jump from the trend line, which indicated supersaturation of the solution and the presence of larger nuclei which promoted hydrodynamic cavitation. The results confirmed the ability of NaCl in reducing gas solubility and increase the gas saturation level in the water, thus promoting hydrodynamic cavitation.
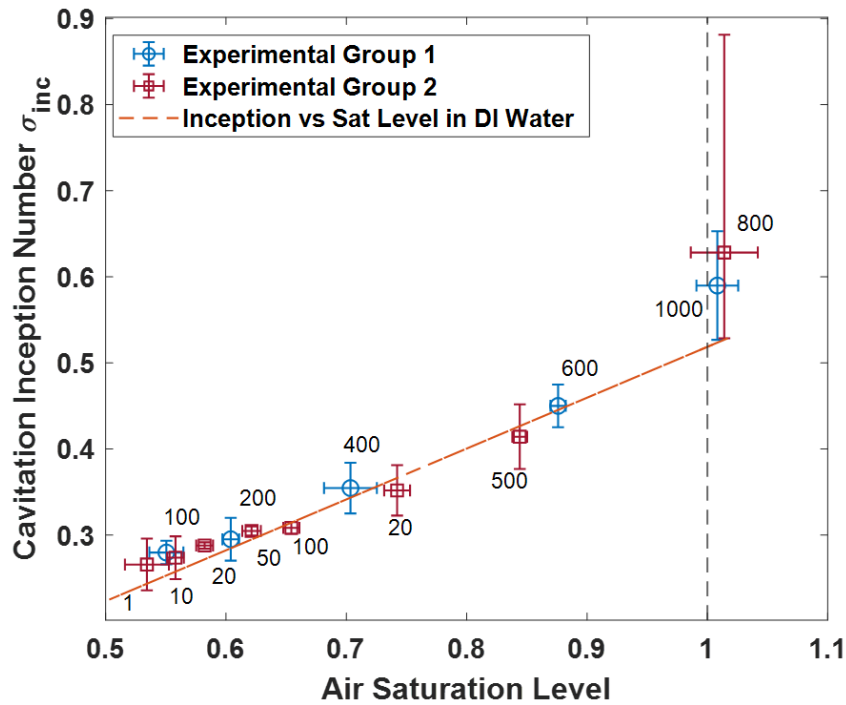
Figure 3.5. Hydrodynamic cavitation inception number *vs* air saturation level in NaCl solutions. Two groups of experimental tests were conducted to show the reproducibility. The NaCl concentrations in mM were labelled beside each data set. The fitting line of inception *vs* air saturation level was obtained from Figure 3.4 using DI water.

3.3.3. Controlling the cavitation inception by changing the pH of carbonated water

As the air saturation level was the major cause of inception change, the transaction of gases between the dissolved aqueous status and the nuclei bubble status provides a promising method to control the inception. In this study, CO_2, with the advantage of highly dependent solubility on solution pH, was chosen as an agent for hydrodynamic control. Hydrodynamic cavitation tests were performed using carbonated water prepared in section

2.2, and the inceptions were recorded as a function of pH. Considering the aqueous CO_2 and H_2CO_3 as the unstable component that could be easily gasified during the cavitation process, inceptions numbers were also presented against f_a, which represented the fraction of aqueous CO_2 and H_2CO_3 over the total dissolved CO_2 content. In this section, the increase in dissolved CO_2 content reduced the water solubility of O_2, resulting in little O_2 content of about 3 mg/L in the freshly-made carbonated water. Considering the little correlation between the solubility of O_2 and N_2 with pH, the effect of gases other than CO_2 can be neglected in this section.

Figure 3.6a shows the cavitation inception number of carbonated water at different pHs. A clear downward trend can be observed with the increase in pH. The inset of **Figure 3.6** shows the relationship of f_a with pH in the ideal solution using Eqs. 3.4 to 3.6. At pH lower than 5.5, the inception number was larger than 1. At this stage, $CO_{2(aq)}$ was greatly supersaturated, with visible bubbles continuously forming on the container wall. The rich amount of gas bubbles led to gaseous cavitation even though the pressure inside the bubble is higher than the saturated vapor pressure [15], [76]. As NaOH was added to the solution and deprotonation progress carried on, dissolved $CO_{2(aq)}$ was converted to the form of bicarbonate and carbonate. The solution gradually transformed from $CO_{2(aq)}$ supersaturated to undersaturated. As a result, $CO_{2(g)}$ gas nuclei dissolved into the solution, leaving little nucleation sites for the cavitation to start. The inception curve continued to drop until the pH was increased to around 8, while further increase in pH to 9.5 showed no change in inception. The result agrees with the inset of **Figure 3.6a** that the minimum fraction of dissolved CO_2 was reached at pH around 8.
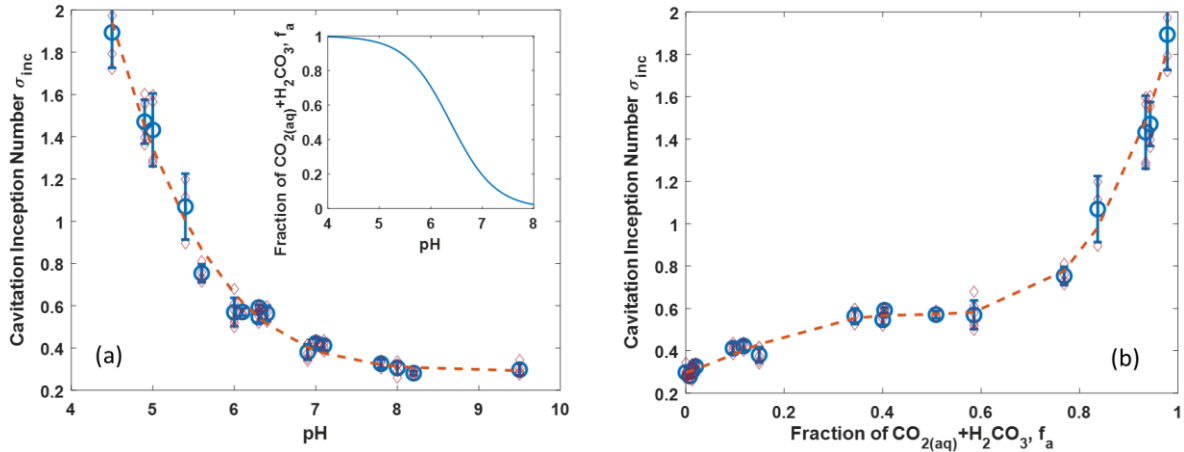
Figure 3.6. The change of cavitation inception with different: (a) pH and (b) fraction of aqueous CO_2 and H_2CO_3 over the total dissolved CO_2, f_a in carbonated water. Inset in (a) shows the relationship between f_a with pH in a saline-free ideal solution.

The curve of cavitation inception number *vs* f_a is shown in **Figure 3.6b.** As NaOH and HCl were added to change the solution pH, the electrical resistivity of the solution gradually decreased, which indicated the accumulation of sodium and chloride electrolytes. Therefore, the water salinity was considered when calculating the fraction of dissolved CO_2 at each pH using Eqs. 3.4 to 3.6. As **Figure 3.6b** shows, when most of the CO_2 content existed in the form of carbonate or bicarbonate instead of aqueous CO_2, the hydrodynamic cavitation was extremely difficult to happen with an average inception number of 0.3. As f_a increased, the carbonated water gradually became gas saturated when f_a reached 0.34. In the middle region where f_a increased from 0.34 to 0.59, the inception number remained constant at 0.55, close to the inception number of air-saturated DI water. The variation of f_a in this region was mainly due to the change of solution resistivity from 350 to 4000 Ohm, while the pH of corresponding samples merely increased from 6 to 6.4. Therefore, comparing to f_a, pH appears to be a more direct parameter for the inception change. As f_a

55

further increased, the same phenomenon as the air-supersaturated water was shown, that visible micro-bubbles were present in the solution to promote cavitation.

After demonstrating the effect of CO_2 solubility on cavitation inception of carbonated water, the reversibility of this method was tested, and the results are presented in **Figure 3.7**. One litre of fresh DI water at pH 7 was carbonated to pH 4.4, followed by the addition of NaOH and HCl to tune the solution pH. The target conditions were chosen to be pH 4 and 8, where the fractions of dissolved CO_2 were close to 1 and 0 as shown in **Figure 3.6**. Such a process was repeated five times, and the inception number reached similar high and low values within the experimental runs. The result demonstrates that changing the CO_2 solubility in carbonated water via pH control is not only effective in controlling the inception of hydrodynamic cavitation, but the method is also highly reversible.
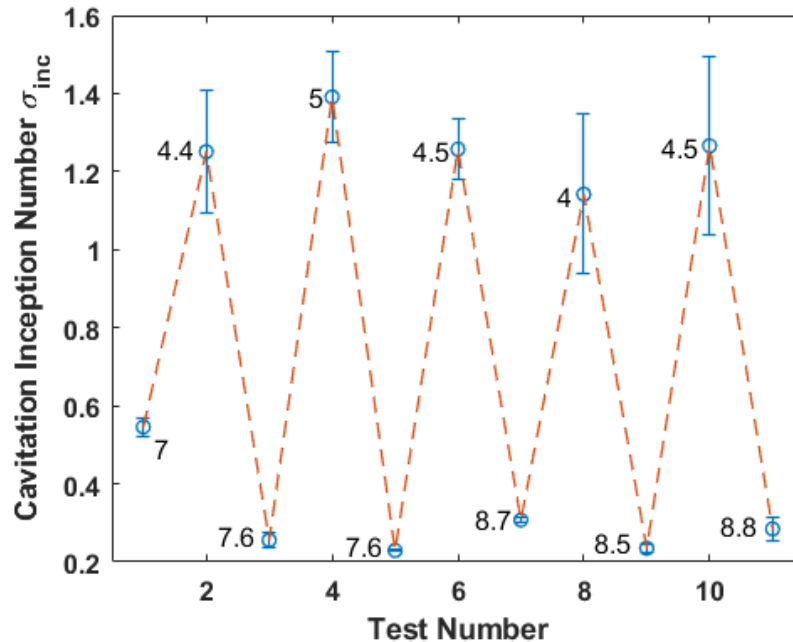
Figure 3.7. Reversibility tests of cavitation inception controlled by changing the pH of carbonated DI water. The pH of each water sample was labelled beside it.

3.4. Conclusions

In this study, we observed that hydrodynamic cavitation inception of aqueous solutions was promoted with the addition of NaCl. With a minimal change in inception for air-saturated salt solutions with different NaCl concentrations, the major cause of inception promotion was the decrease in gas solubility when salt was introduced to the solution. The excess gas entered pre-existing nuclei, which consequently lowered the liquid tensile strength and promoted cavitation. The inception number gradually increased with salt addition when the solution was air undersaturated. Once the solution became air saturated, further addition of salt induced large nuclei that greatly increased the inception number. Knowing the gas saturated level to be the major reason for inception change, the method of altering the CO_2 solubility in carbonated water via pH change was suggested to be a promising technique for controlling the cavitation inception. Moreover, the reversibility of this method was demonstrated and can have implications on the industrial applications that require early or late hydrodynamic cavitation.

Chapter 4 Effect of Solid Wettability on

Three-Phase Hydrodynamic Cavitation

Abstract

In many modern industrial applications such as mineral flotation and water treatment, microbubbles have been used as an efficient aid for increasing the collision and attachment efficiencies and enhance the recovery of valuable fine minerals. One technique to produce such micro-bubbles is to use the hydrodynamic cavitation process when gas cavities in water nucleate under low hydrodynamic pressure. To better understand the cavitation behavior in the presence of solids with different surface properties, we present an experimental study of a multi-phase system. The characteristics of hydrodynamic cavitation with a Venturi tube were experimentally investigated using acoustic detection. The effect of both particle and tube wall surface hydrophobicity and surface structure on the inception of hydrodynamic cavitation were considered. Results demonstrated that particles with lower wettability promoted hydrodynamic cavitation by efficiently trapping gas pockets that facilitate bubble nucleation. In addition, in the condition of low particle concentration (5 g/L) and fine particle size range (D50 < 20 μm), parameters including size and roughness did not play a critical role in affecting cavitation inception. Finally, tests using Venturi tubes of different surface properties showed that the wall surface behaves similarly as particles. Hydrodynamic cavitation was promoted by a more hydrophobic Venturi tube which screened the effect of particle surface properties. Highlights in this study are expected to provide insight into the bubble generation mechanism under different solid conditions and to potentially achieve both high recovery and selectivity of fine particle flotation.

4.1. Introduction

Froth flotation is a widely-used technology in which hydrophobic mineral particles are attached to air bubbles and separated from the hydrophilic particles [110], [160], [161]. This process reaches a high efficiency for particles with sizes ranging from tens to hundreds of micrometers. However, recovery of fine particles remains challenging due to the limited probability of particle-bubble collision [30], [32], [33], [36]. Aiming to increase the bubble/fine-particle collision probability, techniques such as oil-assisted flotation, carrier flotation, shear flocculation and selective polymer flocculation have been reported [162]–[164]. The use of micro-bubbles (hundreds of nanometers to tens of micrometers) is a promising technology in promoting particle collection efficiency for two main reasons [5], [47]. First, the generation of micro-bubbles on the particle surfaces acts as bridges that can significantly enhance the attachment probability between particles and flotation-sized bubbles [45]–[47]. Second, the micro-bubbles benefit the flotation process by promoting the aggregation of fine particles and increasing the bubble-particle collision probability [4], [48], [49]. The overall flotation recovery can be effectively improved with massive micro-bubbles. Hydrodynamic cavitation, as a simple and energy-efficient technology for micro-bubble generation [8], [50]–[52], shows great potential in the flotation process.

In hydrodynamic cavitation, the liquid flow experiences a kinetic energy rise in the Venturi throat, causing a corresponding decrease in pressure. In a confined low-pressure space where nuclei do not possess enough time to grow by gas diffusion, a critical low pressure must be reached so vaporous cavitation can happen. This critical pressure is called the tensile strength of the liquid [54], [57], [165]. In an ultra-pure mono-phase water system, an extremely large tensile strength has been reported at around 240 MPa [51]. However,

the threshold for ordinary water is far lower than this value and is only slightly below the vapour pressure. This difference has been rationalized by the presence of pre-existing cavitation nuclei or micron-size bubbles stabilized by impurities. Previous research has demonstrated that the required tensile strength for gas nucleation can be lowered by decreasing the liquid-gas interfacial tension and increasing gas nuclei sizes. Therefore, hydrodynamic cavitation can be enhanced by the presence of particles that accommodate surface bubbles [1], [53], [54], [166]–[168]. Many research studies have been performed in the recent decades for the application of hydrodynamic cavitation in the improvement of fine particle recovery[5], [44], [47]. However, the fundamental understanding of the mechanism of hydrodynamic cavitation in a three-phase system and the corresponding effect on flotation selectivity remain unclear and requires further investigation. Of particular interest is the change of three-phase hydrodynamic cavitation behaviors with different solid properties.

In this study, we investigate the effective parameters and mechanism of both slurry particles and tube walls on promoting the inception of three-phase cavitation. To achieve this goal, hydrodynamic cavitation inception tests were first performed using a glass-made Venturi tube with high wettability to study the effect of particle properties on cavitation inception without interference from the tube wall. The cavitation inceptions were detected using an acoustic detection approach, where the results of particles with different wettabilities, sizes and surface roughnesses were investigated and compared. The particle wettability, as the most effective parameter, was proposed to affect cavitation by involving gas pockets rather than the particle property itself. To demonstrate this idea, the particles of different wettabilities were tested after gas pocket elimination treatment, and the results

were compared with slurries without any treatment. In the last section, the influence of tube wettability on three-phase hydrodynamic cavitation was investigated. Inceptions with particles of different wettabilities were compared between a glass tube and a 3D-printed Venturi tube with lower surface wettability. The screen effect of the tube wall on particle wettability effect was analyzed. This study aims to obtain a better understanding of the behaviors of both particle and Venturi tube walls in three-phase hydrodynamic cavitation.

4.2. Material and Methods

4.2.1. Equipment setup

Using a peristaltic pump, the slurry carried through a Venturi tube as shown in **Figure 1a**. A magnetic stirring bar with a stirring plate placed underneath the mixing tank was used for particle-water mixing. The rotating speed of the stirring bar was kept at 450 rpm in each test for consistency. A flow meter (Omega type FLR1001) was placed in front of the Venturi to measure the flow rate. The voltages were monitored by an oscilloscope (Rigol DS1054Z) and converted into liquid flow rate in post-treatment. The flow meter emitted infrared light and received the reflection back from a turbine wheel driven by the slurry flow. Particle slurries for each test were prepared at a concentration of 5 g/L, by which the light transmittance was not blocked for high flow meter performances. To minimize particle blockage effect on infrared light transmission, calibration was performed for each experiment with particle slurry.
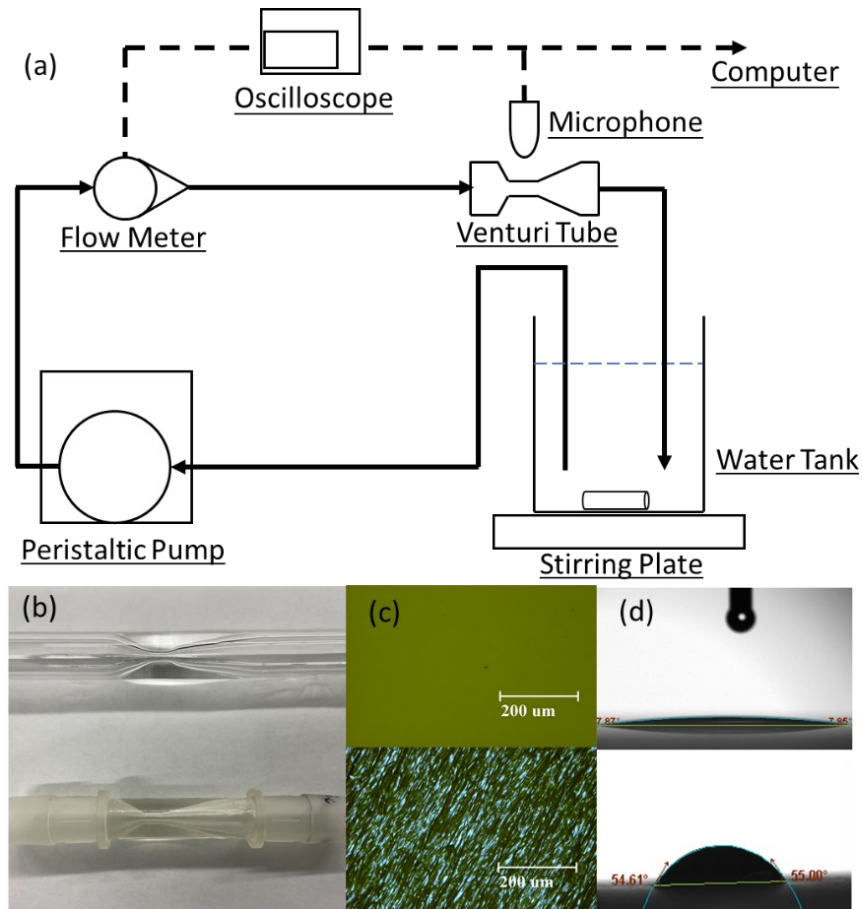
Figure 4.1. (a) Schematic diagram of the experimental setup. (b) Images of glass Venturi tube (top) and 3D printed Venturi tube (bottom). (c) Microscope images and (d) Tensiometer contact angle measurement of the corresponding material.

4.2.2. Hydrodynamic cavitation device

Two Venturi tubes were used in this study to induce hydrodynamic cavitation. In the experiments targeting the effect of particle property on hydrodynamic cavitation, the glass-made Venturi tube shown at the top in **Figure 1b** was used. The glass material had a relatively smooth surface with high wettability, as the 10x microscopic imaging and Tensiometer (Attension Theta Lite) contact angle measurement showed in the top of

Figure 1c and **Figure 1d**. Such a tube wall is expected to have a nuclei-free surface, which barely promotes bubble nucleation. Without interference from tube wall properties, the glass Venturi tube is ideal for studying the effect of particle properties. A second Venturi tube was fabricated using the Formlabs Form2 3D printer equipped with Stereolithography (SLA) technology, as shown at the bottom of **Figure 1b**. To minimize the geometry difference between the two tubes, the 3D printed tube was designed with similar parameters as the glass tube, with 10 mm inlet diameter, 2.2 mm throat diameter, 21° convergent angle and 9° divergent angle. Both tubes were fabricated with inlet and outlet extensions that were joint to the half-inch recirculation hoses. Although the SLA technology uses lasers to solidify photo-sensitive liquid material and is a well-known technology for high-resolution fabrication [169], a relatively rough surface was observed under the 10x microscopic imaging compared to the glass material. Furthermore, the contact angle measurement shows a more hydrophobic surface with a contact angle of 55°. In the study of the Venturi wall's effect, particles with different properties were tested with both tubes, and the cavitation inceptions were compared.

4.2.3. Particle preparation and characterization

In the three-phase cavitation study, silica particles were used to prepare the slurry due to their easy size control and wettability modification. By grinding the crystalline bulk silica using a Shatter Box and following sieving, three patches of silica particles with different sizes were obtained. The particle sizes were measured using Mastersizer 300, and the average result of three tests for each patch is listed in **Table 4.1**. With the mean sizes of less than 20 μm from the Mastersizer 3000 measurement, these silica particles were

selected to represent the fine particles that are problematic in the mineral flotation processes [36]. As a reference to the rough silica particles, spherical glass beads purchased from Kisker Biotech GmbH & Co. were also tested in the effect of particle surface roughness study. The SEM images of patch 3 silica particles and glass beads are shown in **Figure 4.2**, with 100 μm scale bars for the left images and 40 μm scale bars for the zoomed right images. The glass beads have a spherical shape with relatively smooth surfaces, while the silica images show obvious irregular shapes with creviced surfaces that are potential sites for surface gas nuclei.

Besides the particle surface structures, wettability also plays a crucial role in the presence of surface nuclei. For wettability modification, the dry silica particles and glass beads were placed into the 0.2 vol% dichlorodimethylsilane (DDMS) in toluene solution[170]. During the treatment, DDMS peeled off the hydrophilic hydroxyl group from the silica surface and substituted it with a layer of methyl groups repulsive to water molecules, and a longer treatment period led to lower wettability.

As direct contact angle measurement on fine particles is difficult, flat silica wafers as references were silane-treated with particles, and their contact angles before and after treatment were measured. The contact angles are listed in **Table 4.2**, where the values are summarized from three tests for each sample. Before treatment, the contact angles of clean silica wafers were measured to be less than 10°, indicating a relatively clean surface. After 10 s, 30 s and 120 s of silane treatment, the contact angle of the clean silica wafers roughly increased 20° between each step leading to 35°, 54° and 73°, respectively. In this study, despite the contact angle of silane-treated particles never exceed 90°, they are referred as "hydrophobic" particles in the results and discussion section for differentiation from the

bare silica particles. Although the apparent wettability of silica particles is a combination of surface roughness and material hydrophobicity, and the contact angles of silica wafers could not fully represent the contact angles of the particles, this contact angle measurement provides a general trend of the particle wettability.

Table 4.1. Sizes of the tested particles

Particle Name	D10 (μm)	D50 (μm)	D90 (μm)
Silica Patch 1	0.414	1.54	10.9
Silica Patch 2	2.91	11.7	24.4
Silica Patch 3	1.73	16.9	56.8
Glass Beads	2.08	19.9	52.1

Table 4.2. The corresponding contact angle of glass slides after the different duration of 0.2 vol% DDMS treatment

0.2 vol% DDMS Treatment Time	Average Contact Angle on Clean Glass Slides	Standard Deviation of Contact Angle
0	8.71	± 1.22
10 s	35.15	± 2.94
30 s	53.96	± 4.36
120 s	72.57	± 6.48
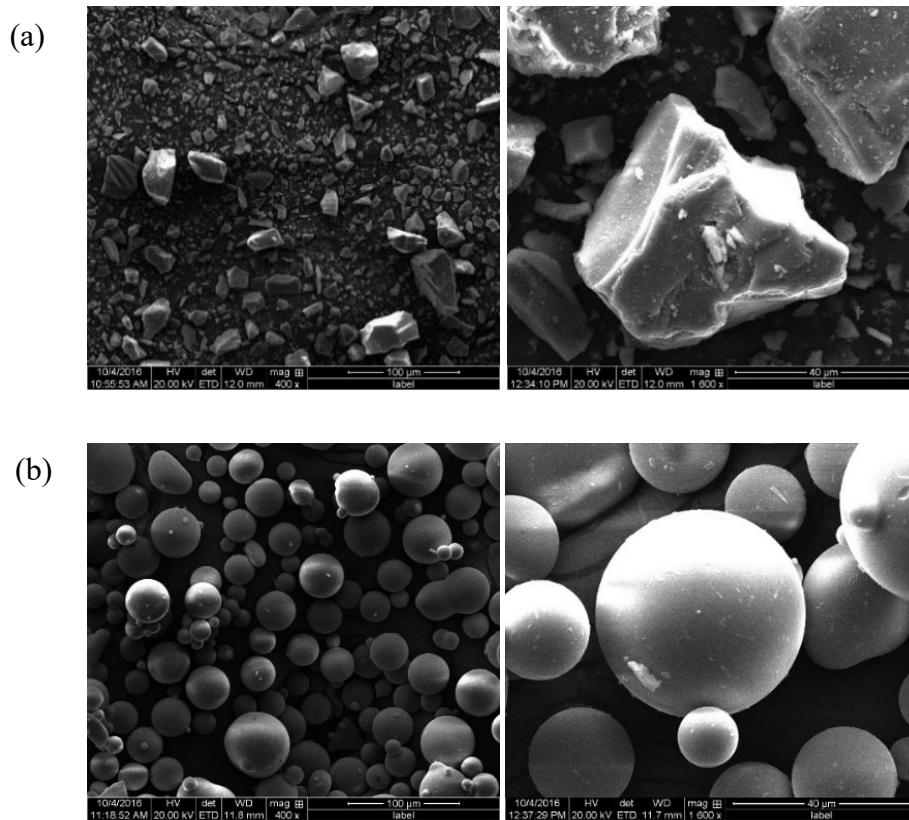
Figure 4.2. SEM images of particles at 400x and 1600x: (a) patch 3 silica particles and (b) glass beads.

4.2.4. Cavitation inception measurement

In this study, the inceptions of hydrodynamic cavitation were measured using an acoustic detection method. A microphone (Fifine-K050) was connected to a computer and taped at the outer wall of the Venturi tube close to the throat. By using Mastersizer 3000, the cavitation generated microbubbles have sizes ranging from 20 to 100 μm with D50 is about 40 μm without particle or chemical addition. The freshly produced microbubbles are smaller than the measured value as they experience coalesce while entering the chamber of Mastersizer. When cavitation occurred, high-frequency energy waves that radiated during bubble oscillation were detected by the microphone [171]. As shown in the insets

of **Figure 4.3**, the absolute amplitudes of the sound signal were extracted in the conditions of no cavitation, intermediate cavitation, and full cavitation. The fluctuation observed in the insets is caused by pulsating flow from the peristaltic pump. The ambient noise was detected below the amplitude threshold of 3 mV, while the noise radiated by the hydrodynamic cavitation exhibited a higher sound level. Cavitation was then distinguished by using a threshold of 3 mV.

For the inception measurement using the acoustic method, half-second of acoustic samples were recorded at 100 kHz at each flow rate. As shown in **Figure 4.3**, the proportion of cavitation samples was plotted against the throat velocity calculated by dividing the flow rate by the Venturi throat area. The fraction of cavitation samples (f) that reach the amplitude threshold are named cavitation probability, and its relationship with throat velocity displays a cumulative normal distribution defined as:

$$f = \frac{1}{2}\left\{1 + \text{erf}\left[\frac{(v - \mu)}{\sigma\sqrt{2}}\right]\right\} \tag{4.1}$$

where erf is the error function, v is the throat velocity, μ and σ are the mean and variance of the distribution. The S-shape cumulative frequency curve can be obtained by fitting the cavitation probability and the associated velocity data into the function above. To quantify the cavitation inception for numerical analysis and comparison, the cavitation inception in this study is defined as the throat velocity where a straight-line fitting the middle section of the S-shape curve intercepts with the x-axis.
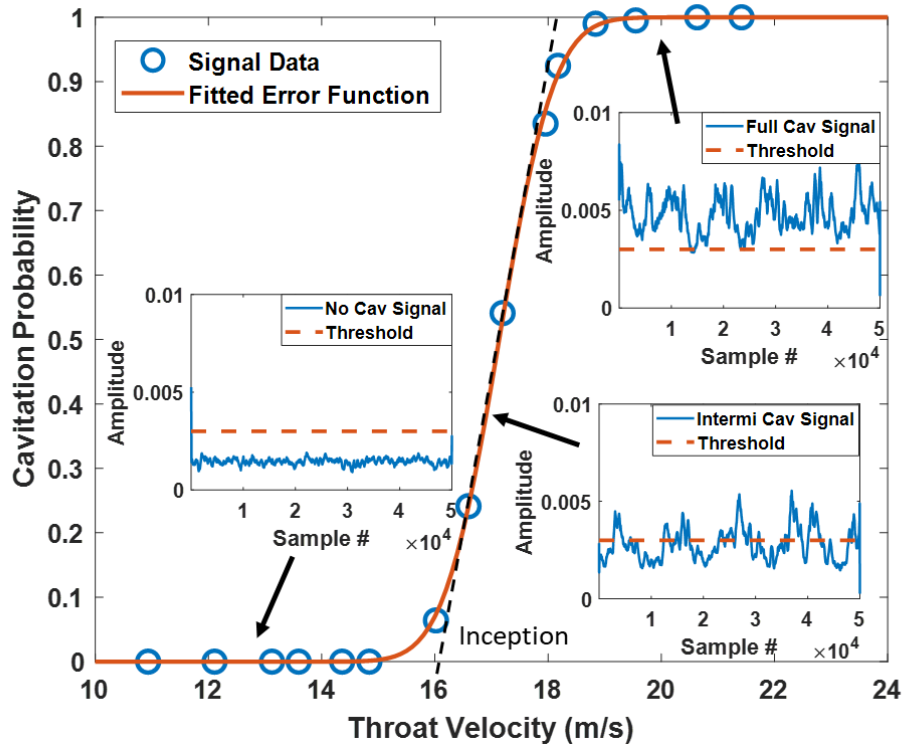
Figure 4.3. Example of cavitation probability test with patch 1 silica particles after 10 s of silane treatment. Inset: The amplitude of the acoustic signal in the conditions of no cavitation, intermediate cavitation, and full cavitation, respectively.

4.3.   Results and discussion

4.3.1. Effect of particles to stabilize nuclei in the water system

Classical theory suggests that gas nuclei in a liquid-air two-phase system are unstable due to their large Laplace pressure. However, stabilized nuclei were observed in particle or dust-rich environments [172]. These nuclei, in return, act as gas nucleation sites and facilitate cavitation. In this section, hydrodynamic cavitation was performed using a glass tube to avoid the nuclei trapped on the tube wall. Without particle addition, the system consists of only de-ionized (DI) water and bulk nuclei were used to simulate two-phase

hydrodynamic cavitation, and the large inception variation of the two-phase cavitation was analyzed. After that, hydrophilic silica particles were introduced, and the role of particles in unifying cavitation inceptions was discussed.

The inceptions of two-phase hydrodynamic cavitation in the glass Venturi tube are shown in **Figure 4.4**. The lines represent the averaged fitted curve of ten tests in each condition. To visually display the reproducibility, each fitted curve was associated with a shaded area, which was obtained based on the standard deviation of the mean of distributions, μ from Eq.4.1, with 99% confidence interval. The results show an interesting phenomenon that for the more than twenty inception tests performed, two distinct groups of results were obtained from the two-phase cavitation despite using the same setup and de-ionized water. The first group on the right has average inception at about 22 m/s. The other group of water samples, by contrast, has much quicker cavitation with average inception at 19 m/s. According to Bernoulli's equation, the pressure in the fluid decreases with the square of fluid velocity. The high cavitation inception indicates a stable water system that is able to withstand low pressure before the liquid ruptures (cavitation). Such water samples were sensitive to the presence of gas pockets, which were detrimental to the high tensile strength of the liquid [133]. In other words, this group of water samples are relatively "nuclei-free". On the other hand, the two-phase cavitation tests with lower inception velocities were "nuclei-present", which were likely induced when replacing the post-cavitation water with fresh DI water for the preparation of the next set of experiments. These nuclei with micron or smaller radii tend to dissolve in bulk water due to the large Laplace pressure unless they are stabilized by either bulk contaminants or tube wall [60],

[173]. The two groups of the two-phase cavitation inceptions could be explained by the unstable existence of nuclei in the water system.
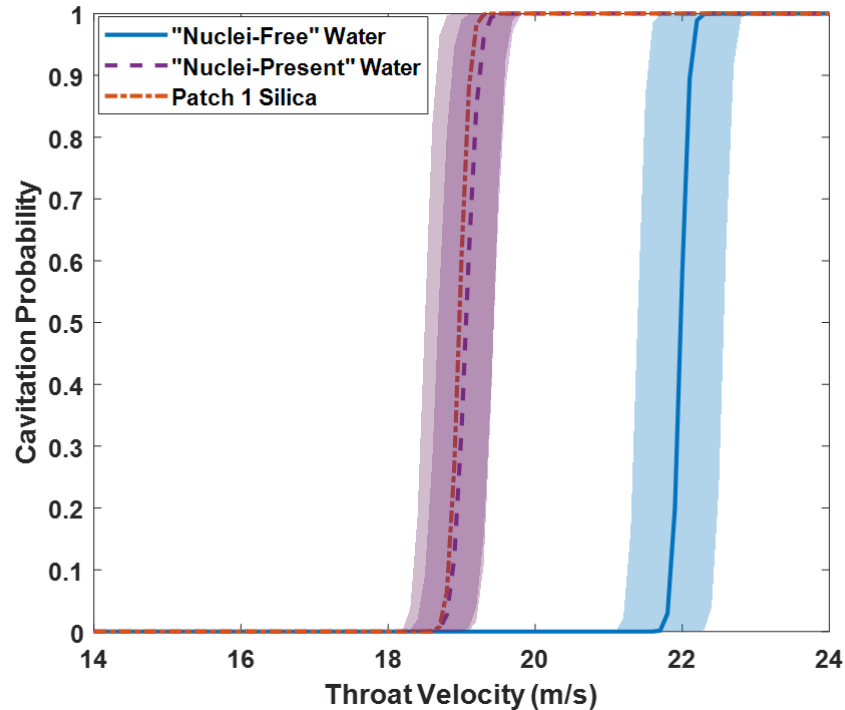
Figure 4.4. Cavitation probability as a function of throat velocity with DI water. Two distinct groups of water results using the same setup and material were observed. The curve of "nuclei-present" water overlaps with the result using untreated silica patch 1.

To confirm the role of naturally hydrophilic particles in stabilizing nuclei and enhance cavitation, silica patch 1 slurry at a concentration of 5 g/L was added to the water system, and the inception curve is shown in **Figure 4.4**. For the ten tests performed with the hydrophilic particles, the results showed great consistency, that the two groups of inceptions obtained from two-phase cavitation were unified to one group at about 19 m/s, which almost overlapped with the "nuclei-present" water data. The patch 1 silica particles, with small D50 at 1.5 μm, and naturally hydrophilic characteristics, were not expected to

bring large nuclei to the water system. Despite that, the particles were able to stabilize the pre-existing nuclei in the system, which reduce the required tensile strength and promote cavitation.

4.3.2. Particle wettability effect on cavitation inception with different types of particles

The wettability of particles plays an important role in hydrodynamic cavitation. Not only because low wettability provides lower energy for heterogeneous nucleation [51], [166], most importantly, it increases the ability of solids to stabilize gas pockets, which drastically lowers the tensile strength of the liquid and induces cavitation at a relatively high pressure. In this section, the silica patch 1, 2, 3 and glass beads of different wettabilities were tested at a concentration of 5 g/L, and the comparison of averaged inceptions of five runs is shown in **Figure 4.5**. The hydrodynamic cavitation was induced by using the glass Venturi tube with a hydrophilic and smooth wall surface. The group of "nuclei-free" DI water tests, representing the two-phase (air and water) hydrodynamic cavitation, were plotted as the reference.

As **Figure 4.5** shows, all four types of bare particles have significant effects in reducing the cavitation inception comparing to the two-phase cavitation due to particles stabilizing nuclei and created nucleation sites for inception. Similar to the two-phase condition, the cavitation probability rose sharply with bare silica addition, which indicates that the cavitation happened violently in just a short period at the corresponding threshold. According to Blake's theory [174], the threshold for bubble nucleation is inversely

proportional to nuclei size. Therefore, the inception profiles of bare particles suggested that the nuclei involved in these cavitation activities were tiny and with relatively uniform sizes.

The inceptions with particles of different wettabilities are compared in **Figure 4.5**. As discussed in section 4.2.4, the inception value in this study is quantified as the throat velocity where the straight line fitting the middle section of the S-shape curve intercepts with the x-axis. It can be clearly observed that with the increase of the particle hydrophobicity, the inceptions show a gradually decreasing trend. This phenomenon is universal for all four types of particles. Taking **Figure 4.5a** as an example, the hydrophobic silica particles lowered the inceptions to 16 m/s, 14 m/s and 13 m/s after silane treatment time t_{DDMS} of 10 s, 30 s and 120 s. Comparing to the inception of the two-phase system which was about 22 m/s, particles after 120 s of treatment caused a significant 9 m/s drop to the inception. Such a drop in inception velocity could be converted to a 158 kPa difference in pressure based on Bernoulli's equation. The low pressure threshold for cavitation results from the presence of large nuclei. With similar ending points at 19 m/s to the bare silica particle curves, particles with hydrophobic coating display earlier inceptions with lower slopes of the cavitation probability curves. These results indicate that, besides the same population of small nuclei which sustain full cavitation, the hydrophobized particles also brought larger nuclei to the water system, which induced partial cavitation at lower throat velocity. Moreover, as the wettability of solid particles decreases, they are able to hold more and larger nuclei.
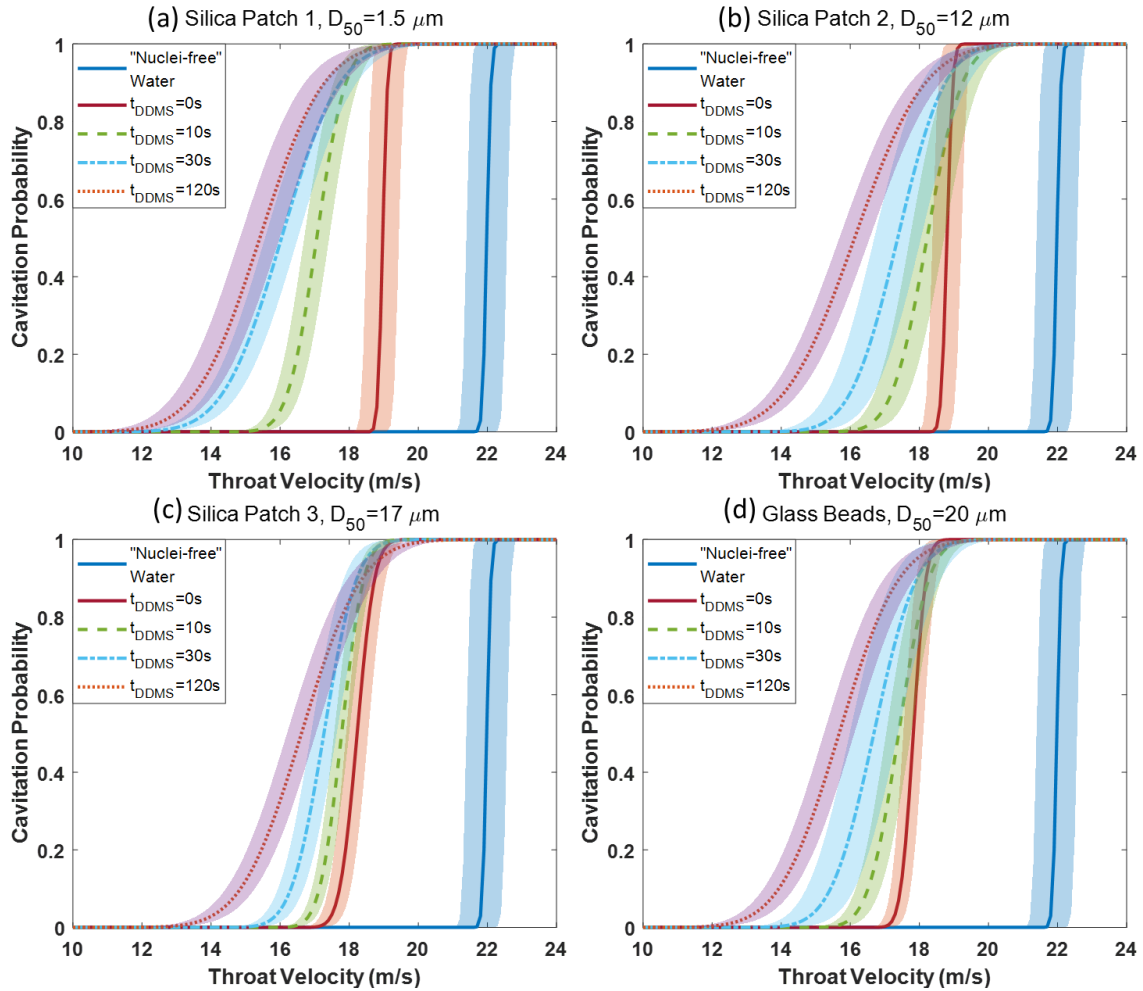
Figure 4.5. Hydrodynamic cavitation inception tests with silica: (a) patch 1, (b) patch 2, (c) patch 3, and (d) glass beads at 5 g/L. Each type of particle was treated in a DDMS solution for different periods (t_{DDMS}) to modify the surface wettability. The average and standard deviation of five tests are plotted for particles with each wettabilities. The result of the "nuclei-free" two-phase hydrodynamic cavitation is plotted as a reference.

Silica particles from patches 1 to 3 have different sizes listed in **Table 4.2**. By comparing **Figure 4.5a** with **4.5b** and **4.5c**, the size effect of particles on hydrodynamic cavitation was demonstrated. The patch 3 particles, with the largest average size, show the lowest inception without silane treatment. This result was confirmed by Marshall et al. in

2003 that larger particles have a better effect in reducing the tensile strength of water, possibly due to the ability to hold larger nuclei [58]. However, this effect is no longer obvious for hydrophobic particles. Hydrophobic fine particles exhibited smaller inceptions as particle size increased. This result might arise from the complex fine particle agglomeration process where micro-size bubbles can be stabilized inside a particle-bubble cluster [46], [49], [112]. The results show that in the tested size range, wettability plays a critical role in reducing cavitation inception regardless of the particle size. However, this cavitation selectivity is more pronounced for fine particles.

Glass beads with similar particle size distributions as silica patch 3 were applied to examine the effect of particle surface roughness on cavitation inception (**Figure 4.5d**). Similar to **Figure 4.5c**, the ability of hydrophobized glass beads in lowering the inception of the fluid system is as good as the silica particles. This result is contrary to the expectation that the smooth surface of glass beads was supposed to have a limited ability to facilitate nuclei. Nuclei that exist in the crevices on the particle surfaces are restricted by the size of the crevices [57], [175], thus the nuclei are expected to be tiny considering the fine sizes of particles used in this study. Moreover, as shown in **Figure 4.6**, the phenomenon of "air-ball" like clusters was observed when hydrophobic particles were added to the water system, which evidenced the presence of large air bubbles agglomerated with hydrophobic particles. According to the bubble nucleation theory, the inception is initiated by the nucleation of the largest nuclei in the system. The results demonstrated that hydrodynamic cavitation with particles is possibly induced by the bubbles attached to particles, whereas the tiny nuclei entrapped in surface crevices play an insignificant role in this case. Therefore, the effect of particles on cavitation is barely affected by surface roughness.
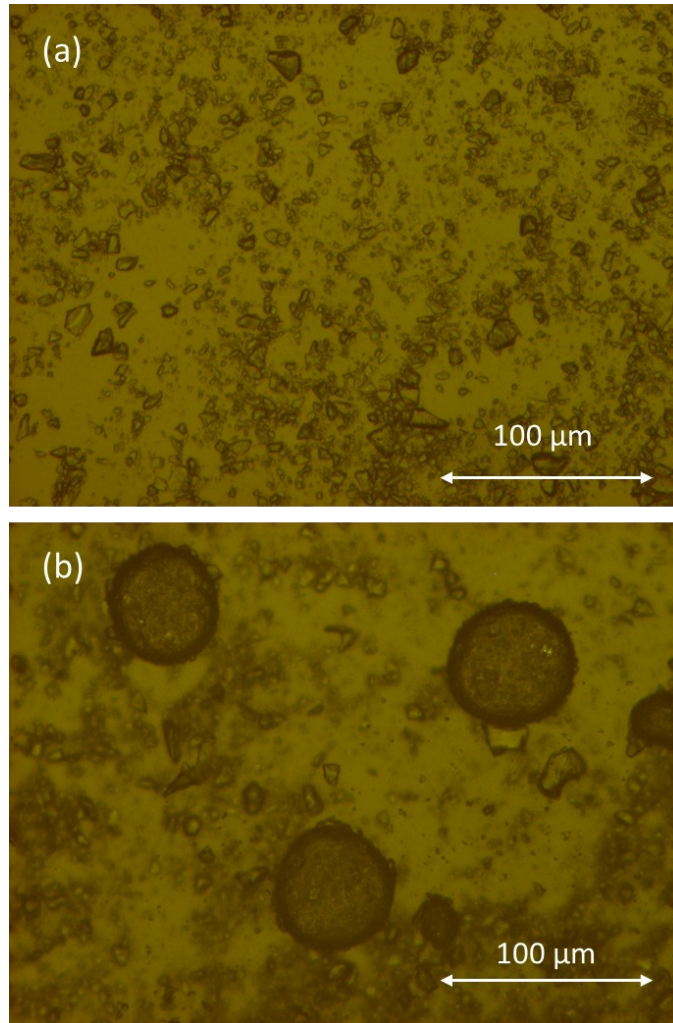
Figure 4.6. Microscopic images of slurry using patch 2 silica particles (a) without and (b) with 30 s of DDMS treatment. Air balls were observed with surface hydrophobic particles.

4.3.3. Role of gas-pockets in the effect of wettability in hydrodynamic cavitation

Besides the formation of particle-covered air bubbles during particle addition, another possible mechanism for the hydrophobic particles to bring bubbles into the water system is that when silane-treated particles were added to water, they would sink before being fully wetted and carry gas pockets on their surfaces [172]. Both theories suggested the

introduction of gas pockets during hydrophobic particle addition. Therefore, the reduction of cavitation inception by hydrophobic particles was believed to be the effect of surface gas pockets. However, hydrophobic solid surfaces themselves could promote cavitation since the free energy required for bubble nucleation is lowered with higher hydrophobicity [51]. To investigate the significance of gas pockets in the effect of particle wettability, particle slurries after gas-pocket elimination were tested. The correlation between cavitation inceptions and particle wettabilities was compared with that of undegassed slurries.

To remove the gas pockets in the water system, the silica patch 2 slurries were degassed by vacuuming in a sealed flask for ten minutes. The samples were then placed in the open air for four days to recover the air-saturation level so that the inceptions could be examined without the effect of gas-saturation level [150]. With the equilibrium contact angle of tested particles less than 90°, the degassed particles would not be able to spontaneously re-generate surface nuclei, even in the crevices [176]. In **Figure 4.7**, throat velocity at inception was plotted as a function of the particle hydrophobicity, which is represented by the contact angle of glass slides under the same silane treatment. Curves fitted the average inceptions were plotted to guide their trend over hydrophobicity. Regardless of the presence of gas pockets, the addition of bare silica particles (9°) has similar inceptions at approximately 18 m/s. The inception differences were observed between undegassed and pre-degassed slurries when the silane-treated silica particles were applied. For silica in undegassed water, the inceptions decreased considerably with hydrophobicity. In comparison, the pre-degassed slurries showed relatively consistent inceptions at around 18 m/s, which barely changed from the untreated silica. These phenomena indicate that the

gas pockets are the main trigger to promote cavitation, and larger gas pockets are carried by particles with higher hydrophobicity. A noticeable drop in inception could be observed for particles of 73°. However, the average inceptions (17 m/s) are still about 20% higher than the inception tested in undegassed water. Considering the effect from surface energy not as critical as gas pockets for cavitation inception, this drop in inceptions is possibly caused by the hydrophobic particle-stabilized gas pockets which survived from the nuclei elimination process.
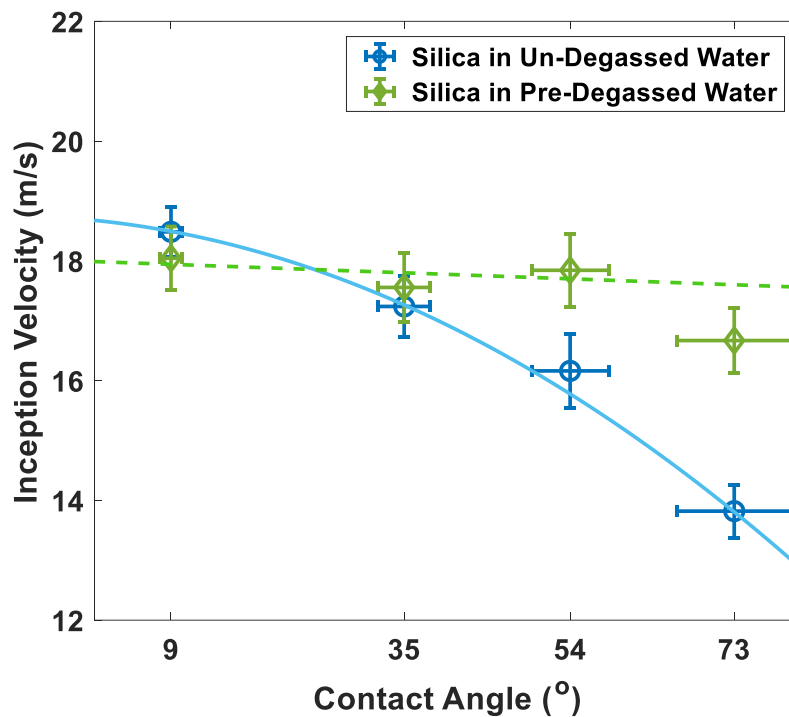
Figure 4.7. Hydrodynamic cavitation inceptions with particles of different wettabilities. Cavitation tests were performed using silica patch 2 in pre-degassed water to eliminate the gas pockets in the water system. The results are compared with tests using un-degassed slurries.

4.3.4. Effect of Venturi tube wall wettability on three-phase cavitation

In previous sections, the hydrodynamic cavitation was performed in a glass-made Venturi tube whose wall is smooth and hydrophilic. Without interference from the tube wall, hydrodynamic cavitation tests show that the wettability of solids plays an important role in changing the inception of three-phase hydrodynamic cavitation. Considering the direct interaction between the wall and liquid flow, it is reasonable to expect that the surface properties of the Venturi tube wall would also affect the hydrodynamic cavitation process. In this section, silica patch 2 slurries with different wettabilities were tested in the 3D-printed Venturi tube. The results were compared with the glass tube.

In **Figure 4.8**, cavitation inceptions of particle slurries are plotted as a function of particle wettability, and the effect of glass Venturi tube and 3D-printed Venturi tube were compared. Tests performed in two-phase systems were included as the reference group. For tests performed in the glass tube, the addition of silane-treated silica decreases the inceptions considerably. The curve fitting average inceptions display a downward trend from approximately 20 m/s in two-phase cavitation tests to 14 m/s in tests with the most hydrophobic silica particles (73°). By contrast, the cavitation test using the 3D-printed tube showed much lower inception in two-phase cavitation, where cavitation started as early as 15 m/s throat velocity. As shown in **Figure 4.1b**, the 3D-printed Venturi tube was intentionally designed to have similar geometry as the glass Venturi tube. The geometry differences between these two Venturi tubes are within 100 micrometer range. Such a tiny difference could not solely explain the significant inception difference in two-phase cavitation tests (almost 5 m/s) without the effect from the hydrophobic characteristic of the 3D-printed tube wall. When bare silica particles (9°) and 10 s-silane treated particles (35°)

were added, the inceptions barely changed since their contact angle is much lower than the contact angle of 3D-printed material at 55°. The nuclei induced by those particles were not as large as the hydrophobic tube wall, having no apparent effect on cavitation inceptions. The further addition of the 30 s and 120 s treated particles (54° and 73°) in 3D-printed tube lowered the inceptions, the overall decrease was from about 15 m/s to about 13 m/s. The effect of hydrophobic particles in lowering inception velocity was far less effective than using the glass tube.
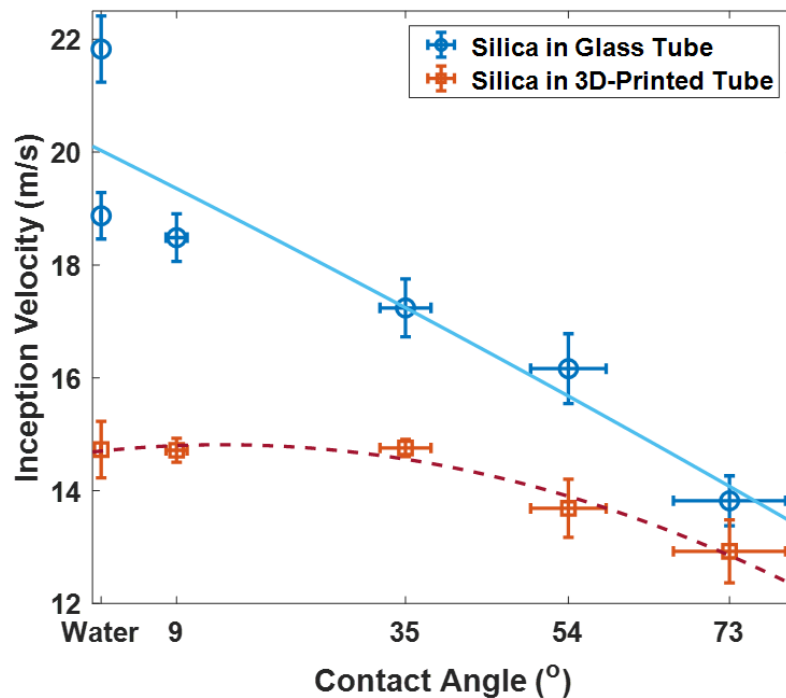
Figure 4.8. Hydrodynamic cavitation inceptions with patch 2 silica with different wettabilities. Tests were performed using a glass Venturi tube and a 3D-printed Venturi tube.

4.4. Conclusion

The effect of particle properties on hydrodynamic cavitation behavior was investigated using the acoustic detection setup. Two distinct average inceptions, 18.9 and 21.8 m/s, were found in the two-phase cavitation tests using a glass Venturi tube. The addition of naturally hydrophilic fine particles converged the inceptions to 18.5 m/s, which is possibly due to the particles stabilizing gas nuclei in bulk water. Particles with different wettabilities, sizes and roughness were also tested in the three-phase hydrodynamic cavitation. Regardless of the surface roughnesses and particle sizes, particles with lower wettabilities could effectively reduce cavitation inception. Based on the relative constant inceptions from three-phase cavitation tests using pre-degassed slurries, the mechanism of particle wettability effect was demonstrated to be the introduction of gas pockets. Compared to the glass Venturi tube, the 3D-printed Venturi tube had a more hydrophobic tube wall which significantly promoted hydrodynamic cavitation. Under such circumstances, the wettability effect from particles on hydrodynamic cavitation became less obvious.

In the industrial flotation process, both recovery and grade are critical parameters that need optimization. Hydrodynamic cavitation, as an efficient micro-bubble generation process, was proven to improve the recovery of fine particles. However, questions have been raised that the tiny bubbles could entrap unwanted particles, causing a lower grade of froth. Based on this study, it is encouraging to see that hydrodynamic cavitation has the potential to improve the flotation selectivity, taking advantage of particle hydrophobicity in promoting cavitation. By using a hydrophilic Venturi tube where the performance of hydrophobic and hydrophilic particles can be differentiated, the operation flow velocity

could be adjusted to reach the inception of only target particles. By doing so, it is promising to have bubble nucleation from cavitation happening on target particles only; thus both recovery rate and selectivity are improved.

Chapter 5 Enhancement of Selective Fine Particle Flotation by Microbubbles Generated through Hydrodynamic Cavitation

Abstract

The flotation of fine particles less than 50 µm is challenging for the mining industry. By using hydrodynamic cavitation, a significant improvement in the recovery of fine particles has been found. This study aims to investigate the effect of hydrodynamic cavitation on the selective flotation of fine particles from detailed mechanisms. Our single-bubble flotation results indicated that the bubble-particle collection efficiencies of fine silica particles (D_{50} = 6 µm and D_{50} = 16 µm) improved after hydrodynamic cavitation, especially for hydrophobized silica particles. The improved flotation performance of fine particles was investigated from three perspectives: (1) By zeta potential distribution measurements, bubble-frosting on hydrophobic particles was demonstrated after hydrodynamic cavitation. (2) The formation of large aggregates of hydrophobic fine particles after cavitation was revealed by slurry turbidity and particle size measurements, potentially contributing to the improved collision efficiency of the fine particles due to the bridging effect provided by microbubbles. (3) The attachment efficiency between a solid surface and flotation bubbles was enhanced if the surface was covered with hydrodynamic cavitation-generated microbubbles. Compared to the hydrophilic particles, the hydrophobic particles benefited from the hydrodynamic cavitation from the perspectives of bubble frosting, particle-bubble collision efficiency and attachment efficiency. Based on this study, it is expected that the separation efficiency for fine hydrophilic and hydrophobic particles can be improved by hydrodynamic cavitation.

5.1. Introduction

Froth flotation, which was first applied in the mining industry in the nineteenth century, is now widely used in mineral processing [23], [25], oil sands processing [18], [19], [177], [178], paper recycling and wastewater treatment [21], [179], [180]. With the depletion of high-grade and easy to process ores, miners are facing low-grade and complex ore bodies. In this case, fine grinding circuits have to be applied in order to liberate the valuable minerals, resulting in a substantial amount of fine particles. It has been reported that the flotation recovery is highly dependent on the particle size. Particles under 10-20 μm, even with desired hydrophobicity, are difficult to recover by flotation except by entrainment [35], [181]–[183]. This phenomenon is believed to result from the low efficiency of particle-bubble interactions [26], [27], [29], [184]–[186].

It is generally accepted that the interactions between particle and bubble include three sub-processes: collision, attachment, and detachment [26], [27]. Surface forces such as the Van der Waals, electrostatic and hydrophobic, are important to the particle-bubble interaction, particularly the attachment efficiency [27], [187], [188]. For fine particles, the detachment is negligibly small because of the low inertia [28], [29]. Their small sizes mainly contribute to the low collision efficiency between them and conventional flotation bubbles. Two major approaches have been investigated to improve fine particle flotation, including decreasing the bubble size and increasing apparent particle sizes [36]. In particular, the methods of enhancing particle sizes by forming flocs or aggregates are of great interest. Typically, a long-chain polymer or coagulant is added to promote the aggregation of fine particles [37], [38]. However, this method had challenges in the industry due to the lack of selectivity of the reagents used, resulting in the entrapment of

gangue minerals [39], [40]. Thus, the demand for an efficient method to selectively improve the collision and attachment of conventional flotation bubbles and fine particles is still substantial.

In recent years, hydrodynamic cavitation (HC) emerged as a promising method for improving the flotation recovery of fine and ultrafine particles [3], [16], [189]. Cavitation is a process whereby gas/vapour filled voids are formed [1]–[3]. With a fast liquid flow through a specialized geometry, such as orifice and Venturi tube that allows velocity variation, hydrodynamic cavitation occurs, and bubbles nucleate by utilizing the decrease and subsequent increase in local pressure [190]. It has been reported that micro/nanobubbles generated by hydrodynamic cavitation can help the aggregation formation and increase the surface hydrophobicity of fine and coarse particles (coal, phosphate), thus improving flotation recovery and flotation rate [6], [41], [44], [143]. Besides that, the advantages of micro/nanobubbles can extend to lower consumption of collector and frother [43], [44], [191].

Previous studies have mainly focused on the effect of HC on the overall recovery of target particles. However, the detailed mechanism in flotation sub-processes and the effect on flotation selectivity were usually neglected. The goal of this paper is to investigate the effect of hydrodynamic cavitation on the flotation of both hydrophilic and hydrophobic fine particles. The collection efficiency representing the overall floatability of particles before and after HC was experimentally quantified. To explain the results, the effects of HC on particles with different wettabilities were further investigated from the perspective of bubble frosting, aggregation formation and solid-bubble attachment. In the end, the

mechanisms of HC on the selective improvement of hydrophobic particle flotation were discussed and summarized.

5.2.   Experimental Methods

5.2.1. Hydrodynamic cavitation devices and operating parameters

The hydrodynamic cavitation (HC) based bubble generation setup is shown in **Fig. 5.1A.** The setup with auto-gas suction was designed to continuously provide microbubbles for the study of particle performance in the flotation process. Connected by the 5/16 inches (7.94 mm) Tygon tubes, the peristaltic pump drove the water from a storage tank at atmospheric pressure into the Venturi-type gas suction tube. This tube was designed with a tube inlet/outlet diameter at 6.67 mm and a slight narrow throat diameter of 5 mm, which created a zone lower than the atmospheric pressure at the Venturi throat when water passed through. The air was automatically injected into the system, by which the air flow rate was controlled at 14.3 CCM by the valve. At downstream of the peristaltic pump, the water-air mixture entered a pressurized cell and separated into two phases. Choked by the Venturi type HC device with a large inlet/throat diameter ratio at 4, high pressure built up in the pressurized cell, causing the dissolution of excessive air into water according to Henry's law [74]. The air-saturated water was discharged from the cell bottom to avoid the escape of large bubbles. In the downstream, the Venturi-type HC device was designed with a high inlet angle at 42° and a low outlet angle at 6° so that the occurrence of HC was greatly promoted [147], [192]. The liquid passing through the Venturi throat experienced a sudden static pressure drop and became air-supersaturated, and subsequently microbubbles nucleated at the tube outlet. In this study, the HC bubble generation process was conducted

using DI water in a controlled environment at 20°C, with a constant water flow rate at 1.34 L/min (approximately 25 m/s at Venturi throat) and no chemical additives. One minute of HC setup operation would generate sufficient microbubbles to turn the clear DI water into milky bubble solution, as shown in **Fig. 5.1B**. An on-site bubble size measurement using Malvern Mastersizer 3000 provided the microbubble size distribution in **Fig. 5.1C**, with a mean bubble size of about 38.3 μm. The actual bubble sizes could be much smaller than the measured value since tiny bubbles passing through the Mastersizer suction tube would coalesce or dissolve without stabilizing by any surfactant.
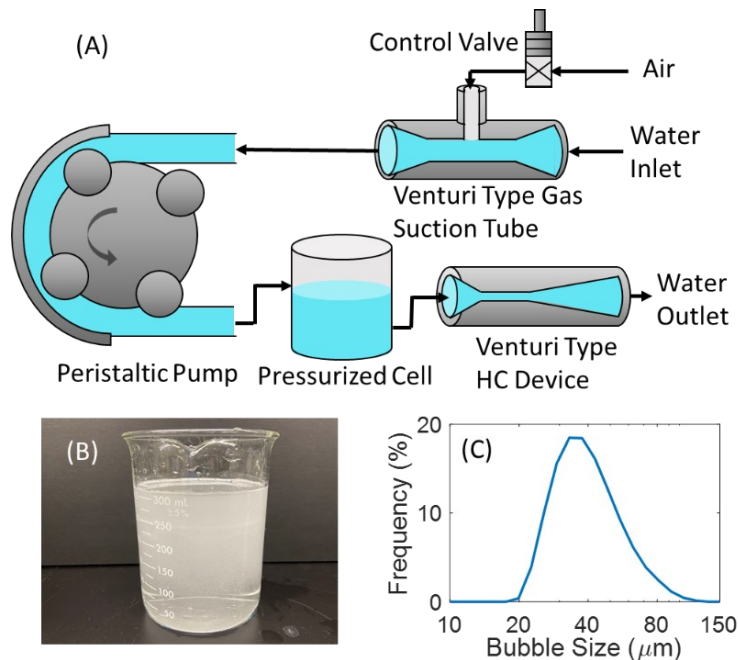
Figure 5.1. (A) Hydrodynamic cavitation-based bubble generation device with auto gas-suction design. (B) Picture of DI water after one minute of bubble generation process with operating parameters used in this study. (C) Size distribution of the HC generated microbubble measured using Malvern Mastersizer 3000. No surfactant was added in this operation.

5.2.2. Single bubble-particle collection efficiency measurement and calculation

In this study, the overall efficiency of bubble-particle interaction was quantified by measuring the collection efficiency. This study used two batches of high purity silica particles purchased from U. S. Silica (MIN-U-SIL®) with mass median diameters (D_{50}) at around 6 µm and 16 µm. The contact angle of original silica particles was assumed to be 10° by measuring the contact angle of a clean glass of similar material. Two batches of silica particles were hydrophobized to various degrees by exposure to 0.1% dichlorodimethylsilane (99.5%, Sigma-Aldrich) in toluene for 0.5 and 2 min, and the contact angles of the silica particles were approximated by the contact angles of glass surfaces with the exact same treatment, which were 45°-50° and 75°-80°, respectively.

The two batches of silica fine particles, each with three different wettabilities, were used in the single bubble flotation experiment before and after HC treatment. For each test, 1 g of silica particles were mixed in 1 L of DI water using a mechanical agitator kept at 300 rpm for 5 min to form the 0.1 wt% silica suspension. Such dilute suspension was prepared to minimize the entrainment amount in the collection efficiency measurement. For experiments that required the HC treatment, the suspension was recirculated through the HC setup for 1 min, then immediately transferred to the single bubble flotation set up for collection efficiency tests.

A modified Hallimond flotation setup with a three-way valve for the single bubble-particle collection efficiency experiments is shown in **Fig. 5.2**. In order to minimize unwanted turbulence and create a particle-free water zone before introducing the single

bubbles, a three-way valve designed by Dai et al. was used in this study [193]. During feeding, the three-way valve was positioned towards the bottom, where the top and bottom sections were separated as shown in the top inset of **Fig. 5.2**. Fresh Milli-Q water was introduced into the top tube from the water injection site, while the silica suspension was transferred to the tube bottom from the slurry injection site. During the experiment, the three-way valve was positioned to the right, as shown in the bottom inset, so that the top and bottom tubes were connected. Capillary generated single bubbles (about 2.2 mm on average) with an inner diameter of 0.15 μm were injected from the tube bottom for a total of one minute at about one bubble per second; the total number of bubbles was around 60-70 for each test. The particles were collected from the particle collecting chamber and then counted by microscope visualization.
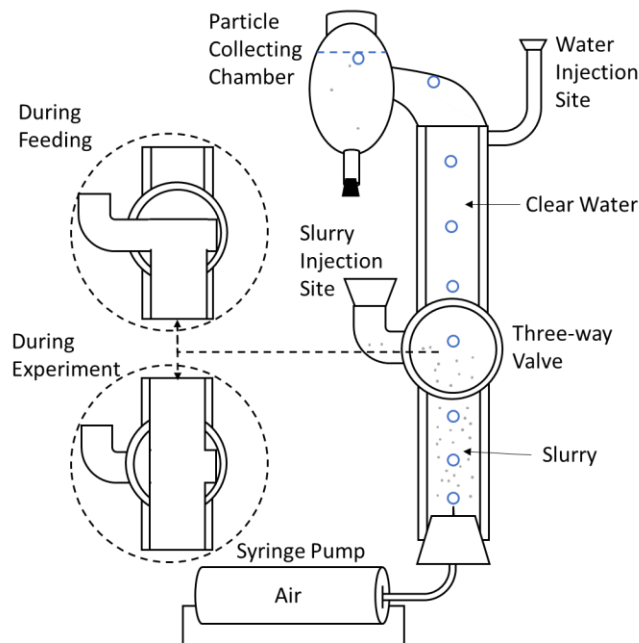
Figure 5.2. Single bubble flotation test setup for collection efficiency measurement. A three-way valve was placed in the middle to separate clear water at the top tube from particle suspension at the bottom before the experiment.

The calculation of collection efficiency follows the work of Dai et al. [194], where the experimental collection efficiency E_{col}^{exp} is estimated as a function of the number of particles collected per bubble; in order words,

$$E_{col}^{exp} = \frac{N_{pf}}{C_p \times V_f} = E_c E_a E_s \tag{5.1}$$

where N_{pf} represents the number of particles floated per bubble, C_p is the particle number concentration and V_f is the volume of the suspension in the path of the rising bubble. The collection efficiency can be defined as the product of the efficiency of three sub-processes in flotation, which involves collision efficiency, E_c, attachment efficiency, E_a, and stability efficiency, E_s [195].

The collection efficiency provides an overall concept of the ability of a type of particle to be picked up by flotation bubbles. It is also regarded as the combination of efficiencies for the flotation sub-processes. To explain the selective effect of HC on particles of different wettabilities, the fundamentals of HC on particle collision and attachment were further studied. The stability efficiency of particle-bubble masses was neglected in this study, as small sizes and low masses of particles were associated with negligible detachment probability [28], [29].

5.2.3. Bubble frosting tests by Zetaphoremeter

The zeta-potential distribution analysis using Zetaphoremeter (SEPHY-CAD Instrumentations) is an innovative method to identify the interaction potential of different substances in dynamic environments [196], [197]. It measures the electrophoretic mobility distribution of materials by tracking their trajectory in an applied electric field, and the

electrophoretic mobilities are converted to zeta potential using the Smoluchowski equation [198]. In this study, the zeta potential distribution of air bubbles generated using the HC set up and particle suspension of 6 μm silica at 10° and 45° were measured individually. Without surfactant addition, the zeta-potential distribution of silica particles and air bubbles show similar results that are difficult to distinguish [199]. To solve this issue and to stabilize bubbles for measurements, the cation surfactant dodecylamine hydrochloride (DAH) at 0.1 mM was added to each sample to bring the zeta-potential of bubbles to a relatively positive value. For the experiments of HC bubble frosting on particles, silica suspensions of different wettabilities were mixed with HC bubbles using two methods: (1) The suspension was mixed with HC-generated bubbles using a stirrer; (2) The suspension of particles was directly recirculated in the HC bubble generation setup, then, analyzing their zeta potential distribution. The level of bubble frosting at each condition could be analyzed by comparing the zeta-potential distributions of the mixtures with pure particles or bubbles. All measurements were carried out in 10 mM NaCl solution at natural pH of around 6.5.

5.2.4. Particle aggregation tests by measuring slurry turbidity and particle size distribution

Previous research has demonstrated that the particle-bubble collision efficiency is proportional to the square power of particle sizes [31], [200], [201]. In fine particle flotation, the low collision efficiency due to small particles sizes is a critical issue that needs to be addressed. Previous studies on the HC have visually shown the images of particle aggregates bridged by microbubbles [6], [46], [49]. In this study, the selective effect of HC

bubbles on aggregation formation was demonstrated using turbidity tests. Silica particles (6 µm) with CA = 10°, 45°, and 75° were used to prepare 1 wt% slurry. The slurry samples at agitation before and after 1 min of HC treatment were immediately transferred to a 100 mL glass cell equipped in Micro 100 Turbidimeter (Scientific, Inc.). This equipment automatically measured the turbidity of the slurry sample in real-time so the relationship between turbidity change over time could be obtained. The formation of aggregates could reduce the number of suspending particles, thus resulting in a turbidity decrease in the slurry. The slurry samples were then taken to measure the particle size distribution using the Malvern Mastersizer 3000, so that the results from turbidity tests could be verified. To avoid interference from bubbles in the particle size measurement, each sample was size-measured at least 5 mins after HC treatment, so that the free microbubbles in bulk water would either dissolve or escape from the solution.

5.2.5. Bubble-solid attachment experiment

In the bubble-solid attachment efficiency study, flotation size bubbles were generated one by one to interact with inclined glass pieces in DI water. This method has been used to measure the induction time of bubbles and solid surfaces [202]. As explained in **Fig. 5.3**, bubbles generated from a capillary tip would rise, contact, slide, and potentially attach to the top glass tilted 30°. Three glasses of different surface properties were prepared: A UV-treated clean glass surface with CA = 10°, a hydrophobized glass surface with CA = 45°, and a microbubble-covered glass surface prepared by placing a bare glass into HC generated bubble solution. By image analysis, the sizes of rising bubbles in this section were measured at about 0.9 mm. The controlled small size could avoid bubble deformation according to Weber number, *We*:

$$We = \frac{\rho_l v_b^2 d_e}{\sigma} \tag{5.2}$$

where ρ_l and σ are the density and surface tension of DI water, respectively. With the bubble volume equivalent diameter, $d_e \sim 0.9$ mm, the bubbles had rising terminal velocity, v_b of about 0.1 m/s [203], [204]. Such flotation bubbles had a Weber number around 0.13, which is less than one. Therefore, the bubbles would undergo negligible deformation and a relatively consistent rising path [205]–[207]. After contacting the glass surfaces, the bubbles were not necessarily attached but thinning the interfacial water film while sliding on the glass surface due to the buoyancy force. Using a high-speed camera, the motion of the bubbles approaching and sliding underneath the glass surface was captured, and the period from bubble-solid contact to attachment was recorded as the induction time.
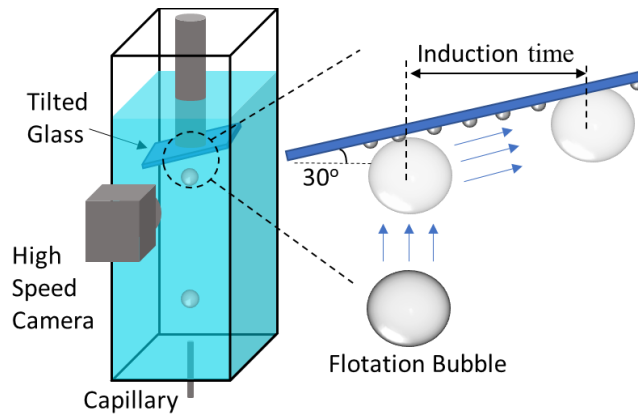
Figure 5.3. Schematic diagram of the bubble sliding experimental setup and graphic demonstration of parameters.

5.3.   Results and discussion

5.3.1. Single bubble-particle collection efficiency

The collection efficiency represents the overall ability of a single bubble to pick up particles and is a comprehensive parameter that involves the collision, attachment and detachment efficiencies. By comparing the collection efficiency before and after HC treatment, the overall effect of HC on the flotation of particles of different wettabilities was obtained, providing a direction for further analysis of the HC effect on sub-processes.

As shown in **Fig. 5.4**, using 6 μm and 16 μm particles, increased collection efficiencies of silica particles were observed as a function of particle size and hydrophobicity before HC treatment. These results were expected since larger particles were easier to collide with flotation bubbles, and their larger mass provides higher momentum that helps penetrate through the bubble-particle interfacial water film. With stronger hydrophobic forces for attachment, the particles with lower wettability were the most favourable for flotation at both sizes. The hydrophilic ones were difficult to pick up. In fact, the collected hydrophilic (10°) silica particles before cavitation could be largely contributed by entrainment, as the attachment and collision efficiency for fine hydrophilic particles should be quite small.

Compared with those before cavitation, the particles after HC treatment had obvious higher collection efficiency. Interestingly, the collection efficiency of bare silica after HC treatment slightly increased from $0.87x10^{-3}$ to $2.29x10^{-3}$ for 6 μm silica and from $4.17x10^{-3}$ to $6.88x10^{-3}$ for 16 μm silica. The result suggests that the HC-generated microbubbles could improve the recovery of hydrophilic particles to a small extent. On the other hand, the improvement in collection efficiency became substantial for the hydrophobic particles

(contact angle at 45° or 75°), where the efficiency values after HC were more than doubled. Based on the flotation sub-processes, the increase in collection efficiency could be attributed to higher collision and attachment efficiencies. The possible mechanism is the HC bubbles frosting on the hydrophobic particles, which improved their interactions with other particles and large flotation bubbles. The bubble-frosted particles formed particle aggregates to improve the collision probability with flotation bubbles, and the attachment efficiency was also improved due to bubble coalescent attachment. To demonstrate this hypothesis, specific studies on the effect of HC on flotation sub-processes will be included in the next sections.
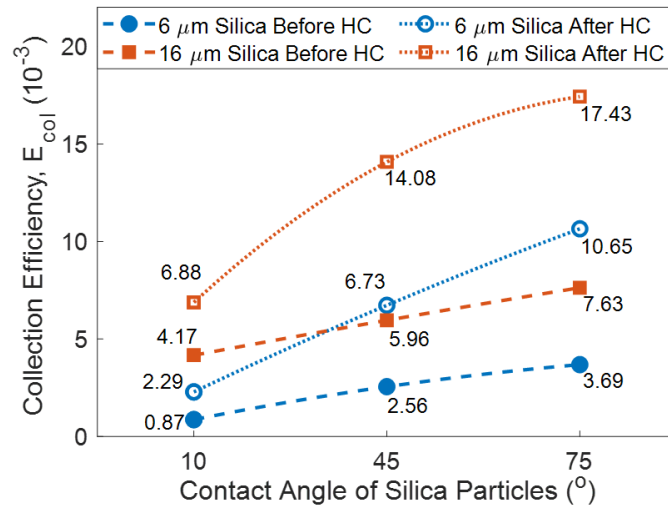
Figure 5.4. Collision efficiency of hydrophilic silica (10°) and modified hydrophobic silica (45° and 75°) using 6 μm and 16 μm silica particles before and after HC treatment.

5.3.2. Effect of HC on bubble frosting on particles of different wettabilities

The microbubbles frosting on particles after the HC treatment is the first, yet most critical step in the HC-assisted fine particle flotation. It is the precondition for microbubble-aided particle aggregation and particle-flotation bubble attachment. In this study, the interaction between HC bubbles and particles of different wettabilities was demonstrated by zeta-potential distribution measured using the Zetaphoremeter. DI water with 0.1 mM DAH was used to generate a relatively positive zeta potential for bubbles, while the silica particles have negative potential values at the operating pH of 6.45. Having the two materials with different peaks, a merging distribution would represent the combination of particles and bubbles, and more positive values would suggest well-frosted bubbles on particle surfaces.

The zeta-potential distribution of HC bubbles, silica particles, bubble-particle stirring mixture, and particle suspension after HC mixing are shown in Fig. 5.5 from top to bottom. The results were presented with hydrophilic particles (10o) on the left and hydrophobic particles (45°) on the right. Each sub-figure is the combination of 5 test runs for reproducibility, and the x-axis of all figures was kept the same for comparison. The mean value of each peak was indicated using dash lines. The bubbles affected by the cation surfactant DAH have a relatively positive distributions average value of 11.2 mV. On the other hand, the particles displayed negative values, where the hydrophilic silica particles had a peak at -53.1 mV, and hydrophobic particles had a less negative peak at -29.1 mV. The shift of hydrophobic particles demonstrated the presence of gas pockets on the particle

surfaces, which were formed due to particle wettability and roughness [57], [208], [209]. The measurement of hydrophobic particles in a pre-degassed solution had similar zeta-potential results to hydrophilic particles; thus, the mild hydrophobic coating (45°) from silane treatment had no significant effect on the particle zeta-potential without the presence of surface gas pockets.

As shown in the third row of **Fig. 5.5**, two peaks were observed for both the hydrophilic and hydrophobic particles by mixing the HC-generated microbubbles with the particles. For hydrophilic particles, the left peak with an average of -40.6 mV represented the particles that barely interacted with bubbles, and the right peak at -5.9 mV could result from the partially covered particles with HC bubbles. Due to buoyancy force and large Laplace pressure, the microbubbles were difficult to stabilize for measurements, thus resulting in a much lower number frequency of the right peak than the particle peak at the left. The two peaks of the mixture indicate a bad attachment of bubbles and hydrophilic particles. In fact, the attachment in the right peak might be due to the attractive EDL forces, which would be negligible if non-cation surfactants were used. Compared to the hydrophilic particle-bubble mixture, bubbles played a more significant role with hydrophobic particles even though two peaks were observed. Simply mixing bubbles and 45o particles, the left point that represented particles shifted from -29.1 mV to -9 mV, trending toward the bubbles. The right peaks with relatively higher frequency were at 12.3 mV, close to the original bubble value, indicating a complete covering of bubbles on particle surfaces. The result indicated a higher level of hydrophobic particle-bubble interactions and the presence of more stabilized bubbles.

The last row of **Fig. 5.5** shows the zeta potentials of particle suspensions after 2 mins of HC treatment. In these processes, particle suspensions participated directly in the bubble generation process, where bubbles could directly nucleate on the particles from pre-existing surface gas pockets. As a result, the level of bubble-particle attachment was expected to be higher than that of particle-HC bubble post-mixing. However, the results of hydrophilic particles showed no obvious difference. Two obvious peaks were still present with mean values slightly trending toward bubbles, demonstrating the low efficiency of bubble frosting on hydrophilic particles even with HC treatment. On the other hand, the hydrophobic particle suspension showed a unique peak at 12 mV after HC treatment, similar to the value of bubbles. This phenomenon indicated a strong bubble-particle attachment and bubble covering on particles on a large scale. Overall, the HC micro bubble frosting is obvious with hydrophobic particles, and the best way to achieve bubble-particle attachment is through direct HC treatment.
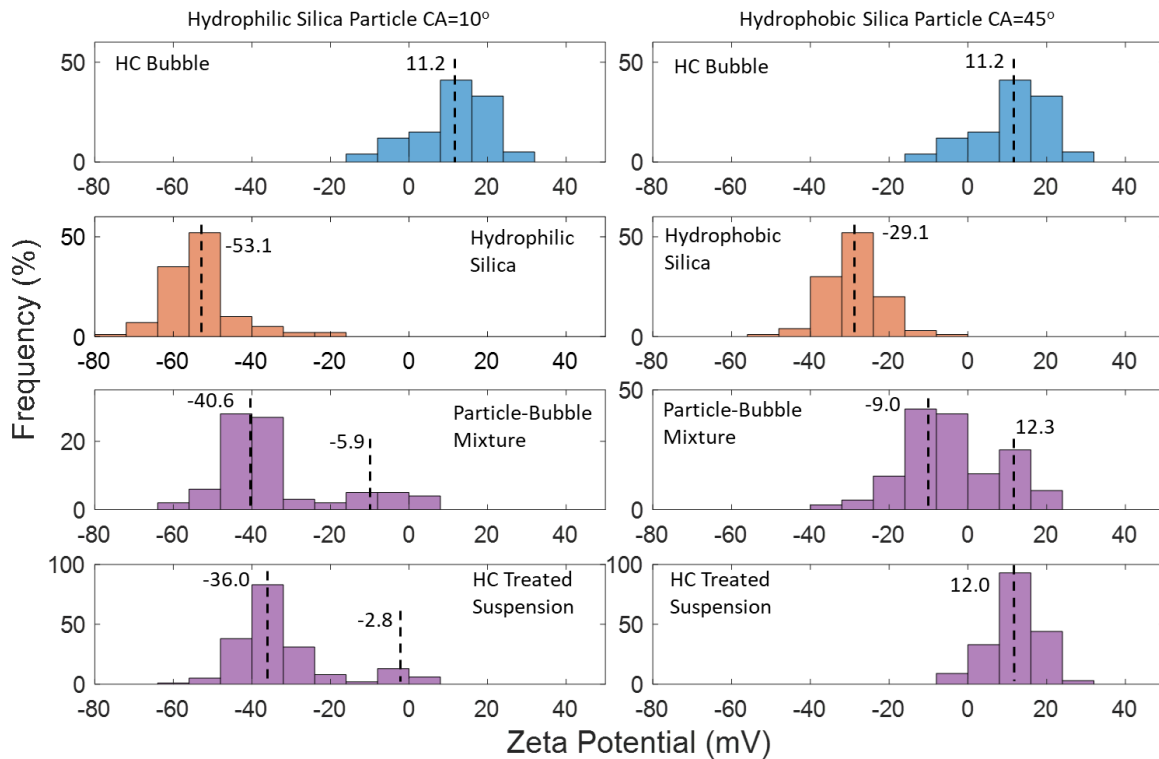
Figure 5.5. From top to bottom, the zeta-potential distributions of HC generated microbubbles, silica particles, HC bubble-particle mixture by stirring, and particle suspension after HC treatment. Slurries were prepared using hydrophilic silica (left) and hydrophobic silica (right). Slurries were prepared in 10 mM NaCl solution at natural pH of around 6.5. 0.1 mM cation surfactant DAH was added to differentiate the zeta-potential of bubbles from silica particles.

5.3.3. Particle aggregation by turbidity and size measurements

Increasing the apparent sizes of fine particles has been an effective method to improve particle recovery, as the collision probability with conventional flotation bubbles could be enhanced. Due to small bubble sizes, the microbubbles had high collision efficiency with fine particles [31], [200], [201], thus could be used as bridges that efficiently enhance

particle-particle interaction to form large particle aggregates. The previous bubble-frosting study has demonstrated the inherent bubble growth on the surface of hydrophobic fine particles by HC treatment, which revealed its potential in particle aggregation. In this study, the level of aggregation formation of 1 wt% particle suspension made with 6 μm silica was tested using the turbidity meter before and after HC treatment. The sizes of the silica suspensions were measured to further demonstrate the formation of aggregations after HC treatment.

The turbidites of silica suspension were measured as a function of settling time, as shown in **Fig. 5.6A**. The suspension of the hydrophilic particles (10°) before HC treatment has the most dispersed particles, as shown by the highest turbidity. After HC treatment, as expected, the suspension turbidity did not change remarkably considering the limited interactions between microbubbles and hydrophilic fine particles. For the hydrophobic particles, lower turbidities were observed even before HC treatment, indicating the natural formation of particle aggregates. The phenomenon became more obvious as the particle hydrophobicity increased. This could result from the hydrophobic forces that bonded particles during particle addition and mixing. The turbidity of hydrophobic silica suspension had a significant decrease after HC treatment. The results demonstrated the effect of HC microbubbles in enhancing aggregation formation, which reduced the number of fines in the suspension and thus increased the clarity of the slurry. The recorded images of the aggregate formation for hydrophobic (45°) particles before and after HC are shown in **Fig. 5.6B** and **5.6C**. The photos clearly displayed the slurry suspension before HC, and suggested the formation of large aggregates for the hydrophobic particles after cavitation.
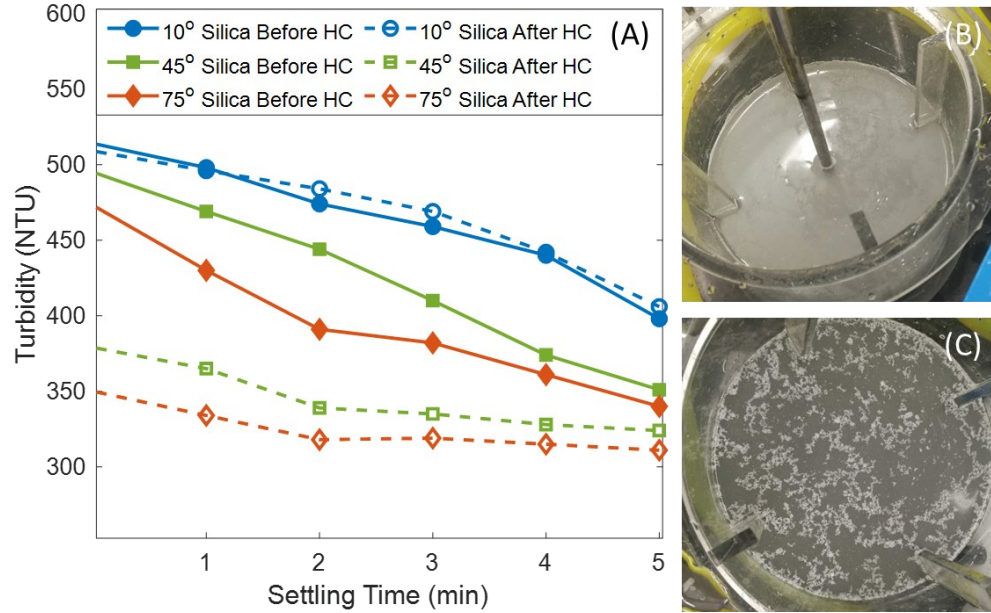
Figure 5.6. (A) Turbidity measurements of 1 wt% silica suspensions before and after cavitation as a function of time. (B) Image taken for 45° silica before cavitation; (C) Image taken for 45° silica after cavitation.

The particle size distribution of silica suspension before and after cavitation was measured using Mastersizer to directly measure the effect of cavitation on particle apparent size change. The equipment automatically measured particle sizes three times in each case to give a relatively representative average result, and the data are shown in **Table 5.1** and **Fig. 5.7**. For the hydrophilic silica (10°), the interactions between particles and bubbles were enhanced to a small extent after HC treatment, which was reflected by the slightly increased D50 from 6.6 to 8.2 μm. The D90 of the suspension after cavitation changed from 20.8 to 21.4 μm, in which most of the particles were still regarded as troublesome fine particles in the flotation process. For both batches of hydrophobic silica particles (CA = 45° and 75°) before cavitation treatment, even though the same theoretical particle sizes as the hydrophilic silica, they exhibited larger D90. The size differences explained the

lower turbidity compared to hydrophilic particle suspension, resulting from the small-degree particle aggregation formed by pre-existing surface bubbles and hydrophobic force. The changes in particle size distribution after HC treatment are illustrated in **Fig. 5.7**. The number frequency of particles larger than 10 μm decreased dramatically. Instead, large aggregates were formed shown by the new peaks over 100 μm. The aggregates seem to be formed by particles or small aggregates larger than 10 μm, which contained surface nuclei to facilitate the nucleation of surface bubbles. The results confirmed the selective behaviour of HC bubbles that mainly enhance the aggregation formation of hydrophobic particles. Large hydrophobic particle aggregates could originate from small complexes of hydrophobic particles and gas pockets after HC treatment. It coincided with the previous experiment that hydrophobic particles with surface bubbles had the best performance in bubble frosting after HC treatment.

Table 5.1. The particle size distribution of silica suspensions before and after cavitation

	Before/After Cavitation	Dx (10) (μm)	Dx (50) (μm)	Dx (90) (μm)
10º Silica	Before cavitation	0.92	6.62	20.8
10º Silica	After cavitation	1.01	8.15	21.4
45º Silica	Before cavitation	0.86	6.97	27.1
45º Silica	After Cavitation	0.99	10.1	400
90º Silica	Before cavitation	0.90	10.0	44.7
90º Silica	After Cavitation	1.02	12.8	291
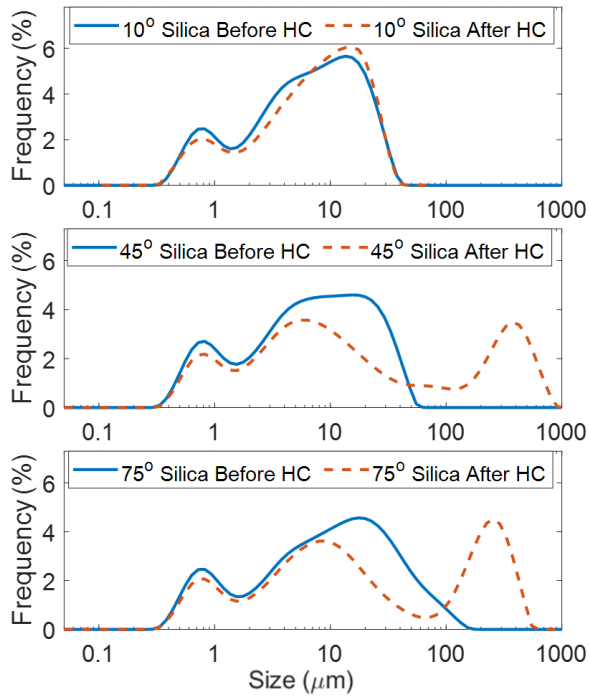
Figure 5.7. The particle size distribution of silica suspensions before and after HC treatment. From top to bottom, silica particles with characteristic contact angles of 10º, 45º, and 75º.

5.3.4. Bubble-solid attachment using bubble sliding under inclined glass surfaces

The bubble-solid attachment efficiency represented by the induction time was measured using motion-tracking of bubbles sliding under a hydrophilic glass surface (CA = 10º), a hydrophobic glass surface (CA = 45º), and a microbubble frosted glass surface. The bubbles with an average size of 0.9 mm had controlled rising velocity at around 0.1 m/s in DI water, thus had similar momentum when approaching the glass surfaces.

Fig. 5.8A shows the bubble rising/sliding velocity plotted against time. For hydrophilic glass, the bubble could not attach to the hydrophilic glass even up to 120 ms of measuring

time. More than five tests were conducted at this condition, and no obvious differences were observed. The low attachment efficiency was expected since the reported millimeter size bubble-hydrophilic solid surface induction time was at hundreds to thousands of milliseconds [117], [119], which was significantly longer than the 120 ms recording time. The bubble velocity profile under the 45° hydrophobic glass surface showed induction times lower than that for the hydrophilic glass. As indicated in the figure, three repeating tests were performed, and all the bubbles were able to attach to the glass within 100 ms. In the last experiment, bubbles contacted with a microbubble frosted glass surface and immediate attachments were observed. The tests were repeated several times with freshly made bubble-frosted glass surfaces, and consistent results were obtained. The microscopic image of microbubbles on the glass surface is shown in **Fig. 5.8B**. Using imaging analysis on three bubble pictures taken at different locations, the size distribution of surface microbubbles was obtained and is shown in **Fig. 5.8C**. The average bubble size of about 40 μm agreed with the bulk bubble size distribution shown earlier in **Fig. 5.1C**. These microbubbles significantly enhanced the bubble-solid attachment, which happened almost instantly after contact.

This study demonstrated the ability of surface microbubbles to greatly enhance the attachment between flotation size bubbles and solids. One hypothesis was proposed by Klassen and his coworkers [210], believing that the coalescent attachment between a large bubble and a tiny bubble required much less free energy than a direct attachment of a large flotation bubble on the particle. From the hydrodynamic perspective, the mechanism can be explained by the Reynolds lubrication theory, where the large Laplace pressure $2\sigma/R$ of small bubbles accelerates the thin liquid film drainage between two surfaces [123]. For

the surface microbubbles with radii around 10-20 μm, the theoretical coalescence time using the Stokes-Reynolds-Young-Laplace model is about 20 ms [123], [211], while the experimental value should be even shorter. Therefore, the presence of surface microbubbles contributed to the fast bubble-solid attachment, thus enhancing flotation recovery.
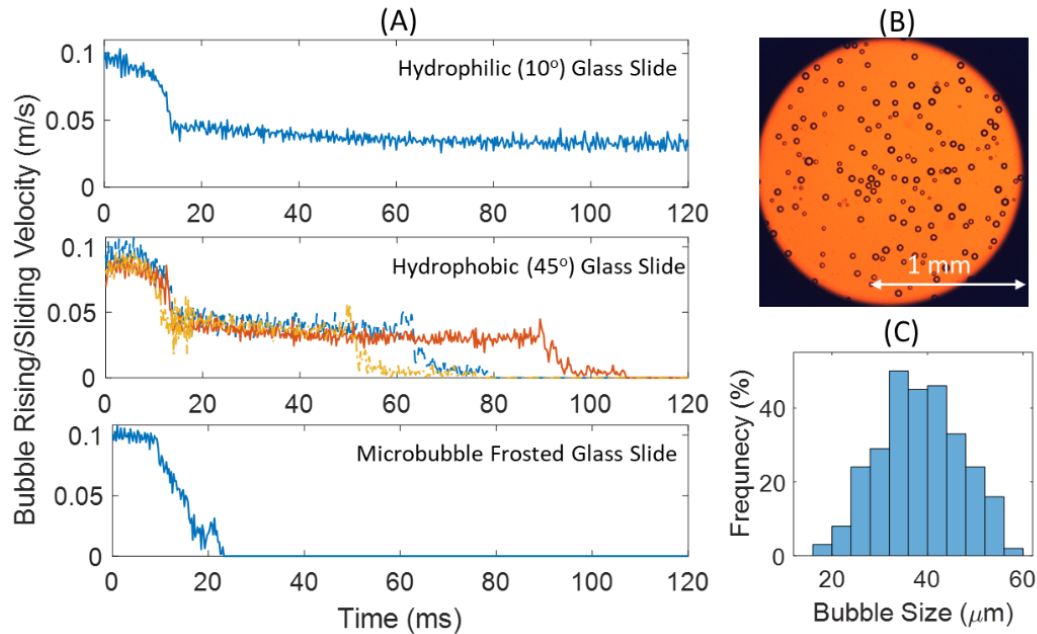
Figure 5.8. (A) The velocity of a bubble rising and sliding on a 30° tilted (1) hydrophilic glass, (2) hydrophobic glass and (3) microbubble-frosted glass. (B) The 10X microscopic image of the bubble-frosted glass surface and (C) the size distribution of surface bubbles.

5.4. Mechanism of HC Enhanced Fine Particle Flotation

The above results revealed that the floatability of hydrophobic fine particles could be significantly increased with HC. The data suggests that three sub-processes are collaboratively involved to selectively improve the flotation performance, as depicted in **Fig. 5.9.** In the first step, HC-generated microbubbles are preferably covered on

hydrophobic particles. Compared to microbubble-particle attachment by mixing, the bubble frosting process is more efficient by direct bubble nucleation on particle surfaces. This explains the particularly significant bubble frosting effect with hydrophobic particles, as the pre-existing surface gas pockets facilitate the bubble nucleation during the HC process.
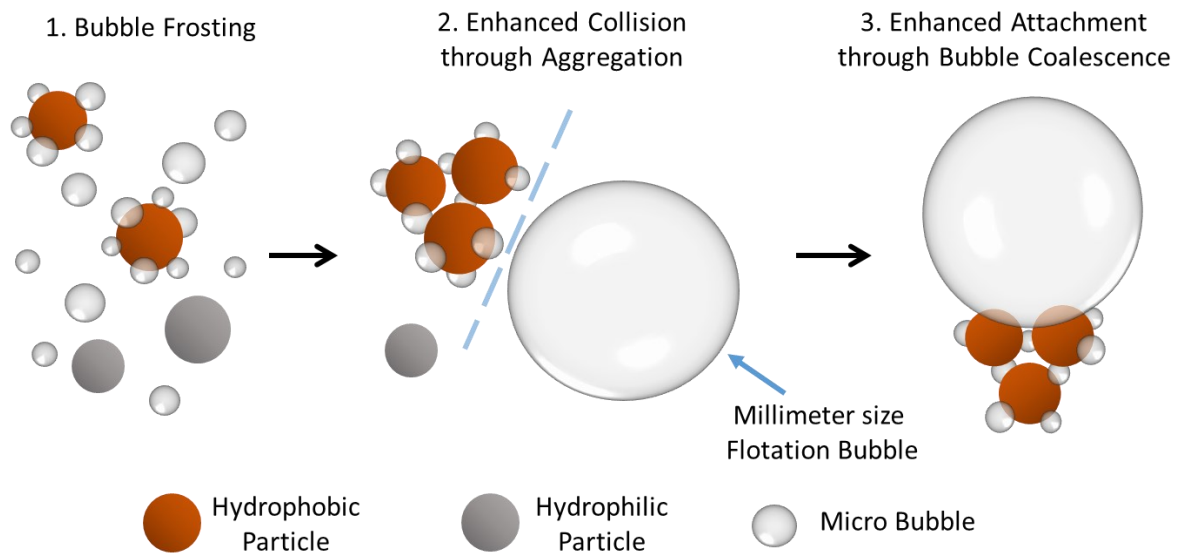
Figure 5.9. Schematic of the HC enhanced fine particle flotation.

The microbubbles on particle surfaces enhanced the latter particle-particle interaction, as the formation of aggregates by fine particles was observed after HC. Again, this was demonstrated to have a more profound impact on hydrophobic particles. Some researchers have shown that the HC-generated nanobubbles or microbubbles can modify the surface properties of particles, including the reduced surface charge density [44][41]. Others suggested that the capillary force contributes to the fast coalescence between microbubbles [212]. Either way, the surface microbubbles on hydrophobic particles act as bridges for fine particles to form large aggregates. Such an increase in particle apparent sizes could

significantly increase the collision efficiency between fine particles and flotation bubbles, as the collision efficiency is proportional to the square power of the particle size. In fact, the approach to improve flotation recovery by forming aggregates has been applied successfully in many fields.

However, the high collision efficiency does not necessarily translate to high floatability, as particle-bubble attachment also plays an important role in fine particle flotation. With particles covered with HC microbubbles, the attachment efficiency could be greatly improved as the induction time was reduced. It could be explained by the lower surface energy for coalescent bubble attachment and the fast liquid film drainage due to the high Laplace pressure of small bubbles. In this study, HC treatment appears to selectively improve the flotation performance for hydrophobic fine particles. It is believed that HC will improve both the flotation recovery and grade of concentrates.

5.5.   Summary

The effect of hydrodynamic cavitation on the flotation chemistry of fine hydrophilic and hydrophobic particles was investigated. Experimental results clearly indicated that hydrodynamic cavitation could improve the collection efficiency of single bubble-fine particles, and the effect was more pronounced for hydrophobic particles. Mechanisms were proposed for how hydrodynamic cavitation assists the flotation collection of fine particles. The combined effect of bubble frosting, aggregation formation, and microbubble bridged bubble-particle attachment resulted in improved collision and attachment efficiencies depending on the hydrophobicity of the particles. Particle zeta-potential measurements confirmed the bubble frosting on hydrophobic particles through the HC process. Measurements of the particle size distribution and turbidity suggested that large aggregates

formed for hydrophobic particles after hydrodynamic cavitation. The flotation bubble-solid attachment analysis indicated that the attachment efficiency of a large bubble with a solid surface was significantly improved after covering with surface microbubbles. For hydrophilic particles, both the collection efficiency and sub-processes tests showed limited improvement after HC treatment. On the other hand, the flotation performance could be significantly improved for hydrophobic particles after HC. The study strongly supports the potential of cavitation in improving the flotation recovery and selectivity of fine particles.

Chapter 6 Improvement of the Fine Particle Flotation by Optimized Parameters of Dual Bubble Generator

Abstract

The conventional froth flotation with millimeter-sized bubbles has faced challenges in recovering fine particles for decades. Using microbubbles generated from hydrodynamic cavitation with a designed Venturi tube enhanced fine particle flotation. The combination of conventional and cavitation bubbles is called the 'dual bubble method'. Previous studies demonstrated the effect of cavitation bubbles on particle-particle and bubble-particle interactions. In this study, a lab-scale flotation column was used to tune and optimize the synergy of cavitation bubbles and conventional bubbles. The optimized position of conventional bubble injection was investigated through bubble size and gas holdup measurements. Flotation tests used naturally hydrophobic molybdenite particles and hydrophilic silica particles to investigate particle recovery and grade improvement with different gas injection locations. Results demonstrate that the gas injection at the inlet of the Venturi tube prevented the generation of cavitation microbubbles but produced smaller size conventional bubbles, which resulted in a decrease in the flotation selectivity. For the downstream gas injection, a higher gas injection rate leads to a higher recovery rate at the expense of flotation selectivity. As the gas injection site is placed further from the Venturi tube, the grade of the desired mineral particles becomes higher, with the cost of lowered recovery.

6.1. Introduction

Froth flotation is a separation process that has been widely used in many industrial applications, including oil sands processing, wastewater treatment, and especially mineral processing [17]–[19], [21], [22], [161], [213], [214]. During the flotation process, air

bubbles are injected into the flotation column and interact with the particles through three sub-processes: collision, attachment, and detachment [31], [201]. The targeted minerals usually have higher attachment probabilities with the rising bubbles, leaving the unwanted particles at the column bottom [201], [215], [216]. For many years, fine particles with sizes smaller than 10-20 μm have faced recovery challenges due to the low collision probability [30], [32], [33], [36]. It has been reported that neither the small size of mineral particles nor the large size of conventional flotation-size bubbles is favorable for the bubble-particle collision and attachment processes [30], [31].

Many studies have been dedicated to developing the appropriate technology to improve the recovery of fine particles, such as reactive oily-bubble flotation, shear flocculation and selective polymer flocculation [162]–[164]. These methods improve the effective size of fine particles through aggregation, increasing the bubble/particle collision and attachment probabilities, and hence, the recovery of mineral particles can be enhanced. However, there are still several major problems such as expensive chemical dosage and energy consumption, strict physical and pH control, as well as low selectivity, which make it difficult to apply these techniques in industrial operations. In recent years, hydrodynamic cavitation, as a relatively simple and energy-efficient technology for microbubble generation [8], [51], [52], has shown great potential for increasing the recovery of fine particles [5], [46], [217]. By placing a Venturi tube in the recirculation loop at the bottom of the flotation column, cavitation can be triggered, and microbubbles are generated through gas nucleation on the tube wall or the surface of hydrophobic and rough particles. The microbubbles attached to the particle surfaces increase the hydrophobicity of the particle surface and provide higher Laplace pressure that offsets the disjoining pressure,

thus enhancing the attachment probability with the flotation-sized bubbles [45]–[47]. Moreover, the microbubbles increase the effective size of fine particles by aggregation, which leads to a higher bubble-particle collision probability [4], [48], [49].

In the flotation setup with the installation of the Venturi tube, the conventional bubbles provide the buoyancy force to float desired minerals, while the microbubbles generated by hydrodynamic cavitation assist in increasing the fine particle recovery. The fundamental study on the dual bubble method and positions of flotation-sized bubble injection with respect to the Venturi tube was still absent. In this study, the dual bubble method was studied by investigating the bubble size and gas holdup with gas injection at different locations, followed by the lab-scale selectivity tests between naturally hydrophobic molybdenite and hydrophilic silica particles.

6.2. Material and Methods

6.2.1. Experimental setup

The schematic of the experimental lab-scale flotation setup built to mimic the flotation process is shown in **Fig. 6.1a**. The core flotation system consists of a peristaltic pump, a gas injection site, and a flotation column of 107 cm in height and 5.1 cm in diameter. For the bubble size distribution measurement, three sources of bubble generation were studied. A Venturi tube was installed as the cavitation device to generate cavitation microbubbles. The flotation-sized bubbles that provide the most buoyancy force for mineral flotation were injected at 55 mm from the upstream (G1) or the downstream (G2) of a Venturi tube. Both gas injection sites were equipped with gas flow meters, and a sintered tube with a porosity of 20 μm was inserted at the Venturi tube outlet to generate flotation-sized bubbles. A flow

meter (Omega type FLR1001) and a pressure transducer (IKA RW 20 digital) were placed upstream of the Venturi tube to monitor the Venturi throat velocity and inlet pressure for cavitation inception measurement. The recirculation flow rate was kept constant throughout all the experiments to maintain the size of the injected bubbles [218]. A microphone (Florida Research Instrument 100-1) was placed at 1 cm above the Venturi tube to detect the signal radiated from bubble burst during cavitation [171], [219]. Through coaxial wire connections, the voltage signals from the flow meter, the pressure transducer and the hydrophone were received by the oscilloscope (Rigol DS1054Z), where the signals were converted to flow rate, pressure, and acoustic spectrum, respectively. The recirculation system was connected by a half-inch Tygon tube.
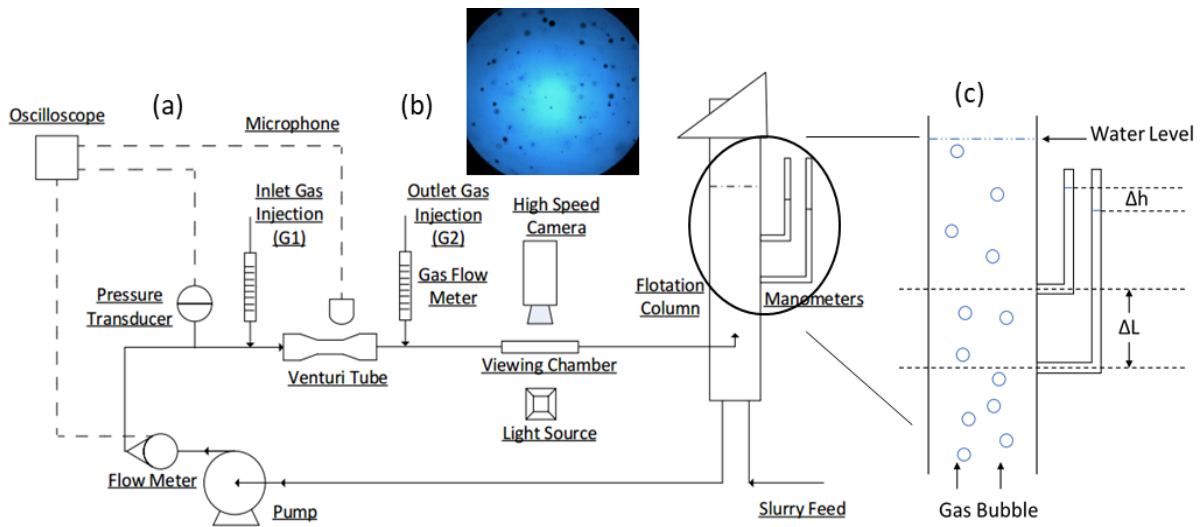
Figure 6.1. (a) Schematic diagram of the experimental setup. (b) Example of a high-speed camera image of bubbles generated without gas injection at throat velocity $V = 15$ m/s. The image is composed of 1024 x 1024 pixels with a scale of 1.8 µm/pixel. (c) Schematic diagram of the setup for gas holdup measurement.

6.2.2. Hydrodynamic cavitation device

The effect of geometrical parameters of the Venturi tube on the hydrodynamic cavitation system was reported in a previous study [147], [220]. Based on the findings, a Venturi tube with a high inlet angle and low outlet angle promotes hydrodynamic cavitation with lower flow resistance. **Figure 6.2. a** shows the geometry of the Venturi tube used in this study. The sintered porous ceramic tube for the generation of flotation-sized bubbles with the porosity of 20 μm was inserted at the entrance of gas injection sites G1 and G2, which were located about 55 mm apart from the inlet and outlet of the Venturi tube.
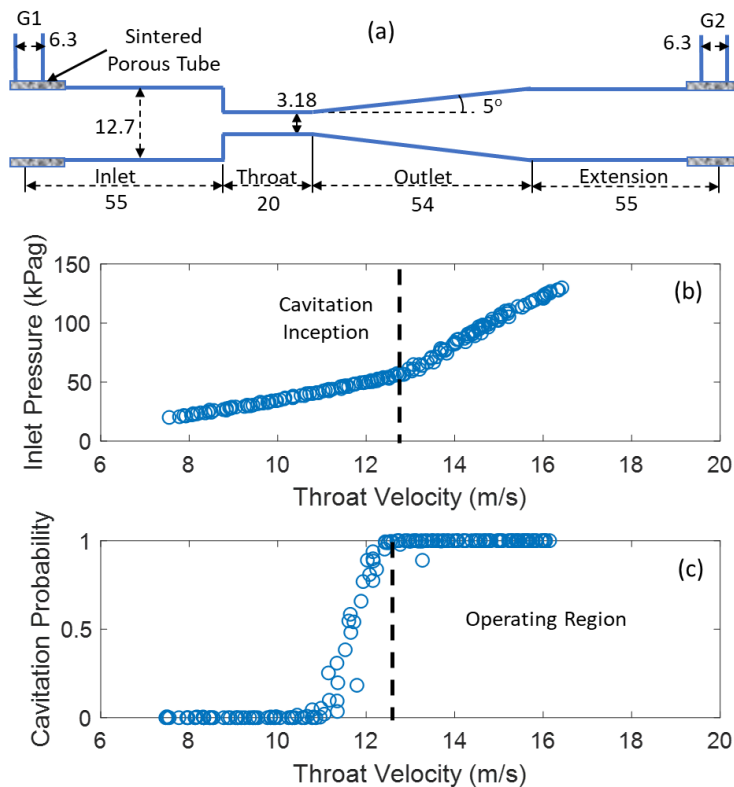
Figure 6.2. (a) Schematic design of the Venturi tube with labelled parameter in mm. The cavitation inception of this device was measured using (b) inlet pressure detection and (c) cavitation noise detection.

In addition, the cavitation performance of the studied Venturi tube was investigated to obtain the cavitation inception in terms of flow velocity at the Venturi throat. The experimental setup and studied methodology have been reported in the previous study [220]. The inception could be indicated by observing the inlet pressure change or detecting the cavitation noise using the hydrophone. As shown in **Fig. 6.2b**, the flow pressure at the tube inlet shows a deviated rising velocity at a throat velocity of about 12.5 m/s, representing the inception of cavitation due to the blockage effect caused by cavitation bubbles at vapor pressure in the Venturi tube. It is observed that the cavitation inception detected using a microphone agrees with the pressure detection, with the fully incepted cavitation also at about 12.5 m/s. Based on the inception measurement, the operating flow velocity at the Venturi throat was set at 15 m/s to ensure the occurrence of cavitation during the experiment.

6.2.3. Bubble size distribution measurement

The size distribution of bubbles generated by the hydrodynamic cavitation setup was monitored using a high-speed camera at 125 fps equipped with a high magnification lens (**Fig. 6.1b**). The observation was conducted through a glass-viewing chamber placed 26 cm downstream from the Venturi tube. A MATLAB code was developed to identify round objects and record their sizes in each image. The bubble quantity and size distribution were calculated using about 1,300 images for each experiment.

6.2.4. Gas holdup measurement

The volumetric fraction of gas in the flotation column, gas holdup (ϵ_g), is obtained by measuring the pressure difference between two tapping points using liquid manometers as shown in **Fig. 6.2c**. The gas holdup can be calculated using the equation:

$$\epsilon_g = 1 - \frac{\rho_w}{\rho_{sl}}\left(1 - \frac{\Delta h}{\Delta L}\right)$$
(6.1)

where ρ_w and ρ_{sl} are water density and slurry density, respectively. Δh and ΔL are the height differences between the slurry level and the tapping points. The gas holdup is a parameter that represents the overall bubble sizes. As the bubble rising velocity is inversely proportional to the bubble size, smaller bubbles result in a longer residence time in the column and higher gas holdup.

6.2.5. Particle preparation

In this study, fine molybdenite particles (D_{50} = 23.5 μm) were used as the target material in the flotation test. Samples were obtained from Teck Highland Valley Copper Partnership, Logan Lake, BC, Canada, with a purity of approximately 97.2% analyzed by XRF. For the hydrophilic particle representing the gangue material, fine silica was purchased from Discovery Gemstone with a purity of 98.58% analyzed by XRF examination. The silica particles were ground using the Shatter box to reach the mean particle size, D_{50} = 22.6 μm, similar to molybdenite particles. Their particle size distributions were measured by Malvin Mastersizer 3000 and are summarized in **Table 6.1.**

Table 6.1. Particle size parameters of molybdenite and silica particles.

	D_{10} (µm)	D_{50} (µm)	D_{90} (µm)
Molybdenite	12.6	23.5	52.2
Silica	2.8	22.6	85.5

6.2.6. Parameters of flotation tests

Methyl isobutyl carbinol (MIBC) purchased from Sigma Aldrich was used at 10 ppm concentration in the study as the frother. Tap water was used due to the considerable volumetric amount needed in each experiment. Flotation tests of the mixture of molybdenite and silica were conducted using the same setup as the bubble size study. 200 g particles in 3 L of the slurry were fed to the column up to the level of 25 cm below the column top. The pulp level was kept constant during the experiment with continuous water fed from the bottom of the column. The timer was started when the froth was first collected, and the collection times were at 0.5, 1, 2, 3 and 4 min. A riffler was used to prepare 2 g of each sample evenly, and one pellet of each sample was sent to XRF examination for assay analysis.

6.3.   Results and Discussion

6.3.1. Role of cavitation micro-bubbles in fine particle flotation

In the flotation process, the bubble size plays a significant role in the collision probability between either bubble/particle or bubble/bubble. The conventional bubbles

were injected in the column flotation to provide the buoyancy force for flotation. However, the interactions between those conventional bubbles and fine particles have poor performance and need to be assisted by microbubbles. In one of our previous studies, the collection efficiency of conventional bubbles to fine silica particles was improved with the help of microbubbles generated using hydrodynamic cavitation. The mechanism was explained by the enhanced particle-particle interactions, which increased the particle-bubble collision efficiency by forming large particle aggregates. The fundamental study by Liu et al. [221] also provided knowledge that microbubbles generated on particle surfaces make it easier to attach to the millimeter size bubbles. Furthermore, the effect of cavitation bubbles on improving particle-particle and particle-large bubble interactions becomes more significant with hydrophobic particles. This phenomenon can be utilized to enhance flotation selectivity.

6.3.2. Bubble size distribution by different gas injection

Fig. 6.3 presents the result of bubble size distribution in the presence and absence of gas injection at a controlled flow speed. The bubble sizes were analyzed from images taken by the high-speed camera at the Venturi tube. 10 ppm of MIBC was added to stabilize the bubble for a longer lifetime and decrease the bubble mean size. In the presence of inlet gas injection (gas injection from G1), larger bubbles were found. The bubble size distribution showed a wider diameter range compared to the bubbles in the absence of inlet gas injection. With 0.5 LPM of inlet gas injection, the mean bubble size is approximately 160 μm, which is much larger than the average cavitation bubbles at 25 μm without inlet gas injection (confirmed by the Mastersizer 3000 measurement at 27 μm). The decrease in microbubble generation and the increase in overall bubble size are explained by pre-existing large

119

bubbles during cavitation. It was reported that the required energy for bubble growth is smaller than that of bubble nucleation. Hence, the vaporized water and dissolved gas prefer to enter the pre-existing bubbles instead of forming new micron-size bubbles [1], [53], [57]. In addition, when the gas was injected at the inlet of the Venturi tube, the inlet pressure increased from 83 kPag to 117 kPag. Subsequently, the pressure in the Venturi throat increased, which lowered the tensile stress applied to the liquid phase and prevented the formation of microbubbles. The theories explained the large bubles size distribution as shown in **Fig. 6.3**, that tiny cavitation bubbles were absent when the air was injected from G1. Regarding the flotation size bubbles, the G1 injected bubbles were shattered into bubbles at about 160 μm under the Venturi tube's high shear and turbulent energy. By comparison, the size of conventional flotation bubbles injected from G2 was over 200 μm, which was still smaller than the real size due to the high-speed camera viewing area limit. Their sizes could be reflected by the gas holdup discussed in the next section. Results of bubble size distribution provide the supporting explanation in the column flotation experiments, which will be discussed further in this study.
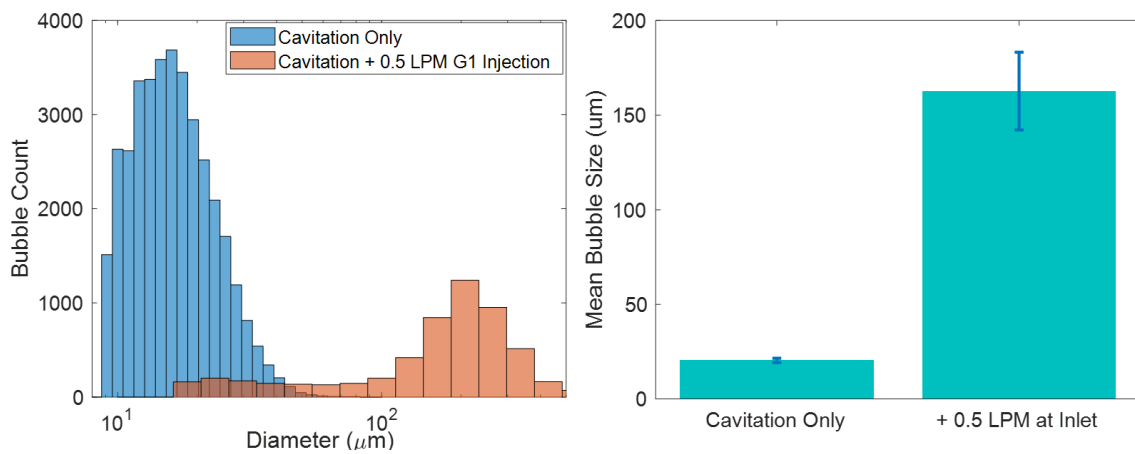
Figure 6.3. Comparison of bubble size distribution with and without 0.5 LPM of gas injection from the inlet of Venturi tube at throat velocity, $V = 15$ m/s, 10 ppm MIBC.

6.3.3. Gas holdup measurement

The gas holdups in the column sampling area with G1 and G2 injections were compared, and the gas holdup without the installation of cavitation sparger is shown as a reference in **Fig. 6.4**. It is worth noting that the low gas holdups shown in this study served as an indication for bubbles size comparison, where the tests were performed in an air/water two-phase system. The gas holdup tests were also performed in the three-phase condition at a higher gas injection rate, where the water was replaced by 6.7 wt.% slurries with 1.043 g/L of density. The gas holdup in the column increases from 10.5% to 15.6% with 2-4 liter per minute (LPM) of G1 gas injection and from 10.2% to 15.1% for G2 gas injection at the same rate. **Fig. 6.4** shows that the highest gas holdup was observed with G1 gas injection with and without MIBC, while the column without the infill of cavitation bubbles has the lowest gas holdup as expected. The high gas holdups from G1 injection were contributed to the massive smaller than conventional flotation bubbles, which were produced by the shattering of injected bubbles at the Venturi tube. As discussed by Miettinen et al., although decreasing the flotation bubble size can enhance the bubble/particle collection efficiency, the use of small bubbles also brings some challenges [36]. They noticed that the low rising velocity of smaller conventional bubbles adhered with mineral particles led to a longer flotation time, which is not preferred in the flotation operation. Also, one of the other main disadvantages is that the smaller bubbles result in high water recovery, and hence, the entrainment of undesired particles can be increased. The observation from **Fig. 6.4** will be further explained during selectivity tests in the next session.
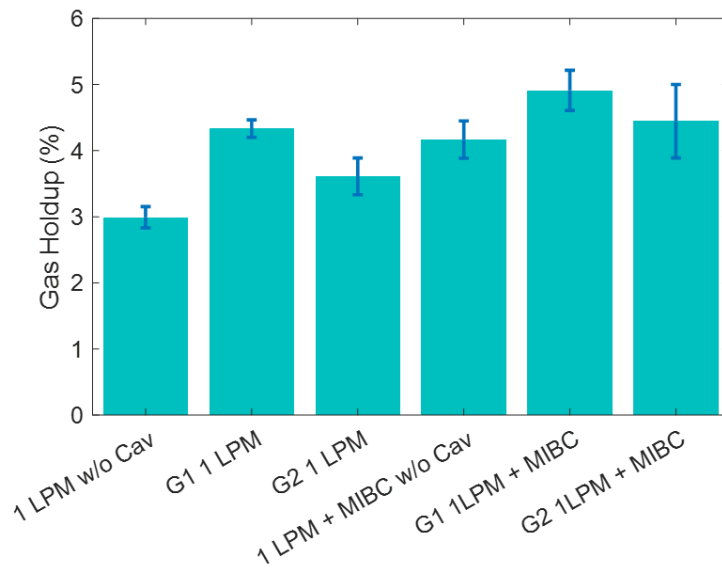
Figure 6.4. Gas holdup with and without hydrodynamic cavitation, with 1 LPM of gas injection from the inlet/outlet of Venturi tube at $V = 15$ m/s, 10 ppm MIBC. The tests were performed without the addition of particles.

6.3.4. Effect of cavitation bubbles and gas injection rate in particle flotation

The enhancement of fine particle flotation by cavitation bubbles was demonstrated in the column flotation test using 6.7 wt% molybdenite/silica mixture slurries at a 3:7 mass ratio. According to the above discussion, experiments were conducted with gas injection from 2 to 4 LPM at the outlet injection site G2 to avoid the disturbance to cavitation microbubble generation. As a reference, flotation tests without hydrodynamic cavitation were performed by replacing the Venturi tube with a hollow tube with a gas injection at 3 LPM. The results are presented in **Fig. 6.5**. The tests without hydrodynamic cavitation had obvious lower recovery and grade compared to the ones with cavitation microbubbles. The

results confirmed the previous studies that the cavitation bubbles increase fine particle recovery through (1) enhancing particle-particle interactions to form large aggregates, thereby promoting the collision probability with conventional bubbles, and (2) enhancing particle-conventional bubble interactions to increase attachment efficiency. In addition, the beneficial effects of cavitation bubbles are more significant with hydrophobic particles; thus, promoting the flotation selectivity.

By increasing the gas injection rate from 3 LPM to 4 LPM, a higher recovery was obtained, but with the cost of a lower grade. The result is as expected since a large number of conventional bubbles could collect gangue materials by entrainment. Despite that, the grade of cavitation flotation with 4 LPM gas injection was similar to that without cavitation bubbles with 3 LPM injection, while a significant improvement in particle recovery of over 10% was obtained. Vice versa, a lower recovery similar to the tests without cavitation was obtained by decreasing the gas injection rate from 3 LPM to 2 LPM. Still, the grade was significantly increased with the help of cavitation bubbles. The results indicated that both the flotation recovery and grade could be improved by introducing the hydrodynamic cavitation setup onto the flotation column. By tuning the gas injection rate downstream of the cavitation sparger, a higher recovery can be achieved with the expense of grade and vice versa.
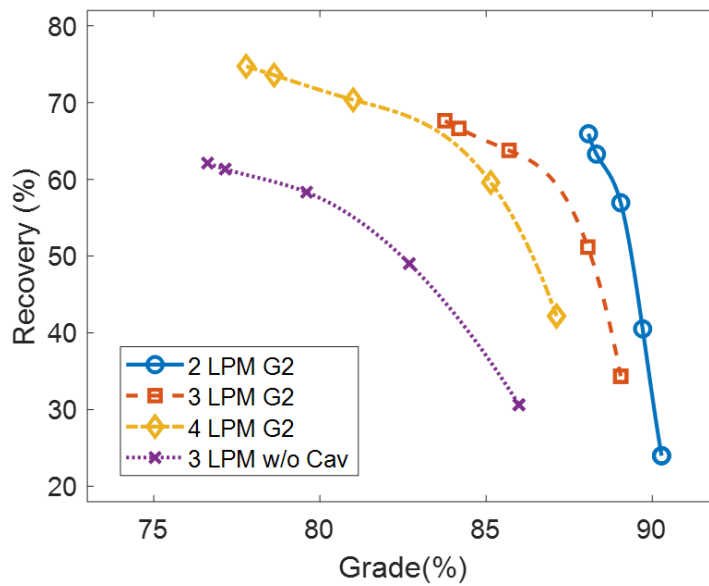
Figure 6.5. Recovery vs Grade of molybdenite in selectivity tests of 6.7 wt% molybdenite/silica mixture used as the slurry feed. Conventional air bubbles were injected from G2 at rates from 2 LPM to 4 LPM. Flotation without installing the cavitation device was performed with an injection rate at 3 LPM as a reference.

6.3.5. Flotation tests with different G1/G2 gas injection ratio

As discussed previously, the inlet or outlet gas injection (from G1 or G2) leads to various mechanisms of bubble formation with different size distributions. To confirm the disadvantages of inlet gas injection, flotation tests were conducted with a total of 3 LPM of gas injection from G1 and G2 at different ratios. The flotation results are presented in **Fig. 6.6**. It can be noticed that the grade of molybdenite particles decreased with the increase of the amount of G1 gas injection. In other words, more entrainment of silica particles occurred with the injection of gas at the G1 position. The flotation results agree with the bubble size study that the gas injection at the G1 position is unfavourable for the

targeted mineral particles. The millimeter bubbles generated at G2 prevented the nucleation of microbubbles and lowered the conventional bubble size which possibly causes the entrainment of unwanted particles. In addition, the conventional bubble-particle aggregates formed at the inlet of the Venturi tube must subsequently travel through the turbulent Venturi region, which could potentially increase the detachment probability of molybdenite particles from air bubbles [147]. On the other hand, gas injection at G2 prevented the interference of pre-existing conventional bubbles on hydrodynamic cavitation, which could generate microbubbles on the surface of particles. Subsequently, the bubble-covered particles encountered freshly injected conventional bubbles at G2 to achieve the perfect dual-bubble flotation. In this circumstance, the detachment probability of the aggregates from the flotation-sized bubbles can be reduced. Overall, conventional bubble injection from the downstream of cavitation sparger is desired.
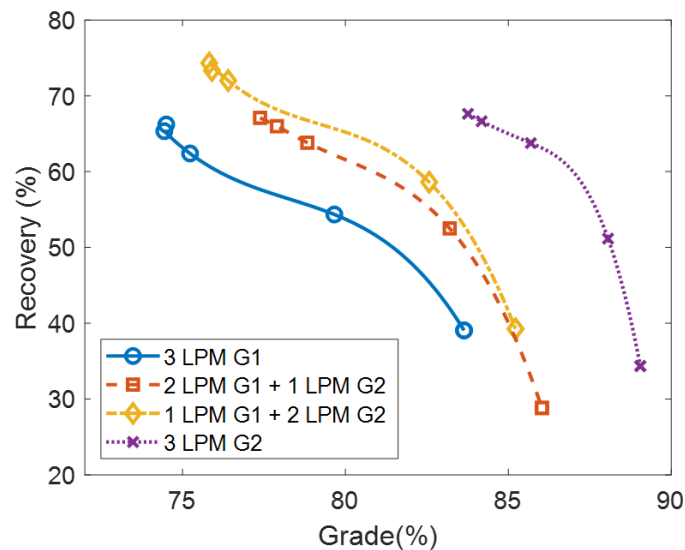

Figure 6.6. Recovery vs Grade of molybdenite in selectivity tests of 3 L of 6.7 wt% molybdenite/silica mixture used as the slurry feed. The total gas injection rate is 3 LPM divided by G1 and G2 injection locations at different ratios.

6.3.6. Optimization of gas injection location apart from cavitation sparger

After identifying G2 as the preferred gas injection site, the distance between G2 and Venturi tube requires identification to optimize the dual bubble method. Three groups of flotation tests were conducted with G2 placed at 55 mm, 80 mm, and 120 mm away from the end of the Venturi tube. As shown in **Fig. 6.7**, longer distance results in lower recovery but higher grade. The results could be explained by the small sizes of cavitation bubbles undergoing large Laplace pressure, which results in a short lifetime after leaving the Venturi tube. Furthermore, surfactant gradually accumulates on the surface of bubbles, preventing the coalescence between them [46]. With the closest G2 position to the Venturi tube (55 mm), the bridging microbubbles at their greatest number can benefit the attachment to either molybdenite or silica particles to form aggregates, which are followed by the further attachment to the large fresh bubbles. Thus, at the G2 injection site 55 mm apart, the recovery of molybdenite was higher. Still, the grade was relatively lower as the recovery of gangue silica also increased from the cavitation microbubbles. For the longer distance of G2 placement, a better grade and a lower recovery were obtained. It was elucidated that the attachment between silica particles and microbubbles is due to entrainment, while the attachment between molybdenite particles and microbubbles is by physical attraction. Due to the long travelling distance before they meet the fresh bubbles, silica particles are more likely detached from microbubbles. Hence, the molybdenite grade in the concentrate is the highest for the case of 120 mm
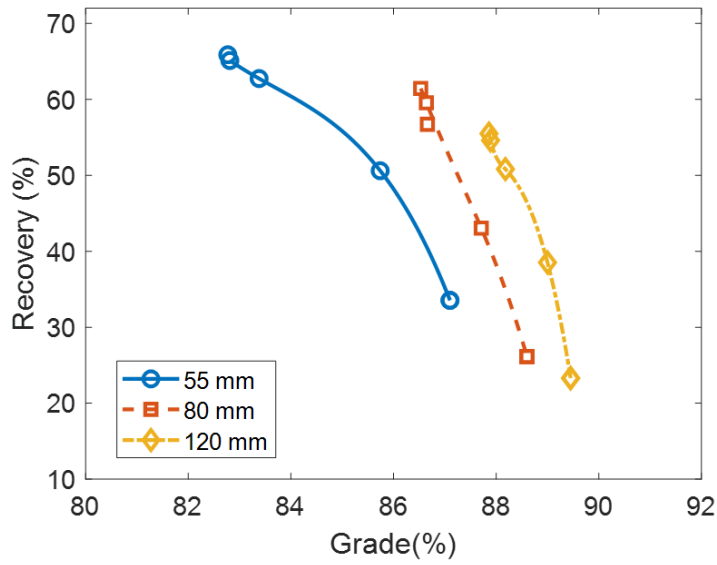
Figure 6.7. Recovery vs Grade of molybdenite with G2 placed 55 mm, 80 mm, and 120 mm away from the end of the Venturi tube.

6.4.   Conclusions

In the dual bubble flotation study, the location of flotation bubble injection with respect to the cavitation sparger was optimized by measuring overall bubble size distribution and gas holdup. The mean size of the cavitation bubble without gas injection upstream was measured to be about 25 μm. However, the gas injection at the Venturi tube inlet prevented the formation of the small cavitation bubbles and replaced them with shattered conventional bubbles with mean sizes of about 170 μm. Such conventional bubbles resulted in a higher gas holdup, which would cause entrainment of gangue material and low flotation grade. The flotation tests on the molybdenite/silica mixture were performed to demonstrate the effect of the dual bubble in fine flotation. Compared to conventional flotation without hydrodynamic cavitation, higher recovery and grade were obtained with conventional bubbles injected downstream of the cavitation sparger. The improvement in

the recovery and grade can be tuned by adjusting the gas injection rate. A low grade of targeted molybdenite particles was collected by injecting gas upstream of the cavitation sparger, which agreed with the bubble size study. At last, an investigation of the effect of gas injection positions showed that a higher grade was achieved with a longer distance between the Venturi tube outlet and the gas injection site, but the recovery was lower. This study revealed a new perspective to improve the selectivity of desired mineral particles in the flotation column operation.

Chapter 7 Conclusions and Future Work

7.1. Conclusions

The mechanism of hydrodynamic cavitation inception induced by Venturi tubes in both two-phase and three-phase systems was experimentally investigated in this work. By applying this technique, the roles of cavitation microbubbles in fine particle flotation were fundamentally understood and experimentally demonstrated.

In the water/air two-phase system, the inception of hydrodynamic cavitation was promoted with the addition of NaCl. However, the inception barely changed when salt was introduced into solutions with constant gas saturation levels. The decrease explained the mechanism for the change in gas solubility with the presence of electrolytes. Dissolved gas molecules entered or left the pre-existing gas nuclei when the gas saturation level was altered, thus affecting the tensile strength of the liquid. The air-saturation level of degassed DI water was changed from 0.5 to 1 by gas injection or salt addition, and the cavitation was promoted from 0.2 to 0.5 in cavitation inception number, which was calculated based on the inception velocity at Venturi throat. Further increase in the air content caused oversaturation, which induced visible bubbles that greatly promoted hydrodynamic cavitation. Knowing the gas saturated level as the major reason for inception change, CO_2 was utilized as an innovative additive for cavitation inception control, as its solubility is highly dependent on solution pH. The effect and reversibility of this method were demonstrated by altering the pH of carbonated solutions between 4 and 8, and the cavitation inception number reached the same level at about 1.2 and 0.2 within the 11 test runs. The

results suggested it as a reversible process to be potentially utilized in industrial applications that require early or late hydrodynamic cavitation.

The content of gas nuclei liquid, as the major factor affecting the liquid tensile strength and cavitation inception, depended on the surface properties of solids in the three-phase systems. The presence of hydrophilic particles stabilized the tiny gas nuclei in bulk water, which accelerated the inception of hydrodynamic cavitation from 22 m/s to 19 m/s in Venturi throat velocity. Moreover, the addition of hydrophobic particles further promoted cavitation, regardless of the particle surface roughness and particle sizes. The mechanism of particle wettability effect was demonstrated to be the introduction of gas pockets, as similar inceptions were obtained using pre-degassed solutions that prevented the formation of surface bubbles. By replacing the glass-made hydrophilic cavitation tube at 10° contact angle with a 3D printed tube with similar geometry and contact angle at 55°, the hydrodynamic cavitation inception was dropped to 15 m/s if particles with lower contact angles were present. The distinct effects of hydrophobic and hydrophilic particles on the inception of hydrodynamic cavitation preliminarily revealed its benefit potential in both the recovery and selectivity of the mineral flotation process.

The detailed mechanism of cavitation microbubbles on the flotation of hydrophilic and hydrophobic fine particles was investigated next. Single bubble flotation tests indicated that hydrodynamic cavitation could improve the bubble collection efficiency with hydrophobic particles. The results were explained from three aspects: (1) Microbubbles were preferably covered on hydrophobic particle surfaces during the hydrodynamic cavitation process to modify the particle surface properties. (2) particle-particle interactions were enhanced with the presence of microbubbles to form large aggregates, which

increased the particle collision probability with flotation bubbles. (3) The large flotation bubbles could easily attach to solids with surface microbubbles. All three factors were particularly effective for hydrophobic particles, which explained the improved collection efficiency compared to hydrophilic ones. These results strongly support hydrodynamic cavitation's potential in improving the flotation recovery and selectivity of fine particles.

The beneficial effect of hydrodynamic cavitation in fine particle flotation was demonstrated using a lab-scale flotation column with molybdenite and silica particle mixture. The location of flotation bubble injection with respect to the cavitation sparger was optimized by measuring the overall bubble size distribution and gas holdup. By gas injection upstream of cavitation sparger, the generation of cavitation bubbles at about 25 μm was hindered. Instead, the flotation bubbles were shattered from over 200 μm to about 160 μm when passing through the Venturi tube. Such a decrease in flotation bubble size resulted in a higher gas holdup and a lower flotation selectivity due to entrainment. By comparison, both cavitation microbubbles and large flotation bubbles were present in the system if flotation bubbles were injected downstream of the cavitation sparger. The combination of cavitation bubbles in tens of micrometers and injected flotation bubbles in hundreds of mcirometers formed the ideal dual-bubble technique, which improved both the recovery and grade of fine particle flotation. The improvement in the recovery and grade can be tuned by adjusting the gas injection rate. The distance of gas injection from the cavitation sparger was also investigated. A higher grade was achieved with a longer distance between the Venturi tube outlet and the gas injection site, but the recovery was lower.

7.2. Future work

Based on the developed experimental method and findings, several research areas are suggested for future study.

- In Chapter 3, the addition of NaCl was demonstrated to enhance hydrodynamic cavitation by lowering the gas solubility. By contrast, it is worth investigating the type of salts that increases the gas solubility of the solution, which would potentially prevent the occurrence of hydrodynamic cavitation.

- The presence of gas pockets on hydrophobic particle surfaces reduced the tensile strength of the liquid and enhanced cavitation. The detailed mechanism of the gas pocket formation on particles of different surface properties should be studied.

- The surface microbubbles could efficiently improve the attachment between a flotation bubble and a flat surface, regardless of its hydrophobicity. The microbubbles provided high Laplace pressure that accelerated the thin liquid film drainage. The bubble attachment with a solid rough surface with spikes in micro sizes should be explored and compared with attachment with a microbubble frosted surface.

- It is worth confirming the effect of hydrodynamic cavitation in an industrial-scale flotation process experimentally.

References

[1] E. Christopher, Brennen, *Cavitation and bubble dynamics*. 2013.

[2] Z. A. Zhou, Z. Xu, and J. A. Finch, "On the role of cavitation in particle collection during flotation - a critical review," *Miner. Eng.*, vol. 7, no. 9, pp. 1073–1084, Sep. 1994, doi: 10.1016/0892-6875(94)00053-0.

[3] Z. Zhou, Z. Xu, J. A. Finch, H. Hu, and S. R. Rao, "Role of hydrodynamic cavitation in fine particle flotation," *Int. J. Miner. Process.*, vol. 51, no. 1–4, pp. 139–149, 1997, doi: 10.1016/S0301-7516(97)00026-4.

[4] Z. A. Zhou, Z. Xu, J. A. Finch, H. Hu, and S. R. Rao, "Role of hydrodynamic cavitation in fine particle flotation," *Int. J. Miner. Process.*, vol. 51, no. 1–4, pp. 139–149, 1997, doi: 10.1016/S0301-7516(97)00026-4.

[5] H. Li, "Role of hydrodynamic cavitation in fine particle flotation," *Int. J. Miner. Process.*, vol. 51, no. 1–4, pp. 139–149, 2014, doi: 10.1016/S0301-7516(97)00026-4.

[6] S. Calgaroto, A. Azevedo, and J. Rubio, "Flotation of quartz particles assisted by nanobubbles," *Int. J. Miner. Process.*, vol. 137, pp. 64–70, Apr. 2015, doi: 10.1016/j.minpro.2015.02.010.

[7] Yusuf G. Adewuyi, "Sonochemistry: environmental science and engineering applications," *Ind. Eng. Chem. Res*, no. 40, pp. 4681–4715, 2001, doi: 10.1021/ie010096l.

[8]   J. Carpenter, M. Badve, S. Rajoriya, S. George, V. K. Saharan, and A. B. Pandit, "Hydrodynamic cavitation: an emerging technology for the intensification of various chemical and physical processes in a chemical process industry," *Rev. Chem. Eng.*, vol. 33, no. 5, 2016, doi: 10.1515/revce-2016-0032.

[9]   S. Arrojo, Y. Benito, and A. Martínez Tarifa, "A parametrical study of disinfection with hydrodynamic cavitation," *Ultrason. Sonochem.*, vol. 15, no. 5, pp. 903–908, 2008, doi: 10.1016/j.ultsonch.2007.11.001.

[10]   M. Dular *et al.*, "Use of hydrodynamic cavitation in (waste)water treatment," *Ultrason. Sonochem.*, vol. 29, pp. 577–588, 2016, doi: 10.1016/j.ultsonch.2015.10.010.

[11]   K. K. Jyoti and A. B. Pandit, "Water disinfection by acoustic and hydrodynamic cavitation," *Biochem. Eng. J.*, vol. 7, no. 3, pp. 201–212, 2001, doi: 10.1016/S1369-703X(00)00128-5.

[12]   G. E. Totten, Y. H. Sun, R. J. Bishop, and X. Lin, "Hydraulic system cavitation: A review," in *SAE Technical Papers*, 1998, vol. 107, no. 1998, pp. 368–380, doi: 10.4271/982036.

[13]   R. Singh, S. K. Tiwari, and S. K. Mishra, "Cavitation erosion in hydraulic turbine components and mitigation by coatings: Current status and future needs," *J. Mater. Eng. Perform.*, vol. 21, no. 7, pp. 1539–1551, 2012, doi: 10.1007/s11665-011-0051-9.

[14]   P. Kumar and R. P. Saini, "Study of cavitation in hydro turbines—A review," *Renew. Sustain. Energy Rev.*, vol. 14, pp. 374–383, Jan. 2010, doi:

10.1016/j.rser.2009.07.024.

[15]   G. Kuiper, "Chapter 4: Physics of cavitation : Cavitation Inception," *Cavitation Sh. Propuls.*, pp. 17–27, 2010.

[16]   M. Fan, D. Tao, R. Honaker, and Z. Luo, "Nanobubble generation and its application in froth flotation (part I): nanobubble generation and its effects on properties of microbubble and millimeter scale bubble solutions," *Min. Sci. Technol.*, vol. 20, no. 1, pp. 1–19, 2010, doi: 10.1016/S1674-5264(09)60154-X.

[17]   L. L. Schramm and R. J. Mikula, "Froth flotation of oil sand bitumen," *Foam Eng. Fundam. Appl.*, pp. 251–281, 2012, doi: 10.1002/9781119954620.ch12.

[18]   J. Masliyah, Z. J. Zhou, Z. Xu, J. Czarnecki, and H. Hamza, "Understanding water-based bitumen extraction from athabasca oil sands," *Can. J. Chem. Eng.*, vol. 82, no. 4, pp. 628–654, 2008, doi: 10.1002/cjce.5450820403.

[19]   F. Rao and Q. Liu, "Froth treatment in athabasca oil sands bitumen recovery process: A review," *Energy and Fuels*, vol. 27, no. 12, pp. 7199–7207, 2013, doi: 10.1021/ef4016697.

[20]   T. Kasongo, Z. Zhou, Z. Xu, and J. Masliyah, "Effect of clays and calcium ions on bitumen extraction from Athabasca oil sands using flotation," *Can. J. Chem. Eng.*, vol. 78, no. 4, pp. 674–681, 2000, doi: 10.1002/cjce.5450780409.

[21]   J. A. Finch and C. A. Hardie, "Example of innovation from the waste management industry: Deinking flotation cells," *Miner. Eng.*, vol. 12, no. 5, pp. 467–475, 1999, doi: 10.1016/S0892-6875(99)00030-8.

[22] C. qing Wang, H. Wang, J. gang Fu, and Y. nian Liu, "Flotation separation of waste plastics for recycling-A review," *Waste Manag.*, vol. 41, pp. 28–38, 2015, doi: 10.1016/j.wasman.2015.03.027.

[23] M. C. Fuerstenau, J. Graeme, and R. H. Yoon, "Froth flotation: a century of innovation," *Flotat. Chem.*, p. 89, 2007.

[24] D. Fuerstenau, "The Froth Flotation Century," in *Advances in flotation technology*, 1999, pp. 3–22.

[25] B. A. Wills and T. Napier-Munn, "Wills' mineral processing technology: an introduction to the practical aspects of ore treatment and mineral recovery," in *American Mineralogist*, 2015.

[26] Z. Dai, D. Fornasiero, and J. Ralston, "Particle–bubble collision models — a review," *Adv. Colloid Interface Sci.*, vol. 85, no. 2–3, pp. 231–256, Mar. 2000, doi: 10.1016/S0001-8686(99)00030-5.

[27] R.-H. Yoon, "The role of hydrodynamic and surface forces in bubble–particle interaction," *Int. J. Miner. Process.*, vol. 58, no. 1–4, pp. 129–143, Feb. 2000, doi: 10.1016/S0301-7516(99)00071-X.

[28] D. Tao, "Role of Bubble Size in Flotation of Coarse and Fine Particles—A Review," *Sep. Sci. Technol.*, vol. 39, no. 4, pp. 741–760, 2005, doi: 10.1081/SS-120028444.

[29] J. Ralston, D. Fornasiero, and R. Hayes, "Bubble–particle attachment and detachment in flotation," *Int. J. Miner. Process.*, vol. 56, no. 1–4, pp. 133–164,

Apr. 1999, doi: 10.1016/S0301-7516(98)00046-5.

[30] L. Parkinson and J. Ralston, "Dynamic aspects of small bubble and hydrophilic solid encounters," *Adv. Colloid Interface Sci.*, vol. 168, no. 1–2, pp. 198–209, 2011, doi: 10.1016/j.cis.2011.08.002.

[31] Z. Dai, D. Fornasiero, and J. Ralston, "Particle-bubble collision models--a review," *Adv. Colloid Interface Sci.*, vol. 85, no. 2–3, pp. 231–56, 2000, doi: 10.1016/S0001-8686(99)00030-5.

[32] D. Feng and C. Aldrich, "Effect of particle size on flotation performance of complex sulphide ores," *Miner. Eng.*, vol. 12, no. 7, pp. 721–731, 1999, doi: 10.1016/S0892-6875(99)00059-X.

[33] W. J. Trahar and L. J. Warren, "The flotability of very fine particles - A review," *Int. J. Miner. Process.*, vol. 3, no. 2, pp. 103–131, 1976, doi: 10.1016/0301-7516(76)90029-6.

[34] W. J. Trahar, "A rational interpretation of the role of particle size in flotation," *Int. J. Miner. Process.*, vol. 8, no. 4, pp. 289–327, 1981, doi: 10.1016/0301-7516(81)90019-3.

[35] E. T. Woodburn, R. P. King, and R. P. Colborn, "The effect of particle size distribution on the performance of a phosphate flotation process," *Metall. Mater. Trans. B*, vol. 2, no. 11, pp. 3163–3174, Nov. 1971, doi: 10.1007/BF02814969.

[36] T. Miettinen, J. Ralston, and D. Fornasiero, "The limits of fine particle flotation," *Miner. Eng.*, vol. 23, no. 5, pp. 420–437, 2010, doi:

10.1016/j.mineng.2009.12.006.

[37]   Y. A. Attia, "Synthesis of PAMG chelating polymers for the selective flocculation of copper minerals," *Int. J. Miner. Process.*, vol. 4, no. 3, pp. 191–208, 1977, doi: 10.1016/0301-7516(77)90002-3.

[38]   S. Song, A. Lopez-Valdivieso, J. L. Reyes-Bahena, and C. Lara-Valenzuela, "Floc flotation of galena and sphalerite fines," *Miner. Eng.*, vol. 14, no. 1, pp. 87–98, 2001, doi: 10.1016/S0892-6875(00)00162-X.

[39]   J. Rubio, F. Capponi, and E. Matiolo, "Flotation of sulphides ore fines and ultrafines particles," *IMPC 2006 - Proc. 23rd Int. Miner. Process. Congr.*, pp. 587–592, 2006.

[40]   P. Somasundaran, "Role of surface chemistry of fine sulphides in their flotation," in *Complex sulphide ores*, 1980, pp. 118–127.

[41]   M. Fan, D. Tao, R. Honaker, and Z. Luo, "Nanobubble generation and its applications in froth flotation (part II): fundamental study and theoretical analysis," *Min. Sci. Technol.*, vol. 20, no. 2, pp. 159–177, Mar. 2010, doi: 10.1016/S1674-5264(09)60179-4.

[42]   M. Fan, D. Tao, R. Honaker, and Z. Luo, "Nanobubble generation and its applications in froth flotation (part III): specially designed laboratory scale column flotation of phosphate," *Min. Sci. Technol.*, vol. 20, no. 3, pp. 317–338, May 2010, doi: 10.1016/S1674-5264(09)60205-2.

[43]   M. Fan, D. Tao, R. Honaker, and Z. Luo, "Nanobubble generation and its

applications in froth flotation (part IV): mechanical cells and specially designed column flotation of coal," *Min. Sci. Technol.*, vol. 20, no. 5, pp. 641–671, Sep. 2010, doi: 10.1016/S1674-5264(09)60259-3.

[44]   A. Sobhy and D. Tao, "Nanobubble column flotation of fine coal particles and associated fundamentals," *Int. J. Miner. Process.*, vol. 124, pp. 109–116, 2013, doi: 10.1016/j.minpro.2013.04.016.

[45]   R. Ahmadi, D. A. Khodadadi, M. Abdollahy, and M. Fan, "Nano-microbubble flotation of fine and ultrafine chalcopyrite particles," *Int. J. Min. Sci. Technol.*, vol. 24, no. 4, pp. 559–566, 2014, doi: 10.1016/j.ijmst.2014.05.021.

[46]   H. Li, A. Afacan, Q. Liu, and Z. Xu, "Study interactions between fine particles and micron size bubbles generated by hydrodynamic cavitation," *Miner. Eng.*, vol. 84, pp. 106–115, 2015, doi: 10.1016/j.mineng.2015.09.023.

[47]   Z. A. Zhou, Z. Xu, J. A. Finch, J. H. Masliyah, and R. S. Chow, "On the role of cavitation in particle collection in flotation – A critical review. II," *Miner. Eng.*, vol. 22, no. 5, pp. 419–433, 2009, doi: 10.1016/j.mineng.2008.12.010.

[48]   D. Tao, S. Yu, X. Zhou, R. Q. Honaker, and B. K. Parekh, "Picobubble column flotation of fine coal," *Int. J. Coal Prep. Util.*, vol. 28, no. 1, pp. 1–14, 2008, doi: 10.1080/07349340701640901.

[49]   W. Zhou, H. Chen, L. Ou, and Q. Shi, "Aggregation of ultra-fine scheelite particles induced by hydrodynamic cavitation," *Int. J. Miner. Process.*, vol. 157, pp. 236–240, 2016, doi: 10.1016/j.minpro.2016.11.003.

[50]   M. Li, A. Bussonnière, M. Bronson, Z. Xu, and Q. Liu, "Study of Venturi tube

geometry on the hydrodynamic cavitation for the generation of microbubbles,"

Miner. Eng., vol. 132, no. September 2018, pp. 268–274, 2019, doi:

10.1016/j.mineng.2018.11.001.

[51]   F. Caupin and E. Herbert, "Cavitation in water: a review," *Comptes Rendus Phys.*,

vol. 7, no. 9–10, pp. 1000–1017, 2006, doi: 10.1016/j.crhy.2006.10.015.

[52]   P. R. Gogate and A. B. Pandit, "A review and assessment of hydrodynamic

cavitation as a technology for the future," *Ultrason. Sonochem.*, vol. 12, no. 1–2,

pp. 21–27, 2005, doi: 10.1016/j.ultsonch.2004.03.007.

[53]   S. Jones, "The cycle of bubble production from a gas cavity in a supersaturated

solution," *Adv. Colloid Interface Sci.*, vol. 80, no. 1, pp. 51–84, 1999, doi:

10.1016/S0001-8686(98)00075-X.

[54]   M. C. Sukop and D. Or, "Lattice Boltzmann method for homogeneous and

heterogeneous cavitation," *Phys. Rev. E - Stat. Nonlinear, Soft Matter Phys.*, vol.

71, no. 4, pp. 1–5, 2005, doi: 10.1103/PhysRevE.71.046703.

[55]   D. R. Cyr, "Bubble growth behaviour in supersaturated liquid solutions,"

University of Maine, 2001.

[56]   B. M. Borkent, S. Gekle, A. Prosperetti, and D. Lohse, "Nucleation threshold and

deactivation mechanisms of nanoscopic cavitation nuclei," *Phys. Fluids*, vol. 21,

no. 10, p. 102003, 2009, doi: 10.1063/1.3249602.

[57]   S. Jones, "Bubble nucleation from gas cavities — a review," *Adv. Colloid*

Interface Sci., vol. 80, no. 1, pp. 27–50, 1999, doi: 10.1016/S0001-8686(98)00074-8.

[58]   H. B. Marschall, K. a. Mørch, a. P. Keller, and M. Kjeldsen, "Cavitation inception by almost spherical solid particles in water," *Phys. Fluids*, vol. 15, no. 2, pp. 545–553, 2003, doi: 10.1063/1.1535940.

[59]   L. A. Crum, "Tensile strength of water," *Nature*, vol. 278, no. 5700, pp. 148–149, 1979, doi: 10.1038/278148a0.

[60]   K. A. Morch, "Reflections on cavitation nuclei in water," *Phys. Fluids*, vol. 19, no. 7, p. 072104, 2007, doi: 10.1063/1.2747210.

[61]   K. Ulatowski, P. Sobieszuk, A. Mróz, and T. Ciach, "Stability of nanobubbles generated in water using porous membrane system," *Chem. Eng. Process. - Process Intensif.*, vol. 136, no. July 2018, pp. 62–71, 2019, doi: 10.1016/j.cep.2018.12.010.

[62]   J. N. Meegoda, S. Aluthgun Hewage, and J. H. Batagoda, "Stability of nanobubbles," *Environ. Eng. Sci.*, vol. 35, no. 11, pp. 1216–1227, 2018, doi: 10.1089/ees.2018.0203.

[63]   B. E. Oeffinger and M. A. Wheatley, "Development and characterization of a nano-scale contrast agent," *Ultrasonics*, vol. 42, no. 1–9, pp. 343–347, 2004, doi: 10.1016/j.ultras.2003.11.011.

[64]   M. Alheshibri, J. Qian, M. Jehannin, and V. S. J. Craig, "A history of nanobubbles," *Langmuir*, vol. 32, no. 43, pp. 11086–11100, 2016, doi:

10.1021/acs.langmuir.6b02489.

[65]   Milton S. Plesset, "On the stability of gas bubbles in liquid-gas solutions," vol. c, pp. 133–141, 1982.

[66]   K. Yasui, *Acoustic cavitation and bubble dynamics*. 2018.

[67]   D. J. Stierman, "Generation of stabilized microbubbles in seawater," pp. 209–211, 1981.

[68]   F. E. Fox and K. F. Herzfeld, "Gas bubbles with organic skin as cavitation nuclei," *J. Acoust. Soc. Am.*, vol. 26, no. 6, pp. 984–989, 1954, doi: 10.1121/1.1907466.

[69]   M. Mezger *et al.*, "Water and ice in contact with octadecyl-trichlorosilane functionalized surfaces: A high resolution x-ray reflectivity study," *J. Chem. Phys.*, vol. 128, no. 24, 2008, doi: 10.1063/1.2931574.

[70]   I. Pereiro, A. Fomitcheva Khartchenko, L. Petrini, and G. V. Kaigala, "Nip the bubble in the bud: A guide to avoid gas nucleation in microfluidics," *Lab Chip*, vol. 19, no. 14, pp. 2296–2314, 2019, doi: 10.1039/c9lc00211a.

[71]   A. a. Atchley and A. Prosperetti, "The crevice model of bubble nucleation," *J. Acoust. Soc. Am.*, vol. 86, no. 3, p. 1065, 1989, doi: 10.1121/1.398098.

[72]   S. B. Sant, *Physics and Chemistry of Interfaces*, vol. 28, no. 12. 2013.

[73]   A. Ferrari, "Fluid dynamics of acoustic and hydrodynamic cavitation in hydraulic power systems," *Proceedings of the Royal Society A: Mathematical, Physical and Engineering Sciences*, vol. 473, no. 2199. 2017, doi: 10.1098/rspa.2016.0345.

[74]   R. Sander, "Compilation of Henry's law constants (version 4.0) for water as

solvent," *Atmos. Chem. Phys.*, vol. 15, no. 8, pp. 4399–4981, 2015, doi: 10.5194/acp-15-4399-2015.

[75]   M. Medrano, P. J. Zermatten, C. Pellone, J. Franc, and F. Ayela, "Hydrodynamic cavitation in microsystems. I. Experiments with deionized water and nanofluids," *Phys. Fluids*, vol. 23, no. 12, 2011, doi: 10.1063/1.3671682.

[76]   C. Mishra and Y. Peles, "Cavitation in flow through a micro-orifice inside a silicon microchannel," *Phys. Fluids*, vol. 17, no. 1, 2005, doi: 10.1063/1.1827602.

[77]   T. B. Benjamin and A. T. Ellis, "The collapse of cavitation bubbles and the pressures thereby produced against solid boundaries," *R. Soc.*, vol. 260, no. 1110, 1966.

[78]   I. Tzanakis, D. G. Eskin, A. Georgoulas, and D. K. Fytanidis, "Incubation pit analysis and calculation of the hydrodynamic impact pressure from the implosion of an acoustic cavitation bubble," *Ultrason. Sonochem.*, vol. 21, no. 2, pp. 866–878, 2014, doi: 10.1016/j.ultsonch.2013.10.003.

[79]   C. Zhang *et al.*, "Dynamic behavior of the cavitation bubbles collapsing between a rigid wall and an elastic wall," *AIP Adv.*, vol. 11, no. 6, 2021, doi: 10.1063/5.0053331.

[80]   L. Van Wijngaarden, "Mechanics of collapsing cavitation bubbles," *Ultrason. Sonochem.*, vol. 1, no. 3, pp. 1–8, 2016.

[81]   Y. Tomita and A. Shima, "High-speed photographic observations of laser-induced cavitation bubbles in water," *Acta Acust. united with Acust.*, vol. 71, no. 3, pp.

161–171, 1990.

[82]   A. Karimi and F. Avellan, "Comparison of erosion mechanisms in different types of cavitation," *Wear*, vol. 113, no. 3, pp. 305–322, 1986, doi: 10.1016/0043-1648(86)90031-1.

[83]   D. Hart and D. Whale, "A review of cavitation-erosion resistant weld surfacing alloys for hydroturbines," *Eutectic Aust. Pty. Ltd., Sydney*, p. 15, 2007.

[84]   S. Shimizu and A. Yamaguchi, "Erosion in hydraulic oil, HWCFs , and tap water," 1989.

[85]   P. R. Gogate and A. M. Kabadi, "A review of applications of cavitation in biochemical engineering/biotechnology," *Biochem. Eng. J.*, vol. 44, no. 1, pp. 60–72, 2009, doi: 10.1016/j.bej.2008.10.006.

[86]   E. Joyce, S. S. Phull, J. P. Lorimer, and T. J. Mason, "The development and evaluation of ultrasound for the treatment of bacterial suspensions. A study of frequency, power and sonication time on cultured Bacillus species," *Ultrason. Sonochem.*, vol. 10, no. 6, pp. 315–318, 2003, doi: 10.1016/S1350-4177(03)00101-9.

[87]   P. R. Gogate, "Hydrodynamic cavitation for food and water processing," *Food Bioprocess Technol.*, vol. 4, no. 6, pp. 996–1011, 2011, doi: 10.1007/s11947-010-0418-1.

[88]   M. Sivakumar and A. B. Pandit, "Wastewater treatment: A novel energy efficient hydrodynamic cavitational technique," *Ultrason. Sonochem.*, vol. 9, no. 3, pp.

123–131, 2002, doi: 10.1016/S1350-4177(01)00122-5.

[89] D. V. Pinjari and A. B. Pandit, "Room temperature synthesis of crystalline CeO2 nanopowder: Advantage of sonochemical method over conventional method," *Ultrason. Sonochem.*, vol. 18, no. 5, pp. 1118–1123, 2011, doi: 10.1016/j.ultsonch.2011.01.008.

[90] A. P. A Mahulkar, "Analysis of hydrodynamic and acoustic cavitation reactors." Germany: VDM publishing, 2010, [Online]. Available: http://googlescholar.blogspot.my/2011/07/google-scholar-citations.html.

[91] V. K. Saharan, M. A. Rizwani, A. A. Malani, and A. B. Pandit, "Effect of geometry of hydrodynamically cavitating device on degradation of orange-G," *Ultrason. Sonochem.*, vol. 20, no. 1, pp. 345–353, 2013, doi: 10.1016/j.ultsonch.2012.08.011.

[92] K. B. Ansari *et al.*, "Process intensification of upgradation of crude oil and vacuum residue by hydrodynamic cavitation and microwave irradiation," *Indian Chem. Eng.*, vol. 57, no. 3–4, pp. 256–281, 2015, doi: 10.1080/00194506.2015.1026949.

[93] P. J. Milly, R. T. Toledo, M. A. Harrison, and D. Armstead, "Inactivation of food spoilage microorganisms by hydrodynamic cavitation to achieve pasteurization and sterilization of fluid foods," *J. Food Sci.*, vol. 72, no. 9, pp. 414–422, 2007, doi: 10.1111/j.1750-3841.2007.00543.x.

[94] R. K. Bhaskaracharya, S. Kentish, and M. Ashokkumar, "Selected applications of ultrasonics in food processing," *Food Eng. Rev.*, vol. 1, no. 1, pp. 31–49, 2009,

doi: 10.1007/s12393-009-9003-7.

[95]   Z. J. Dolatowski, J. Stadnik, and D. Stasiak, "Applications of ultrasound in food technology.," *ACTA Sci. Pol.*, vol. 63, no. 6, pp. 89–99, 2007.

[96]   M. Ashokkumar, R. Rink, and S. Shestakov, "Hydrodynamic cavitation – an alternative to ultrasonic food processing," *Tech. Acoust.*, vol. 9, pp. 1–10, 2011.

[97]   M. Preparation and P. S. Separation, "Chapter 3 Physical and physico-chemical processes," *Waste Manag. Ser.*, vol. 7, no. C, pp. 35–69, 2006, doi: 10.1016/S0713-2743(06)80088-7.

[98]   C. B. Crawford and B. Quinn, "Microplastic separation techniques," *Microplastic Pollut.*, pp. 203–218, 2017, doi: 10.1016/b978-0-12-809406-8.00009-8.

[99]   L. Xie *et al.*, "Surface interaction mechanisms in mineral flotation: Fundamentals, measurements, and perspectives," *Adv. Colloid Interface Sci.*, vol. 295, p. 102491, 2021, doi: 10.1016/j.cis.2021.102491.

[100] Y. Xing, X. Gui, F. Karakas, and Y. Cao, "Role of collectors and depressants in mineral flotation: A theoretical analysis based on extended DLVO theory," *Minerals*, vol. 7, no. 11, 2017, doi: 10.3390/min7110223.

[101] B. V. Derjaguin and S. S. Dukhin, "Theory of flotation of small and medium-size particles," *Prog. Surf. Sci.*, vol. 43, no. 1–4, pp. 241–266, 1993, doi: 10.1016/0079-6816(93)90034-S.

[102] R. H. Yoon, "The role of hydrodynamic and surface forces in bubble-particle interaction," *Int. J. Miner. Process.*, vol. 58, no. 1–4, pp. 129–143, Feb. 2000, doi:

10.1016/S0301-7516(99)00071-X.

[103] B. Shahbazi, B. Rezai, and S. M. Javad Koleini, "Bubble-particle collision and attachment probability on fine particles flotation," *Chem. Eng. Process. Process Intensif.*, vol. 49, no. 6, pp. 622–627, 2010, doi: 10.1016/j.cep.2010.04.009.

[104] A. V. Nguyen, J. Ralston, and H. J. Schulze, "On modelling of bubble-particle attachment probability in flotation," *Int. J. Miner. Process.*, vol. 53, no. 4, pp. 225–249, 1998, doi: 10.1016/S0301-7516(97)00073-2.

[105] D. I. Verrelli and B. Albijanic, "A comparison of methods for measuring the induction time for bubble-particle attachment," *Miner. Eng.*, vol. 80, pp. 8–13, 2015, doi: 10.1016/j.mineng.2015.06.011.

[106] D. Tao, "Role of bubble size in flotation of coarse and fine particles - a review," *Sep. Sci. Technol.*, vol. 39, no. 4, pp. 741–760, 2005, doi: 10.1081/ss-120028444.

[107] Y. Xing, X. Gui, Y. Cao, D. Wang, and H. Zhang, "Clean low-rank-coal purification technique combining cyclonic-static microbubble flotation column with collector emulsification," *J. Clean. Prod.*, vol. 3, 2016, doi: 10.1016/j.jclepro.2016.11.057.

[108] V. Belova, M. Krasowska, D. Wang, J. Ralston, D. G. Shchukin, and H. Möhwald, "Influence of adsorbed gas at liquid/solid interfaces on heterogeneous cavitation," *Chem. Sci.*, vol. 4, no. 1, pp. 248–256, 2013, doi: 10.1039/C2SC21321D.

[109] M. Fan, D. Tao, R. Honaker, and Z. Luo, "Nanobubble generation and its applications in froth flotation (part III): Specially designed laboratory scale column

flotation of phosphate," *Min. Sci. Technol.*, vol. 20, no. 3, pp. 317–338, 2010, doi: 10.1016/S1674-5264(09)60205-2.

[110] R. H. Yoon and G. H. Luttrell, "The effect of bubble size on fine particle flotation," *Miner. Process. Extr. Metall. Rev.*, vol. 5, no. 1–4, pp. 101–122, Feb. 1989, doi: 10.1080/08827508908952646.

[111] G. Gu, R. S. Sanders, K. Nandakumar, Z. Xu, and J. H. Masliyah, "A novel experimental technique to study single bubble-bitumen attachment in flotation," *Int. J. Miner. Process.*, vol. 74, no. 1–4, pp. 15–29, 2004, doi: 10.1016/j.minpro.2003.08.002.

[112] M. A. Hampton and A. V. Nguyen, "Nanobubbles and the nanobubble bridging capillary force," *Adv. Colloid Interface Sci.*, vol. 154, no. 1–2, pp. 30–55, 2010, doi: 10.1016/j.cis.2010.01.006.

[113] H. Schubert, "Nanobubbles, hydrophobic effect, heterocoagulation and hydrodynamics in flotation," *Int. J. Miner. Process.*, vol. 78, no. 1, pp. 11–21, 2005, doi: 10.1016/j.minpro.2005.07.002.

[114] H. Butt, K. Graf, and M. Kappl, *Physics and Chemistry of Interfaces*. 2003.

[115] X. Zhang, R. Manica, Y. Tang, P. Tchoukov, Q. Liu, and Z. Xu, "Probing boundary conditions at hydrophobic solid–water interfaces by dynamic film drainage measurement," *Langmuir*, vol. 34, no. 40, pp. 12025–12035, 2018, doi: 10.1021/acs.langmuir.8b02492.

[116] L. Pan and R. H. Yoon, "Measurement of hydrophobic forces in thin liquid films

of water between bubbles and xanthate-treated gold surfaces," *Miner. Eng.*, vol. 98, pp. 240–250, 2016, doi: 10.1016/j.mineng.2016.09.005.

[117] A. Nikolaev, "Flotation kinetic model with respect to particle heterogeneity and roughness," *Int. J. Miner. Process.*, vol. 155, pp. 74–82, 2016, doi: 10.1016/j.minpro.2016.08.005.

[118] K. Huang and R. Yoon, "Effect of ζ -potentials on bubble-particle interactions," no. November 2018, pp. 21–34, 2019.

[119] L. Wang, Z. Xu, and J. H. Masliyah, "Dissipation of film drainage resistance by hydrophobic surfaces in aqueous solutions," *J. Phys. Chem. C*, vol. 117, no. 17, pp. 8799–8805, 2013, doi: 10.1021/jp4000945.

[120] V. V. Yaminsky, S. Ohnishi, E. A. Vogler, and R. G. Horn, "Stability of aqueous films between bubbles. Part 1. the effect of speed on bubble coalescence in purified water and simple electrolyte solutions," *Langmuir*, vol. 26, no. 11, pp. 8061–8074, 2010, doi: 10.1021/la904481d.

[121] I. U. Vakarelski *et al.*, "Dynamic interactions between microbubbles in water.," *Proc. Natl. Acad. Sci.*, vol. 107, no. 25, pp. 11177–11182, 2010, doi: 10.1073/pnas.1005937107.

[122] D. Y. C. Chan, E. Klaseboer, and R. Manica, "Film drainage and coalescence between deformable drops and bubbles," *Soft Matter*, vol. 7, no. 6, p. 2235, 2011, doi: 10.1039/c0sm00812e.

[123] B. Liu *et al.*, "Dynamic interaction between a millimeter-sized bubble and surface

microbubbles in water," 2018, doi: 10.1021/acs.langmuir.8b01202.

[124] R. G. Horn, L. A. Del Castillo, and S. Ohnishi, "Coalescence map for bubbles in surfactant-free aqueous electrolyte solutions," *Adv. Colloid Interface Sci.*, vol. 168, no. 1–2, pp. 85–92, 2011, doi: 10.1016/j.cis.2011.05.006.

[125] M. H. W. Hendrix, R. Manica, E. Klaseboer, D. Y. C. Chan, and C. D. Ohl, "Spatiotemporal evolution of thin liquid films during impact of water bubbles on glass on a micrometer to nanometer scale," *Phys. Rev. Lett.*, vol. 108, no. 24, pp. 1–4, 2012, doi: 10.1103/PhysRevLett.108.247803.

[126] M. T. Gevari, T. Abbasiasl, S. Niazi, M. Ghorbani, and A. Koşar, "Direct and indirect thermal applications of hydrodynamic and acoustic cavitation: A review," *Appl. Therm. Eng.*, vol. 171, no. February, 2020, doi: 10.1016/j.applthermaleng.2020.115065.

[127] B. Schneider, A. Koşar, and Y. Peles, "Hydrodynamic cavitation and boiling in refrigerant (R-123) flow inside microchannels," *Int. J. Heat Mass Transf.*, vol. 50, no. 13–14, pp. 2838–2854, 2007, doi: 10.1016/j.ijheatmasstransfer.2007.01.002.

[128] M. T. Gevari, M. Ghorbani, A. J. Svagan, D. Grishenkov, and A. Kosar, "Energy harvesting with micro scale hydrodynamic cavitation-thermoelectric generation coupling," *AIP Adv.*, vol. 9, no. 10, 2019, doi: 10.1063/1.5115336.

[129] M. Ghorbani, A. Mohammadi, A. R. Motezakker, L. G. Villanueva, Y. Leblebici, and A. Koşar, "Energy harvesting in microscale with cavitating flows," *ACS Omega*, vol. 2, no. 10, pp. 6870–6877, 2017, doi: 10.1021/acsomega.7b01204.

[130] B. Schneider *et al.*, "Cavitation enhanced heat transfer in microchannels," *J. Heat Transfer*, vol. 128, no. 12, pp. 1293–1301, 2006, doi: 10.1115/1.2349505.

[131] Z. Du, M. P. Bilbao-Montoya, B. P. Binks, E. Dickinson, R. Ettelaie, and B. S. Murray, "Outstanding stability of particle-stabilized bubbles," *Langmuir*, vol. 19, no. 8, pp. 3106–3108, 2003, doi: 10.1021/la034042n.

[132] K. Yasui, T. Tuziuti, and W. Kanematsu, "Mysteries of bulk nanobubbles (ultrafine bubbles); stability and radical formation," *Ultrason. Sonochem.*, vol. 48, no. March, pp. 259–266, 2018, doi: 10.1016/j.ultsonch.2018.05.038.

[133] D. Fuster, K. Pham, and S. Zaleski, "Stability of bubbly liquids and its connection to the process of cavitation inception," *Phys. Fluids*, vol. 26, no. 4, 2014, doi: 10.1063/1.4870820.

[134] F. G. Blake, "The onset of cavitation in liquids," *Harvard Univ. Tech. Memo.*, vol. 12, 1949.

[135] B. M. Borkent, S. Gekle, A. Prosperetti, and D. Lohse, "Nucleation threshold and deactivation mechanisms of nanoscopic cavitation nuclei," *Phys. Fluids*, vol. 21, no. 10, p. 102003, 2009, doi: 10.1063/1.3249602.

[136] R. T. Knapp, J. W. Daily, and F. G. Hammitt, *Cavitation*. Institute of Hydraulic Research, University of Iowa, 1979.

[137] J. G. Auret, O. F. R. A. Damm, G. J. Wright, and F. P. A. Robinson, "The influence of water air content on cavitation erosion in distilled water," *Tribol. Int.*, vol. 26, no. 6, pp. 431–433, 1993, doi: 10.1016/0301-679X(93)90083-D.

[138] B. Li, Y. Gu, and M. Chen, "An experimental study on the cavitation of water with dissolved gases," *Exp. Fluids*, vol. 58, no. 12, pp. 1–9, 2017, doi: 10.1007/s00348-017-2449-0.

[139] R. Lange, H. Staaland, and A. Mostad, "The effect of salinity and temperature on solubility of oxygen and respiratory rate in oxygen-dependent marine invertebrates," *J. Exp. Mar. Bio. Ecol.*, vol. 9, no. 3, pp. 217–229, 1972, doi: 10.1016/0022-0981(72)90034-2.

[140] S. Ceccio, S. Gowing, and Y. T. Shen, "The effects of salt water on bubble cavitation," *J. Fluids Eng. Trans. ASME*, vol. 119, no. 1, pp. 155–163, 1997, doi: 10.1115/1.2819102.

[141] A. L. Nye, X. Wu, and G. L. Chahine, "Bubble generation and sizing in fresh and salt water," *9th Int'l Conf. Two-Phase Syst. Gr. Sp. Appl.*, no. January 2015, pp. 2–4, 2014, doi: 10.13140/2.1.3972.6406.

[142] A. Bussonnière, Q. Liu, and P. A. Tsai, "Cavitation nuclei regeneration in a water-particle suspension," *Phys. Rev. Lett.*, vol. 124, no. 3, p. 34501, 2020, doi: 10.1103/PhysRevLett.124.034501.

[143] Y. Chen, J. Chang, A. Bussonnière, G. Xie, and Q. Liu, "Evaluation of wettability of mineral particles via cavitation thresholds," *Powder Technol.*, vol. 362, pp. 334–340, 2020, doi: 10.1016/j.powtec.2019.11.069.

[144] M. A. Hosien and S. M. Selim, "Acoustic detection of cavitation inception," *J. Appl. Fluid Mech.*, vol. 10, no. 1, pp. 31–40, 2017, doi: 10.18869/acadpub.jafm.73.238.25638.

[145] M. Li, "Influence of Venturi tube geometry and particle properties on the hydrodynamic cavitation for fine particle flotation," University of Alberta, 2017.

[146] J. Černetič, J. Prezelj, and M. Čudina, "Use of noise and vibration signal for detection and monitoring of cavitation in kinetic pumps," *Proc. - Eur. Conf. Noise Control*, pp. 2199–2204, 2008, doi: 10.1121/1.2933777.

[147] H. Shi, M. Li, P. Nikrityuk, and Q. Liu, "Experimental and numerical study of cavitation flows in venturi tubes: From CFD to an empirical model," *Chem. Eng. Sci.*, vol. 207, pp. 672–687, 2019, doi: 10.1016/j.ces.2019.07.004.

[148] R. F. Weiss, "The solubility of nitrogen, oxygen and argon in water and seawater," *Deep. Res. Oceanogr. Abstr.*, vol. 17, no. 4, pp. 721–735, 1970, doi: 10.1016/0011-7471(70)90037-9.

[149] M. Takahashi, K. Chiba, and P. Li, "Free-radical generation from collapsing microbubbles in the absence of a dynamic stimulus," *J. Phys. Chem. B*, vol. 111, no. 6, pp. 1343–1347, 2007, doi: 10.1021/jp0669254.

[150] V. S. Craig, "Gas solubility of electrolytes," in *Encyclopedia of Applied Electrochemistry*, G. Kreysa, K. Ota, and R. F. Savinell, Eds. New York, NY: Springer New York, 2014, pp. 927–931.

[151] C. S. Widodo, H. Sela, and D. R. Santosa, "The effect of NaCl concentration on the ionic NaCl solutions electrical impedance value using electrochemical impedance spectroscopy methods," *AIP Conf. Proc.*, vol. 2021, no. 2018, pp. 0–6, 2018, doi: 10.1063/1.5062753.

[152] Mook W, "Chemistry of carbonic acid in water," in *Environmental Isotopes in the Hydrological Cycle: Principles and Applications*, 2000, pp. 143–165.

[153] B. M. Smirnov and R. Stephen Berry, "Growth of bubbles in liquid," *Chem. Cent. J.*, vol. 9, no. 1, pp. 1–8, 2015, doi: 10.1186/s13065-015-0127-y.

[154] G. Kuiper, "Physics of cavitation : cavitation inception," in *Cavitation in ship propulsion*, 2012, pp. 17–27.

[155] P. Pawliszak, V. Ulaganathan, B. H. Bradshaw-Hajek, R. Manica, D. A. Beattie, and M. Krasowska, "Mobile or immobile? rise velocity of air bubbles in high-purity water," *J. Phys. Chem. C*, 2019, doi: 10.1021/acs.jpcc.9b03526.

[156] G. Jones and W. A. Ray, "The surface tension of solutions of electrolytes as a function of the concentration. III. Sodium chloride," *J. Am. Chem. Soc.*, vol. 63, no. 12, pp. 3262–3263, 1941, doi: 10.1021/ja01857a007.

[157] V. S. Craig, B. W. Ninham, and R. M. Pashley, "The effect of electrolytes on bubble coalescence in water," *J. Phys. Chem.*, vol. 97, no. 39, pp. 10192–10197, 1993, doi: 10.1021/j100141a047.

[158] K. A. Mørch, "Cavitation inception from bubble nuclei," *Interface Focus*, vol. 5, no. 5, pp. 1–13, 2015, doi: 10.1098/rsfs.2015.0006.

[159] G. Kuiper, "Chapter 3 Physics of cavitation : GAS CONTENT," in *Cavitation in Ship Propulsion*, 2010, pp. 9–79.

[160] R. H. Yoon, D. H. Flinn, and Y. I. Rabinovich, "Hydrophobic interactions between dissimilar surfaces," *J. Colloid Interface Sci.*, vol. 185, no. 2, pp. 363–370, 1997,

doi: 10.1006/jcis.1996.4583.

[161] M. C. Fuerstenau, Graeme J., and R. H. Yoon, *Froth flotation: a century of innovation*. Society for Mining, Metallurgy, and Exploration, Inc., 2007.

[162] E. Forbes, "Shear, selective and temperature responsive flocculation: A comparison of fine particle flotation techniques," *Int. J. Miner. Process.*, vol. 99, no. 1–4, pp. 1–10, 2011, doi: 10.1016/j.minpro.2011.02.001.

[163] J. Gregory and S. Barany, "Adsorption and flocculation by polymers and polymer mixtures," *Adv. Colloid Interface Sci.*, vol. 169, no. 1, pp. 1–12, 2011, doi: 10.1016/j.cis.2011.06.004.

[164] L. J. Warren, "Shear-flocculation of ultrafine scheelite in sodium oleate solutions," *J. Colloid Interface Sci.*, vol. 50, no. 2, pp. 307–318, 1975, doi: 10.1016/0021-9797(75)90234-9.

[165] M. Li, R. Manica, B. Xiang, and Q. Liu, "Effect of NaCl and CO2 on the inception control of hydrodynamic cavitation by gas solubility change," *Chem. Eng. Sci.*, vol. 246, p. 116997, 2021, doi: 10.1016/j.ces.2021.116997.

[166] L. Zang, "Heterogeneous nucleation : a surface catalyzed process." pp. 1–5, 2015, [Online]. Available: http://www.eng.utah.edu/~lzang/images/lecture-12.pdf.

[167] W. L. Ryan and E. A. Hemmingsen, "Bubble formation in water at smooth hydrophobic surfaces," *Journal of Colloid And Interface Science*, vol. 157, no. 2. pp. 312–317, 1993, doi: 10.1006/jcis.1993.1191.

[168] R. E. Apfel, "The role of impurities in cavitation-threshold determination," *J.*

Acoust. Soc. Am., vol. 48, no. 5B, p. 1179, 1970, doi: 10.1121/1.1912258.

[169] Formlabs, "Intro to stereolithography 3D printing a comprehensive guide for professional users," no. May. pp. 1–18, 2019, [Online]. Available: https://3d.formlabs.com/introduction-to-stereolithography/.

[170] N. P. Murphy and R. H. Petrmichl, "Highly durable hydrophobic coatings and methods," 2004.

[171] C. S. Martin, H. Medlarz, D. C. Wiggert, and C. Brennen, "Cavitation inception in spool valves," *J. Fluids Eng.*, vol. 103, no. 4, p. 564, 1981, doi: 10.1115/1.3241768.

[172] W. R. Turner, "Microbubble persistence in fresh water," *J. Acoust. Soc. Am.*, vol. 33, no. 9, pp. 1223–1233, 1961, doi: 10.1121/1.1908960.

[173] P. S. Epstein and M. S. Plesset, "On the stability of gas bubbles in liquid-gas solutions," *J. Chem. Phys.*, vol. 18, no. 11, p. 256, 1950, doi: https://doi.org/10.1063/1.1747520.

[174] F. G. Blake, *Onset of Cavitation in Liquids*. Harvard University, 1949.

[175] A. A. Atchley and A. Prosperetti, "The crevice model of bubble nucleation," *J. Acoust. Soc. Am.*, vol. 86, no. 3, p. 1065, 1989, doi: 10.1121/1.398098.

[176] H.-J. Butt, K. Graf, and M. Kappl, "Liquid Surfaces," in *Physics and Chemistry of Interfaces*, John Wiley & Sons, Ltd, 2003, pp. 4–25.

[177] L. L. Schramm and R. J. Mikula, "Froth flotation of oil sand bitumen," in *Foam Engineering: Fundamentals and Applications*, 2012, pp. 251–281.

[178] T. Kasongo, Z. Zhou, Z. Xu, and J. Masliyah, "Effect of clays and calcium ions on bitumen extraction from Athabasca oil sands using flotation," in *Canadian Journal of Chemical Engineering*, 2000, vol. 78, no. 4, pp. 674–681, doi: 10.1002/cjce.5450780409.

[179] C. Wang, H. Wang, J. gang Fu, and Y. nian Liu, "Flotation separation of waste plastics for recycling-A review," *Waste Manag.*, vol. 41, pp. 28–38, 2015, doi: 10.1016/j.wasman.2015.03.027.

[180] H. Shent, R. J. Pugh, and E. Forssberg, "A review of plastics waste recycling and the flotation of plastics," *Resources, Conservation and Recycling*, vol. 25, no. 2. pp. 85–109, 1999, doi: 10.1016/S0921-3449(98)00017-2.

[181] W. J. Trahar, "A rational interpretation of the role of particle size in flotation," *Int. J. Miner. Process.*, vol. 8, no. 4, pp. 289–327, Oct. 1981, doi: 10.1016/0301-7516(81)90019-3.

[182] W. J. Trahar, "The selective flotation of galena from sphalerite with special reference to the effects of particle size," *Int. J. Miner. Process.*, vol. 3, no. 2, pp. 151–166, 1976, doi: 10.1016/0301-7516(76)90031-4.

[183] D. Feng and C. Aldrich, "Effect of particle size on flotation performance of complex sulphide ores," *Miner. Eng.*, vol. 12, no. 7, pp. 721–731, Jul. 1999, doi: 10.1016/S0892-6875(99)00059-X.

[184] Z. Dai, D. Fornasiero, and J. Ralston, "Particle–bubble attachment in mineral flotation," *J. Colloid Interface Sci.*, vol. 217, no. 1, pp. 70–76, Sep. 1999, doi: 10.1006/JCIS.1999.6319.

[185] Y. Xing *et al.*, "Recent experimental advances for understanding bubble-particle attachment in flotation," *Adv. Colloid Interface Sci.*, vol. 246, pp. 105–132, Aug. 2017, doi: 10.1016/J.CIS.2017.05.019.

[186] B. V. V. Derjaguin and S. S. S. Dukhin, "Theory of flotation of small and medium-size particles," *Prog. Surf. Sci.*, vol. 43, no. 1–4, pp. 241–266, May 1993, doi: 10.1016/0079-6816(93)90034-S.

[187] J. Laskowski and J. A. Kitchener, "The hydrophilic—hydrophobic transition on silica," *J. Colloid Interface Sci.*, vol. 29, no. 4, pp. 670–679, Apr. 1969, doi: 10.1016/0021-9797(69)90219-7.

[188] A. V. Nguyen, J. Nalaskowski, and J. D. Miller, "A study of bubble–particle interaction using atomic force microscopy," *Miner. Eng.*, vol. 16, no. 11, pp. 1173–1181, Nov. 2003, doi: 10.1016/J.MINENG.2003.07.013.

[189] Z. Pourkarimi, B. Rezai, M. Noaparast, A. V. Nguyen, and S. Chehreh Chelgani, "Proving the existence of nanobubbles produced by hydrodynamic cavitation and their significant effects in powder flotation," *Adv. Powder Technol.*, vol. 32, no. 5, pp. 1810–1818, 2021, doi: 10.1016/j.apt.2021.03.039.

[190] P. R. Gogate, R. K. Tayal, and A. B. Pandit, "Cavitation: a technology on the horizon," *Curr. Sci.*, vol. 91, no. 1, pp. 35–46, 2006.

[191] W. Xia, J. Yang, and C. Liang, "A short review of improvement in flotation of low rank/oxidized coals by pretreatments," *Powder Technol.*, vol. 237, pp. 1–8, 2013, doi: 10.1016/j.powtec.2013.01.017.

[192]   M. Li, A. Bussonnière, M. Bronson, Z. Xu, and Q. Liu, "Study of Venturi tube geometry on the hydrodynamic cavitation for the generation of microbubbles," *Miner. Eng.*, vol. 132, no. September 2018, pp. 268–274, 2019, doi: 10.1016/j.mineng.2018.11.001.

[193]   Z. Dai, D. Fornasiero, and J. Ralston, "Influence of dissolved gas on bubble-particle heterocoagulation," *J. Chem. Soc.{,} Faraday Trans.*, vol. 94, no. 14, pp. 1983–1987, 1998, doi: 10.1039/A801144C.

[194]   Z. Dai, S. Dukhin, D. Fornasiero, and J. Ralston, "The inertial hydrodynamic interaction of particles and rising bubbles with mobile surfaces," *J. Colloid Interface Sci.*, vol. 197, no. 2, pp. 275–292, Jan. 1998, doi: 10.1006/JCIS.1997.5280.

[195]   Z. Dai, S. Dukhin, D. Fornasiero, and J. Ralston, "The inertial hydrodynamic interaction of particles and rising bubbles with mobile surfaces," *J. Colloid Interface Sci.*, vol. 197, no. 2, pp. 275–292, 1998, doi: 10.1006/jcis.1997.5280.

[196]   J. Liu, Z. Zhou, Z. Xu, and J. Masliyah, "Bitumen-clay interactions in aqueous media studied by zeta potential distribution measurement," *J. Colloid Interface Sci.*, vol. 252, no. 2, pp. 409–418, 2002, doi: 10.1006/jcis.2002.8471.

[197]   C. Yang, T. Dabros, D. Li, J. Czarnecki, and J. H. Masliyah, "Measurement of the zeta potential of gas bubbles in aqueous solutions by microelectrophoresis method," *J. Colloid Interface Sci.*, vol. 243, no. 1, pp. 128–135, 2001, doi: 10.1006/jcis.2001.7842.

[198]   A. Sze, D. Erickson, L. Ren, and D. Li, "Zeta-potential measurement using the

Smoluchowski equation and the slope of the current-time relationship in electroosmotic flow," *J. Colloid Interface Sci.*, vol. 261, no. 2, pp. 402–410, 2003, doi: 10.1016/S0021-9797(03)00142-5.

[199] C. Wu, L. Wang, D. Harbottle, J. Masliyah, and Z. Xu, "Studying bubble-particle interactions by zeta potential distribution analysis," *J. Colloid Interface Sci.*, vol. 449, pp. 399–408, 2015, doi: 10.1016/j.jcis.2015.01.040.

[200] M. E. Weber and D. Paddock, "Interceptional and gravitational collision efficiencies for single collectors at intermediate Reynolds numbers," *J. Colloid Interface Sci.*, vol. 94, no. 2, pp. 328–335, 1983, doi: 10.1016/0021-9797(83)90270-9.

[201] R. H. Yoon, "The role of hydrodynamic and surface forces in bubble-particle interaction," *Int. J. Miner. Process.*, vol. 58, no. 1–4, pp. 129–143, 2000, doi: 10.1016/S0301-7516(99)00071-X.

[202] A. S. Najafi, Z. Xu, and J. Masliyah, "Measurement of sliding velocity and induction time of a single micro-bubble under an inclined collector surface," *Can. J. Chem. Eng.*, vol. 86, no. 6, pp. 1001–1010, 2008, doi: 10.1002/cjce.20116.

[203] R. Clift, J. R. Grace, and M. E. Weber, *Bubbles, Drops, and Particles*. Dover Publications, 1978.

[204] S. H. Park, C. Park, J. Y. Lee, and B. Lee, "A simple parameterization for the rising velocity of bubbles in a liquid pool," *Nucl. Eng. Technol.*, vol. 49, no. 4, pp. 692–699, 2017, doi: 10.1016/j.net.2016.12.006.

[205] D. Bhaga and M. E. Weber, "Bubbles in viscous liquids: shapes, wakes and velocities," *J. Fluid Mech.*, vol. 105, pp. 61–85, 1981, doi: 10.1017/S002211208100311X.

[206] N. M. Aybers and A. Tapucu, "Studies on the drag and shape of gas bubbles rising through a stagnant liquid," *Wärme- und Stoffübertragung*, vol. 2, no. 3, pp. 171–177, 1969, doi: 10.1007/BF00751164.

[207] P. G. Saffman, "On the rise of small air bubbles in water," *J. Fluid Mech.*, vol. 1, no. 3, pp. 249–275, 1956, doi: 10.1017/S0022112056000159.

[208] S. G. Bankoff, "Entrapment of gas in the spreading of a liquid over a rough surface," *AIChE J.*, vol. 4, no. 1, pp. 24–26, 1958, doi: 10.1002/aic.690040105.

[209] P. R. Jones *et al.*, "Sustaining dry surfaces under water," *Sci. Rep.*, vol. 5, pp. 1–10, 2015, doi: 10.1038/srep12311.

[210] V. I. Klassen and V. A. Mokrousov, *An introduction to the theory of flotation*. Butterworths, 1963.

[211] B. Liu, R. Manica, Q. Liu, E. Klaseboer, Z. Xu, and G. Xie, "Coalescence of bubbles with mobile interfaces in water," *Phys. Rev. Lett.*, vol. 122, no. 19, p. 194501, 2019, doi: 10.1103/PhysRevLett.122.194501.

[212] M. A. Hampton and A. V. Nguyen, "Nanobubbles and the nanobubble bridging capillary force," *Advances in Colloid and Interface Science*, vol. 154, no. 1–2. pp. 30–55, 2010, doi: 10.1016/j.cis.2010.01.006.

[213] R. H. Yoon and G. H. Luttrell, "The effect of bubble size on fine coal flotation,"

Coal Prep., vol. 2, no. 3, pp. 179–192, 1986, doi: 10.1080/07349348508905163.

[214] Z. T. Mathe, M. C. Harris, C. T. O'Connor, and J. P. Franzidis, "Review of froth modelling in steady state flotation systems," *Miner. Eng.*, vol. 11, no. 5, pp. 397–421, 1998, doi: 10.1016/S0892-6875(98)00020-X.

[215] J. Laskowski and J. A. Kitchener, "The hydrophilic-hydrophobic transition on silica," *J. Colloid Interface Sci.*, vol. 29, no. 4, pp. 670–679, 1969, doi: 10.1016/0021-9797(69)90219-7.

[216] A. V. Nguyen, J. Nalaskowski, and J. D. Miller, "A study of bubble-particle interaction using atomic force microscopy," *Miner. Eng.*, vol. 16, no. 11, pp. 1173–1181, 2003, doi: 10.1016/j.mineng.2003.07.013.

[217] A. Sobhy, R. Honaker, and D. Tao, "Nanobubble column flotation for more efficient coal recovery," vol. 507, pp. 1–7, 2013.

[218] G. Cheng, C. L. Shi, J. T. Liu, and X. K. Yan, "Bubble-distribution measurement in a flotation column," *Int. J. Coal Prep. Util.*, vol. 36, no. 5, pp. 241–250, 2016, doi: 10.1080/19392699.2015.1111878.

[219] H. Soyama and J. Hoshino, "Enhancing the aggressive intensity of hydrodynamic cavitation through a Venturi tube by increasing the pressure in the region where the bubbles collapse," *AIP Adv.*, vol. 6, no. 4, 2016, doi: 10.1063/1.4947572.

[220] Li，Mingda, A. Bussonnière, Matthew，Bronson, Z. Xu, and Q. Liu, "Influence of Venturi tube geometry on the hydrodynamic cavitation and bubble generation." Mineral Engineering, 2018.

[221] B. Liu *et al.*, "Dynamic interactions between a millimeter size bubble and surface microbubbles in Water." Submitted, Langmuir, 2018.